Numerical simulations to assess the effect of urban heat island mitigation strategies on regional air quality.

Inaugural-Dissertation

zur

Erlangung des Doktorgrades

der Mathematisch-Naturwissenschaftlichen Fakultät

der Universität zu Köln

vorgelegt von

Joachim Fallmann

aus München

2014

Berichterstatter: Prof. Dr. Stefan Emeis

Prof. Dr. Michael Kerschgens

Datum der mündlichen Prüfung: 27.11.2014

“What place would you advise me to visit now?” he asked.

“The planet Earth,“ replied the geographer.

“It has a good reputation.”

And the little prince went away, thinking of his flower.

“The Little Prince”

Antoine de Saint-Exupéry

Zusammenfassung

Die vorliegende Doktorarbeit präsentiert einen numerischen Modellierungsansatz um die Auswirkungen verschiedener Stadtplanungsmaßnahmen auf die Intensität der städtischen Wärmeinsel zu untersuchen und die Rückkopplung dieser Maßnahmen auf die chemische Zusammensetzung der städtischen Atmosphäre zu analysieren. Die Region Stuttgart dient dabei als Testgebiet.

Das mesoskalige Chemie-Transport-Modell WRF-Chem wird dazu verwendet, die Rückwirkung dieser Strategien zur Verringerung der städtischen Wärmeinsel auf die bodennahe Konzentration von primären (CO, NO, PM_{10}) und sekundären Schadstoffen (Ozon) zu diskutieren.

Untersucht werden bekannte Vermeidungsmaßnahmen wie der Effekt heller Dach- und Fassadenflächen, städtische Begrünung oder die Veränderung der Bebauungsdichte. All diese Strategien bewirken eine Verringerung der städtischen Temperatur und tragen somit zur Reduzierung der Wärmeinsel bei.

Die Modellergebnisse zeigen, dass stark reflektierende Oberflächen die effizienteste Methode sind, die städtische Wärmeinsel zu reduzieren. Innerstädtische Begrünung und eine veränderte Bebauungsdichte zeigen geringere Effekte im Modell. Im Falle einer Erhöhung der Dachflächen-Albedo von 0.2 auf 0.7 wird eine Abnahme der städtischen Wärmeinsel um ca. 2 °C im Mittel erreicht.

Die Veränderung der Energie- und Strahlungseigenschaften der städtischen Oberflächen aufgrund der zuvor genannten Vermeidungsmaßnahmen wirkt sich unterschiedlich auf die chemische Zusammensetzung der Atmosphäre aus. Während die mittlere Ozon-Konzentration um ca. 5 - 8 % pro 1 °C Temperaturverringerung reduziert werden kann, wird ein Anstieg primärer Schadstoffe wie NO und CO um 5 - 25 % prognostiziert.

Primär wird durch die Abnahme der Temperatur die dynamische Struktur der Atmosphäre verändert. Die turbulente Durchmischung wird verringert, die Mischungsschichthöhe sinkt daher, wodurch die bodennahe Konzentration von direkt emittierten Schadstoffen wie CO und NO ansteigt. Für den Rückgang der Ozonkonzentration mit sinkender Temperatur ist in erster Linie die direkte Korrelation zwischen Temperatur und Reaktionsgeschwindigkeit verantwortlich.

Es muss jedoch beachtet werden, dass die Maßnahmen auch sekundäre Prozesse nach sich ziehen können. Eine Erhöhung der Oberflächenreflexion durch weiße Dächer zum Beispiel erhöht die Intensität der kurzwelligen Strahlung, was dazu führt, dass maximale Ozonkonzentrationen kurzzeitig sogar ansteigen können. Die Erhöhung biogener Emissionen aufgrund zusätzlicher Bepflanzung wird in dieser Arbeit nicht berücksichtigt.

Hauptresultat ist, dass der Einfluss von Maßnahmen zur Verringerung der städtischen Wärmeinsel auf die Dynamik größer ist als auf die Chemie. Während in bisherigen Studien vorwiegend die positive Auswirkung auf Ozonbelastung diskutiert wurde, untersucht diese Arbeit eine umfassende Luftchemie und arbeitet damit den negativen Effekt auf primäre Schadstoffe heraus.

Abstract

Work in this thesis demonstrates a numerical modelling approach to analyse the effect of urban planning strategies on the urban heat island (UHI) intensity and further the feedback on the chemical composition of the urban atmosphere. The urban area of Stuttgart acts as test bed for the modelling.

The mesoscale chemical transport model WRF-Chem is used to investigate the effect of these urban heat island mitigation strategies on the surface concentration of primary (CO, NO, PM_{10}) and secondary pollutants (O_3).

Known mitigation strategies such as bright roofs and façades, urban greening and modification of the building density are in the focus. All these measures are able to reduce the urban temperature and thus mitigate urban heat island intensity.

Model results reveal that the most efficient way to cool down urban areas is the increase in the surface reflectivity. Changing the building albedo in the model from 0.2 to 0.7, lead to a reduction of the urban heat island by about 2 °C. The effect of urban greening and decreased building density is less.

The mitigation strategies which have been mentioned before promote changes in energetic and radiative properties of urban surfaces modifying the chemical nature of the urban atmosphere with regard to both primary and secondary compounds. A temperature reduction of 1 °C leads to an increase of NO and CO by 5-25 %, whereas the mean ozone concentration is projected to decrease by 5-8 %.

Reduced temperature on the surface and in the urban canopy layer influences the dynamical structure of the atmosphere, which leads to a reduction in turbulent mixing. The depth of the mixing layer is decreased accordingly. As a result, an increase of the near surface concentration of primary compounds is projected. Additionally, temperature directly controls the reactivity of chemical reactions, which explains the reduction of ozone concentration.

It has to be pointed out however, that different measures can generate secondary effects. The increased portion of short wave radiation due to a reflexion from white roofs for instance can promote photochemical reactions, leading to an increase of peak ozone levels

although temperature has been reduced. The additional emission of biogenic compounds coming along with urban greening is not covered in this work.

The main result of this work indicates the dominating role of atmospheric dynamics when analysing the impacts of urban heat island mitigation strategies on urban air quality. Whereas in earlier studies the main effort had been put on the positive effect of temperature dependent reduction of urban ozone concentration, this work analyses a complete air chemistry, being able to show negative effects on primary compounds like CO, NO and PM_{10} as well.

Acknowledgements

First of all I have to thank my supervisor Prof. Dr. Stefan Emeis who supported me throughout the last 3 years. He introduced me to the field of meteorology and atmospheric modelling and gave me the opportunity to independently work on an interesting topic with public relevance.

Further I have to thank all members of the working group *Regional Coupling of Ecosystem-Atmosphere Processes*, in particular Renate Forkel, Richard Foreman and Peter Suppan who always had an open door for discussions and conversation of any kind. Thanks also to Elija Bleher who supported me in my work as PHD-Representative of the IMK-IFU and to Michael Warscher who shared this position with me.

Thanks to Dr. Ulrich Reuter, Rainer Kapp and Dr. Rayk Rinke from the Department of Environmental Protection Stuttgart for the excellent teamwork and sharing of data and to Hugo Denier van der Gon (TNO) for chemical input data. This work was funded by EU-Project 3CE292P3 – 'UHI - Development and application of mitigation and adaptation strategies and measures for counteracting the global UHI phenomenon', implemented through the CENTRAL EUROPE Programme, co-financed by the ERDF. I like to thank all colleagues from NOAA in Boulder, CO, especially Dr. Georg Grell who let me join his working group for four months. Many thanks to the Mathematisch-Naturwissen-schaftlichen Fakultät der Universität zu Köln, in particular to Prof. Dr. Michael Kerschgens for giving me the opportunity to obtain my PHD from the faculty. The membership within the KIT Graduate School for Climate and Environment (GRACE) gave me extra financial support and advanced training opportunities.

Special thanks to Katja, Matthias, Janina, Carsten, Fabi, Andi, Benni, Tom, Ula, Petra etc. for the informal everyday meetings and Marco, Ling and Mia for a great time in Boulder. Thanks to the band members of DaGapo, the IFU-Football team and everybody in the institute who shared conversations with me.

Last but not least I thank my family and friends who supported me during the whole period of my PHD. Any time, they acknowledged my work and encouraged me to carry on. My parents, brother and sisters, who offered me all the support I needed and my friends Thomas and Philipp who have been around me since the early school years.

Table of Contents

Acronyms

AR	Assessment Report
BEP	Building Effect Parameterization
CBD	Central Business District
CBL	Convectively-driven Boundary Layer
CCN	Cloud Condensation Nuclei
CFL	Courant-Friedrichs-Levy
CFL	Constant Flux Layer
CPU	Central processing unit
DEM	Digital Elevation Model
DESIREX	Dual-use European Security IR Experiment 2008
DW	Downwind
ECMWF	European Centre for Medium Range Weather Forecast
EEA	European Energy Agency
ERA	European Reanalysis
ERDF	European Regional Development Fund
GAINS	Greenhouse Gas - Air Pollution Interactions and Synergies
GMES	Global Monitoring for Environment and Security
GDP	Gross Domestic Product
HPC	High performance cluster
IEA	International Energy Agency
IPCC	Intergovernmental Panel on Climate Change
LSM	Land Surface Model
LAI	Leaf Area Index
MACC	Monitoring Atmospheric Chemical Composition
MEGAN	Model of Gases and Aerosols from Nature
MOST	Monin-Obukhov Similarity Theory
MOZART	Model of Ozone and Related Chemical Tracers
NOAA	National Oceanographic and Atmospheric Administration
NWP	Numerical Weather Prediction
OECD	Organisation for Economic Co-operation and Development

OPE	Ozone Production Efficiency
PBL	Planetary Boundary Layer
PDF	Probability Density Function
PET	Physiological Equivalent Temperature
PFT	Plant Functional Type
RADM	Regional Acid Emission Module
RANS	Reynolds Averaged Navier Stokes Equations
RCP	Representative Concentration Pathway
SIA	Secondary Inorganic Aerosols
SLUCM	Single Layer Urban Canopy Model
SNAP	Standardized Nomenclature for Air Pollutants
SOA	Secondary Organic Aerosols
SRES	Special Report on Emissions Scenarios
SVF	Sky View Factor
TKE	Turbulent Kinetic Energy
TNO	Netherlands Organisation for Applied Scientific Research
TOA	Top of the atmosphere
TSP	Total suspended particulate matter
UBL	Urban Boundary Layer
UCL	Urban Canopy Layer
UCM	Urban Canopy Model
UHI	Urban Heat Island
UHII	Urban Heat Island Intensity
UN	United Nations
URL	Urban Roughness Layer
USGS	US Geological Survey
UW	Upwind
WHO	World Health Organization
WRF	Weather Research and Forecasting Model
WW2	World War 2

Notation

A	empirical pre-exponential parameter [cm^3 $molecule^{-1}s^{-1}$]
α	albedo [%]
c	heat capacity[J kg^{-1} K^{-1}]
ε	emissivity [%]
E	emission for one grid cell [mol $km^{-2}h^{-1}$]
G_Z	ground heat flux [Wm^{-2}]
H	building height [m]
H	sensible heat flux [Wm^{-2}]
H_G	sensible heat flux ground [Wm^{-2}]
H_W	sensible heat flux wall [Wm^{-2}]
hν	quantum energy [J]
Θ	solar incidence angle [°]
Θ	potential temperature [°C]
H_{Wall}	heat flux wall [Wm^{-2}]
H_{Ground}	heat flux ground [Wm^{-2}]
i	general subscript
j	general subscript
k	general subscript
λ	thermal conductivity [W m^{-1} K^{-1}]
λ	emission activity factor [-]
λ_{CE}	canopy environment emission activity factor [-]
λ_{age}	leaf age emission activity factor [-]
λ_{SM}	soil moisture emission activity factor [-]
L^*	net long wave radiation at the surface [Wm^{-2}]
L↓	downward net long wave flux [Wm^{-2}]
L	turbulent length scale [m]
Q*	total incoming solar radiation [Wm^{-2}]
Q_F	anthropogenic heat [Wm^{-2}]
Q_E	latent heat [Wm^{-2}]
Q_H	sensible heat [Wm^{-2}]
ΔQ_S	heat storage [Wm^{-2}]

Q_{total}	total energy from canyon [Wm^{-2}]
Q_{wall}	total energy from wall [Wm^{-2}]
Q_{floor}	total energy from floor [Wm^{-2}]
ρ	density [kg m^{-3}]
ρ_{iso}	canopy loss and production factor
R	ideal gas constant [J $K^{-1}mol^{-1}$]
r_s	stomata resistance [sm^{-1}]
r_m	mesophyll resistance representing [sm^{-1}]
r_{lu}	resistance of the outer surfaces in the canopy [sm^{-1}]
r_{dc}	deep canopy resistance [sm^{-1}]
r_{lc}	lower canopy resistance [sm^{-1}]
r_{ac}	canopy height resistance [sm^{-1}]
r_{gs}	ground surface resistance [sm^{-1}]
σ	Boltzmann constant [$Wm^{-2}K^{-4}$]
S_R	incoming solar radiation [Wm^{-2}]
S_D	direct radiation [Wm^{-2}]
S_Q	diffuse radiation [Wm^{-2}]
SF	scaling factor [-]
$\Delta T_{(u\text{-}r(max))}$	maximum urban heat island [K]
T_s	surface temperature [K]
T_{wall}	wall temperature [K]
T_{total}	total temperature [K]
V	volume of air in a grid cell [m^3]
W	building width [m]
Δx	grid spacing [m]
Ψ_s	sky view factor [-]
Ψ_w	wall view factor [-]
ω	area average factor [-]
z	height [m]
ZR	building height [m]

List of Figures

List of Tables

1. Introduction

"As soon as I had escaped the heavy air of Rome and the stench of its smoky chimneys, which when stirred poured forth whatever pestilent vapours and soot they held enclosed, I felt a change in my disposition." (Seneca, AD 61)

'[…] in the denser parts of the metropolis, the heat is raised, by the effect of the population and fires […] and it must be proportionally affected in the suburban parts […]' (Howard L. 1833: The Climate of London)

The roman philosopher Seneca (4 B.C. - 61 A.D.) stated the negative effect of urban air pollution for the inhabitants of the city of Rome during the age of the Roman Empire.

Luke Howard was the first to provide evidence that urban temperatures are elevated compared to the rural surroundings. Based on continuous measurements within the city of London and suburbs, he was the first to describe a phenomenon which was scientifically characterized as the Urban Heat Island (UHI) (Oke 1973) . With his concise statement of the temporal variation of urban-rural temperature differences and the analysis of spatial patterns, he laid the foundation for scientific research in the field of Urban Climate (Mills 2008). Since these times, a vast amount of studies have been performed, covering different fields (Solomon 2007), aspects and geographic regions. Urban climate has been explicitly treated in the recent IPCC Reports (AR4 and AR5) (Stocker et al. 2013).

We are living in a world of growing population and urbanization has become the key indicator of human development around the globe. Until 2050, the fraction of global urban population will increase to over 69% (Europe 82%), which means that about 6.3 billion people are expected to live in urban areas (United Nations 2012). Being the centres of human activity, urban areas are especially vulnerable to climate change and air pollution.

To maintain sustainable development and to cope with the growing population pressure, urban systems are reliant on a constant energy supply, which still is achieved mainly by burning of fossil fuels. Although covering less than 3 % of the land surface, cities are the main contributor to global greenhouse gas emissions. With 78 % of total global carbon emissions, they are heavily implicated in global climate change (Grimm et al. 2008). Urban agglomerations, which have grown rapidly over the last decades, now have to cope with a self-induced effect. If there is an impact of climate change on human beings, this impact will essentially affect urban environments (Stone Jr 2012).

According to city size, building structures and population density, a city creates its own microclimate which can differ from the rural surrounding. The conventional structure of a city is characterized by its road networks, public transportation system and architectural properties. This requires natural open areas to be replaced by impervious sealed surfaces like concrete and asphalt. Surface sealing changes the hydrological properties of an area. Runoff rates are increased and evaporation is reduced significantly. Next to this, urban materials tend to absorb the bulk of the incoming thermal radiation leading to the extensive accumulation of heat. The buildings act as obstacles for air circulation and heat can be trapped within street canyons where it can even remain hours after sunset. Additionally, anthropogenic heat amplifies the excessive warming of urban areas, which can in turn promote the formation of secondary circulation patterns between city and surroundings (Arnfield 2003). The annual mean temperature of central areas of a large city is about 1° to 3 °C higher than in the surrounding areas. In individual calm clear nights, it even can be up to 12 °C higher (Oke 1982a).

The UHI raises the demands of energy supply for air conditioning in summer periods. Air pollution correspondingly increases as connected with power plants and transportation relying on fossil fuels. According to the city structure and meteorological conditions, air pollutants can either remain within the city for long periods or be transported into the rural surrounding either by wind or via induced secondary circulation due to the urban-rural temperature gradient. Further, chemical reactions can be accelerated by the additional heat.

With increased urban growth and traffic volume, heat stress and worsened air quality have also developed into major problems in urban areas located in Europe. Older people and infants tend to suffer most from excessive heating. The European Heat Wave in the summer of 2003 developed into the single most catastrophic weather event to have haunted Europe since the beginning of weather observations. The EU estimated that more than 70,000 people within 12 countries died from heat related illnesses, more than ever recorded in a single event since WW2. Remarkably, Italy and France - two of the most developed and medically advanced societies in the world - alone witnessed over 40,000 deaths. Because of France being one of the countries having suffered the most from the heat wave, this phenomenon often is referred to *'La Canicule'* (Stone Jr 2012) .

In order to improve living conditions in future urban environments, adaptation and mitigation strategies discussed in scientific, and social, political and economic

communities. Adaptation demands the adjustment of our habits and way of living to the changed climatic conditions. Mitigation implies the direct intervention into the system, to identify problems and to reduce negative aspects.

Several mitigation strategies have been discussed in the scientific community to reduce urban temperature and urban heat islands. White roofs and highly reflective façades tend to reflect incoming solar radiation, which in turn leads to a reduction of surface warming (Taha 1997b). The cooling of the building also reduces the amount of energy needed for air conditioning (Akbari et al. 1997). Planted roofs or generally vegetated surfaces transform sensible into latent heat via evaporation, leading to a net cooling. Another way to reduce urban temperatures is the modification of the building structure itself, which includes the orientation and specific characteristics of the building and road orientations to create fresh air corridors and facilitate air circulation.

Several numerical and experimental studies have been carried out in the past to confirm the positive effect of these strategies. Taha (1997b) discussed the impacts of surface albedo, evapotranspiration and anthropogenic heating. By analysing numerical simulations and measurements, he indicated that increasing vegetation cover can effectively reduce the surface and near surface temperature. By combining low altitude flight measurements and a mesoscale model, he demonstrated that increasing the albedo by 0.15 can reduce peak summertime temperatures for the urban area of Los Angeles by up to 1.5 °C. During the DESIREX Campaign 2008, Salamanca et al. (2012) simulated, that a higher albedo leads to a 5% reduction in energy consumption through air conditioning during summertime periods for the area of Madrid. Solecki et al. (2005) studied extensively the effect of urban vegetation in New Jersey by a GIS-based model application, while Zhou et al. (2010) numerically simulated the UHI of Atlanta under extreme heat conditions and stated that increasing the vegetation fraction and evapotranspiration are the most effective mitigation strategies for that area. The energy saving aspect of highly reflective surfaces is simulated on a more global perspective in Akbari et al. (2009) and Oleson et al. (2010), who treated white roofs in a global climate model as subgrid phenomena also accounting for air conditioning and heating demand. Jacobson et al. (2011) used a global model to analyse the effect of urban surfaces and white roofs on global and regional climate.

On the side of experimental studies, Onishi et al. (2010) evaluated the potential for UHI mitigation by greening parking lots in the city of Nagoya, Japan by analysing land surface

temperature retrieved from a broad range of remote sensing datasets. The regional energy saving effect of high-albedo roofs can also be found in Akbari et al. (1997) who was running experimental measurements of microclimate and energy use at selected buildings.

It is well established that urban heat island mitigation strategies have an effect on dynamical processes in the urban canopy layer, whereas the effect on chemical reactions is not yet fully understood. The relation between the urban heat island and air quality is investigated in Lai and Cheng (2009) who showed that the concentration of pollutants increases with the UHI under certain prevailing weather conditions. Taha (1997a) pointed out that peak ozone concentrations at 3 p.m. can decrease by up to 7% with a massive increase of surface albedo, whereas Akbari et al. (2001) stated that urban trees and high-reflective roofs can significantly reduce energy consumption, thus improving air quality.

Analysing the effect of urban heat island mitigation strategies on urban air quality is the main focus of this dissertation. For this reason, the mesoscale numerical model WRF (Weather Research and Forecasting Model (Skamarock et al. 2005)) and the chemical model WRF-Chem (Grell et al. 2005) are used to analyse the urban climate and air quality on a regional scale. Different parameterization schemes are available in WRF to represent urban surfaces and dynamical processes in the urban atmosphere. (Chen et al. 2011a). A way of incorporating high resolution land use data is presented and the modification of an urban canopy model according to local urban properties is discussed. The first part deals with the effect of UHI mitigation strategies on local meteorology and dynamical processes by simulating different urban planning scenarios with regard to a medium sized European city (Stuttgart) during an extreme heat event. The basic results are presented in Fallmann et al. (2014). The second part discusses the effect of these strategies on the chemical composition of the urban air. Local observations from the city of Stuttgart are used to calibrate the model and evaluate the simulations.

The new contribution to the scientific field however will be the incorporation of high resolution land use data and the coupling of an urban canopy model to the chemical model WRF-Chem (Grell et al. 2005) for assessing the effect of certain urban planning scenarios on urban air quality on a regional scale. It is the first study of this kind to be performed for the urban area of Stuttgart and thus acts as test case for future simulations. Different studies have been carried out in the past, dealing with the effect of UHI mitigation strategies mainly on ozone concentrations (e.g. Akbari 2001). This study however extends

the analysis towards secondary effects on primary pollutants such as carbon monoxide, nitrogen oxides and particulate matter coming along with a reduction of the urban temperature.

The study is funded by the EU-Project 3CE292P3 – ‘UHI - Development and application of mitigation and adaptation strategies and measures for counteracting the global UHI phenomenon’. This project is implemented through the CENTRAL EUROPE Programme co-financed by the ERDF. Within eight pilot areas, the project aims to develop strategies and policies for adaption and mitigation of the risks arising from urban heat island formation while being in close transnational discussion with policy makers, local stakeholders and professionals. The urban area of Stuttgart is one of the participating pilot regions and serves as test bed for executing model simulations.

Local processes and interactions like heat islands and urban air quality are driven by boundary conditions from larger scales. Hence, the understanding of small scale phenomena requires an explanation of the broader context in advance.

2. Global Background

2.1 Climate Change

According to the IPCC Fifth Assessment Report AR5 '[…] each of the last three decades has been successively warmer than the preceding one. […] and human influence has been detected in warming of the atmosphere and the ocean […], and in changes in some climate extremes.[…] It is very likely, that the increased CO_2 concentrations have led to a global warming trend in the last century[…]' (Stocker et al. 2013).

The burning of oil, gas, coal and forests has been the driving force of industrial development since the middle of the 19th century. This created an imbalance in the carbon cycle so that the input into the system happens more rapidly than CO_2 is being removed by assimilation processes in the ocean or terrestrial system. An additional anthropogenic greenhouse effect is generated which causes global temperatures to rise. The steady increase of atmospheric CO_2 concentrations has been monitored at the Mauna Loa Observatory in Hawaii since the 1950s when 315 parts per million (ppm) was measured compared with 392 ppm in 2012 (Stone Jr 2012).

In order to project future climate conditions, scenarios of human activities and future socio-economic behaviour of the world population and economy have to be defined. In comparison with AR4 (Solomon 2007) in the Fifth Assessment Report (AR5), the scientific community has developed new ways to characterize future developments by defining four new scenarios following the theory of Representative Concentration Pathways (RCP) (Moss et al. 2010). Each pathway is identified by its approximate radiative forcing in the year 2100 relative to 1750 and represents a range of 21st century climate policies resulting in different intensities of greenhouse gas emissions. Radiative forcing describes the net irradiance at the top of the atmosphere (TOA) calculated from downward minus upward fractions and is modified by the change in concentrations of chemical constituents like carbon dioxide (Stocker et al. 2013)

Following the outcome of IPCC AR5, global surface temperature change for the end of the 21st century is likely to rise by 1.5 - 4 °C relative to the period 1850-1900 for all scenarios. With regard to global mean sea level rise, the range of values reaches from 0.24 to 0.3 cm and from 0.4 to 0.63 cm, respectively. The global CO_2 level is supposed to rise from about 300 ppm historically to over 900 ppm at most in 2100 (Fig. 1) (Stocker et al. 2013).

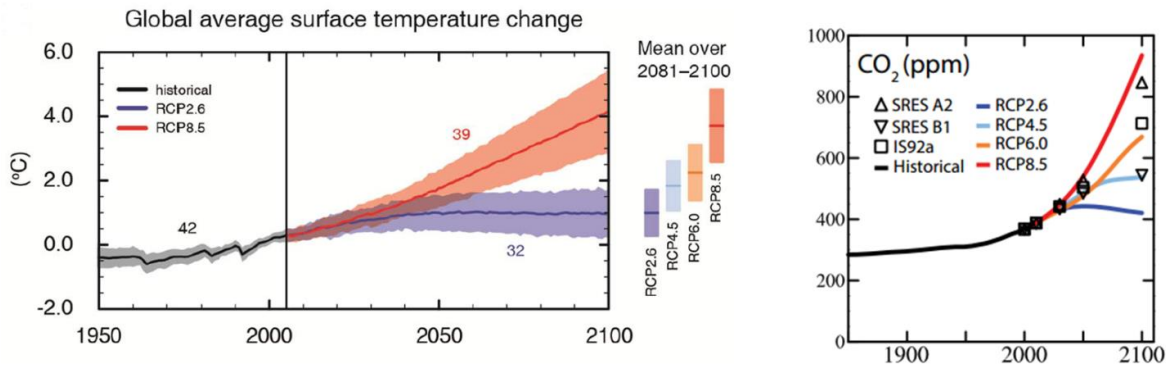

Fig. 1: Projected temperature (left) and CO_2 (right) increase for each RCP Scenario (Stocker et al. 2013)

Due to elevated temperatures, secondary effects will be generated and amplified which will in turn also affect urban environments. The number of summer precipitation events is supposed to decrease, whereas winter months will register an increase. Heavy thunderstorms and very heavy precipitation events will occur more often in the future. An increased frequency of thermal extremes as well as an increase in duration, frequency and intensity of heat waves is very likely. Next to the rising temperature itself, elevated concentrations of air pollutants can become harmful to human health (Kuttler 2012; Solomon 2007). How extreme events affect societies was dramatically proven by the European Heat Wave 2003. Around 2002 heat-related deaths were recorded on a single day in August alone in France, 600 in Spain and another 250 in four Italian cities. Nearly 650,000 ha of land had been destroyed by fires by the end of summer 2003 and the impact on harvest and livestock was dramatic. Massive drought has led to water scarcity where falling river levels affected important European trade routes. The financial loss resulting from the heat wave is estimated to be about $13 billion, which is maybe still underestimating the true costs. Not only the human body, but also urban infrastructure can suffer from long periods with elevated heat stress which can result in distortions of construction materials of buildings or public transportation and derogate electrical power supply (Stone Jr 2012). Urban environments will suffer from climate change and moreover, the risks are amplified by human activities.

2.2 Population growth and urbanization

Next to rising temperatures, the planet has to face a constantly increasing pressure of the global population on land and resources. Since the beginning of the 19th century, the number of people living on Earth has grown from one to over seven billion today and is expected to increase by another 2.3 billion till 2050. Additionally, urbanization demands the transformation of natural landscape to sealed areas leading to a loss of huge amounts of biosphere.

From 1950 till 2010, the percentage of people residing in cities has increased from 30 % to 52 % and is projected to exceed 67 % by 2050. Less developed countries will have to face especially dramatic problems when the standard of development cannot keep pace with the demands of the fast growing population. The number of megacities with at least 10 million inhabitants will increase. With Tokyo (23.3 million) and New York (16.2 million) in the year 1970, only two megacities existed. This number increased to 10 in 1990, up to 23 in 2011 and is expected to rise to 37 in 2025. At present with 37.2 million people, Tokyo is ranked first globally. The three countries with the largest increase in urban population between 2000 and 2050 will be India, followed by China and Nigeria (United Nations 2012).

Between 1970 and 2011, the number of people living in megacities has grown from 39.5 to 359.4 million and is expected to almost double to 630 million by 2025, meaning one in 13 people will be living in a megacity. These huge urban agglomerations are dynamical systems which react to the projected climate change in all its facets (United Nations 2012)

Although urban areas only cover a small fraction of the land surface, it is assumed that they contribute to climate change. According to Kalnay et al. (2003), the impact of urbanization on temperature trends in the continental United States accounts for 0.06 and 0.15 °C per century, depending on the method; one is based on population data, the other on satellite measurements of night light.

Based on the United Nations World Urbanization Prospects 2011 Revision Report (United Nations 2012), in 2011 60 % or about 890 million people were living in areas with a high risk of being affected by natural hazards. Flooding is seen as the most frequent and intense hazard when climate change amplifies the frequency of extreme weather events and the sea

level rises due to global warming. Droughts, which can evoke heat waves, are ranked in second place.

The vulnerability of urban population to climate change is not only related to the growing number itself, but also to an over-aging of the population which happens particularly in OECD countries. By 2050, about 25 % of the people are projected to be older than 65 compared to 15 % today. This massive aging of the population will bring a range of new problems to urban areas regarding the health sector, especially in periods of extreme weather events or heavy air pollution (United Nations 2012).

2.3 Energy consumption and air quality

Cities are dynamic systems which have to constantly satisfy the needs of their inhabitants concerning residential, transportation and economic sectors. Each sector claims a huge demand of energy. With an annual average growth rate of the Gross Domestic Productivity (GDP) of 3.6 %, the global need for energy consumption is expected to increase dramatically within the next 50 years (OECD 2012).

In 2010, the building sector (excluding industrial facilities) consumed more than 20 % of the global delivered energy. Due to the rapid growth of urban systems along with changes in living standards and economic conditions, the energy growth in the building sector is the fastest throughout all projections of the International Energy Agency (IEA). The total global energy demand for buildings shows an annual growth rate of 1.6 percent per year. Although in OECD countries this increase is less intense, in fast growing non-OECD countries this number can rise up to 2.7 %, accounting for nearly 80 percent of the growth in the world's total building sector energy consumption (Birol 2013).

About 85 % of the world's energy is still supplied by fossil fuels like oil, gas and coal. Resources are exploited and renewable energy still does not have the efficiency to fill the gap when the economically viable energy from oil and gas reserves are depleted (Visser et al. 2009).

According to projections of the OECD – Transport Outlook 2011, an increasing level of globalization will lead passenger mobility to triple by 2050. Expecting the global number of cars to rise from 700 million (2011) to nearly 2 billion in 2050, CO_2 emissions from

vehicle use are also assumed to triple despite new technologies for fuel and emission reduction can be effectively used (OECD 2011). In the European Union, CO2 emissions from road transport are responsible for approximately one fifth of the EU's total emissions. Between 1990 and 2010, they have increased by 23 % (Guerreiro et al. 2013).

Nitrogen oxides, volatile organic compounds (VOC) which result from incomplete combustion of fuel and photochemical oxidants like ozone are mainly connected to increased traffic in the urbanized world (Fenger 1999). For cities acting as sources of emissions, ambient concentrations can have widespread effects on human health, urban and regional visibility, ecosystem degradation and on a broader scale, regional climate change and global pollutant transport. (Molina and Molina 2004)

When mobility and social standards are increasing, urban dwellers expand their activities well beyond the city borders, leading to an increase in the ecological footprint and resulting in a constantly increasing pressure on the surrounding ecosystem (Grimm et al. 2008).

3. The Urban Climate

3.1 Introduction

Urban climates significantly differ from those of rural areas, depending on prevailing weather conditions, building geometry and material, anthropogenic heat sources and thermo-physical characteristics (Taha 1997b). Urban climatology as defined in Oke (1987) addresses the mass, momentum and energy transfer through an urban area and entails modified physical variables like temperature, humidity or wind speed which alter circulation patterns, chemical reactions and transport of pollutants.

The analysis of a vast amount of observational data reveals that urban areas in the northern hemisphere annually have an average of 12 % less solar radiation, 8 % more clouds, 14 % more rainfall, 10 % more snowfall and 15 % more thunderstorms compared with the rural surrounding. Urban temperatures can be on average 2 °C higher and the concentration of air pollutants can exceed those of an ‘undisturbed’ atmosphere by 10 times. Evapotranspiration rates from sealed surfaces can be decreased by up to 60% and summertime humidity by 20%. Obviously, fluxes of heat, moisture and momentum are

modified by the urban canopy and are even further enhanced by human activities (Taha 1997b).

The feedback of global processes to the regional and urban scale is closely coupled to the city's orientation, shape and complex morphology. Due to a high degree of heterogeneity, urban areas offer a great diversity of surfaces and a broad range of spatial scales, which leads to diverse effects in the energy balance. The physical mechanisms responsible for the modification of the regional and local climate occur and interact on different scales both in time and spatial dimensions (Britter and Hanna 2003).

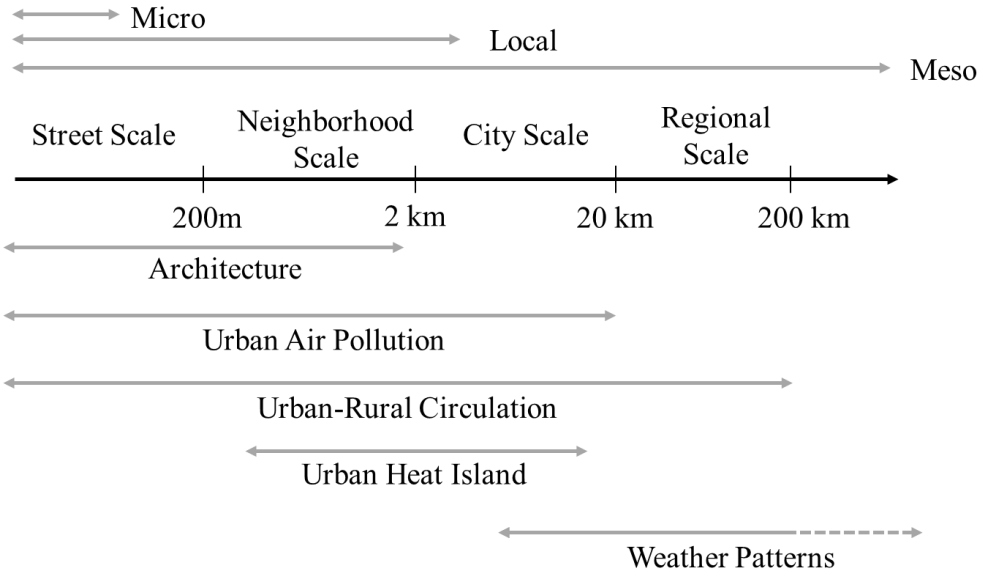

Fig. 2: Interactions across scales in atmospheric modelling (Britter & Hanna 2003)

The time scales range from one second and below for turbulent motions, over hours for the formation of convective cells which produce cumulus clouds, to seasonal or yearly time scales.

Urban-rural interactions and circulation patterns influenced by the urban heat island occur from meso to sub-meso or regional scales and directly affect the regional climate by modifying weather patterns. Urban air pollution and the effect of increased heat on human health reach from the neighbourhood down to the street scale with processes differing between street canyons. A heat island itself can occur on different scales; around a single building, city quarter or the whole urban canopy.

The elevated urban temperatures for urban dwellers may be beneficial in winter periods due to a decreased heating load as well as a reduced snow or ice loading on urban roads. However, the negative aspects concerning heat stress such as an increased energy consumption for cooling and a diminished air quality are dominating factors (Taha 1997b).

Temperature as perceived by human beings depends on a number of factors. Next to the measured temperature itself, factors like moisture, exposure, physiological conditions, clothing and behaviour define the physiological equivalent temperature (PET) which serves as an indicator for the well-being of urban dwellers and characterizes a key parameter in the research field of biometeorology (Höppe and Hurk 1999).

Atmospheric characteristics mirror distinct features of the urban canopy underneath, which leads to the formation of characteristic layers (Fig. 5). According to Oke (1987), the urban atmosphere can be divided into an urban canopy layer (UCL) and an urban boundary layer (UBL), although the transitions can be poorly defined. The UCL which also includes the skin of the urban surface extends from the ground up to the mean roof level and is dominated by absorption and reflection processes within the urban canopy. Per definition it is part of the planetary boundary layer (PBL). The PBL or mixing layer refers to the air volume near the ground that is directly affected by diurnal heat, moisture or momentum transfer to or from the surface. Within this compartment of air, turbulent motion is high and vertical mixing is strong. The top of the boundary layer is characterized by a temperature inversion, a change in air mass, a rapid change in moisture and wind speed and/or wind direction.

Heat propagating through the building material and the ground surface can be accumulated in deeper layers beneath the surface which can lead to warming there. Interactions and processes in the urban atmosphere induced by the presence of a city are expressed as mesoscale for urban-rural interaction, to a local scale for city quarter interaction, down to micro scale processes within urban canyons.

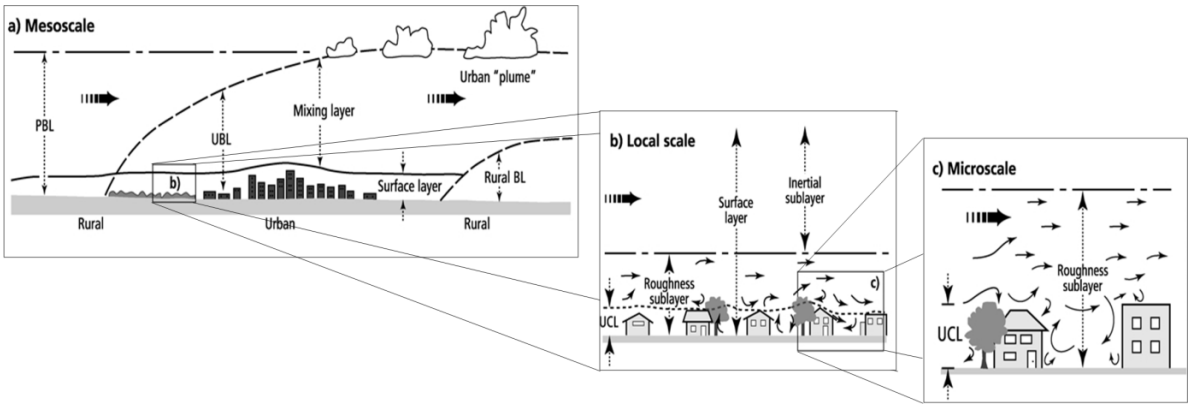

Fig. 3: Urban environments in atmospheric processes across a range of scales (Oke 1987)

In Section 3.2, the Urban Heat Island is defined based upon its physical nature, energetic basis, attached problems and risks related to heat and air quality. Moreover, mitigation strategies are defined and discussed in Section 3.3.

3.2 Urban heat island characteristics

The atmospheric state is a response to the exchange of sensible and latent heat and mass and momentum. In urban areas, the sources and sinks for these exchanges originate from interactions in a heterogeneous environment, involving natural as well as anthropogenic factors. The urban heat island is a regional climate phenomenon induced by the radiative properties of impervious surfaces, leading to aggravated heat accumulation and a positive temperature difference between the urban area and rural surroundings. The urban heat island can be clearly distinguished by analysing the surface temperatures of an urban surface in comparison with the rural surroundings. Isotherms for near surface air temperatures reveal a sharp border between the urban and rural environment which leads to the analogy of an ‘island’ (Fig. 4).

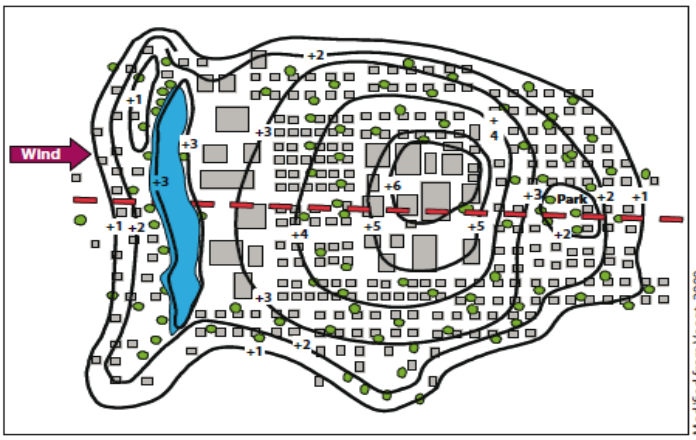

Fig. 4: Contour lines of equal UHI Intensity (EPA 2013)

The horizontal temperature gradient throughout the urban area reflects the city structure while revealing areas of higher building density, whereas single urban parks or lakes might lead to detached cool spots (Voogt and Oke 2003). However, the shape and the characteristics of the UHI are strongly connected to the diurnal cycle of incoming shortwave radiation. Due to rapid night-time cooling of the rural surrounding and the high heat storage capacity of impervious surfaces, the difference in near surface air temperature is highest during the evening and night. Hence, the UHI is mostly pronounced at night and in the periods around sunset and sunrise. In urban areas, warming and cooling rates are generally smaller which leads to a damping of the diurnal temperature curve. Urban areas are characterized by low wind speeds that are especially pronounced when fresh air corridors are blocked by buildings or naturally by morphological features that hinder air mixing and cooling while further promoting the heating of surfaces and temperatures.

Next to the geographical location of a city, topographic features, the nature of soils, vegetation and land use, there is an evident relation between the heat island intensity and the city size or population density.

With population density (P) being an indicator for the size of a city, Oke (1973) found a logarithmic relationship between city size and the UHI intensity. Analyzing the maximum heat island (given as $\Delta T_{u\text{-}r(max)}$) for 11 European cities with more than 50,000 inhabitants, he identified a simple formula:

$$\Delta T_{u-r(max)} = 2.01\, log_{10}\, P - 4.06. \qquad (3.1)$$

Furthermore, there are predominant weather situations which amplify or attenuate the urban heat island intensity. Wind speeds are able to increase or reduce UHI intensities. Low clouds are, for example, more effective in limiting the heat island extent than high clouds of the same amount (Oke 1982). The special topographic situation of Stuttgart makes it well suited for conducting urban climate studies because it sets an important boundary condition for UHI formation. Because heat can especially be trapped in the valley and elevated rural regions in the surrounding produce large pools of cold air, the difference between urban and rural temperature is well pronounced.

3.3 Energetic basis of the urban atmosphere

In contrast to urban environments, the energy balance of natural landscapes is well understood. The energetic processes are predominantly driven by the surface net radiant flux density, which itself is dominated by the incoming short wave radiation at day and outgoing long-wave radiation at night. The heat exchange is dependent on the properties of the soil, the volumetric water content, the morphology, vegetation cover and the state of the atmosphere such as the level of turbulence, which itself is driven by numerous factors. The partitioning of turbulent transport between sensible and latent heat is expressed by the Bowen ratio and is regulated by surface moisture availability (Oke 1987).

Different urban features promote changes in the energy balance which leads to positive thermal anomalies. Through the exchange of energy, mass and momentum, urban environments generate their own microclimate, causing the formation of a distinct urban boundary layer (UBL), which itself can be divided into different sub layers (Fig. 5). The transitions however can be fluid. The understanding of the formation of these layers is important for understanding the effect of the UHI and its connected processes and interactions, as well as the effect on formation and dispersion of pollutants which determine the urban air quality.

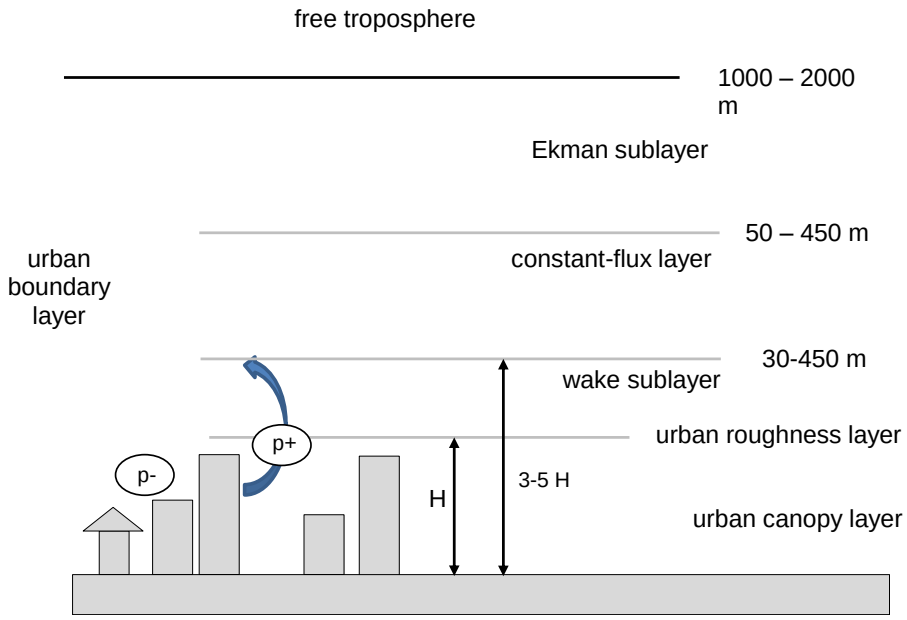

Fig. 5: Schematic of the vertical layering of the urban boundary layer (UBL). H represents the average building height, p+ and p- indicate atmospheric pressure disturbances upstream and downstream of buildings (redrawn from Emeis 2010)

According to Emeis (2010), four characteristic layers evolve in an urban boundary layer. The urban canopy layer extends up to the maximum building height. The attached wake sublayer reaches up to 3-5 m of the building height, where the influence of single buildings on the flow is still present. Both layers can be merged to the urban roughness layer (URL) which is characterized by strong vertical exchange. Above the region of constant flux (constant flux layer CFL or Prandtl layer) the wind direction turns into the direction of the geostrophic wind, which can be defined as Ekman layer. In case of the formation of a convectively driven boundary layer (CBL), the CFL and the Ekman layer combine to form the mixing layer.

The energy balance of any surface on earth is driven by its radiative properties. They are responsible for distribution of the incoming shortwave solar irradiation into single components of absorbed, reflected and stored heat during the day. At night, long-wave radiation exchange is dominating. Impervious surfaces tend to absorb the bulk of the incoming radiation which results in warming of the surface and the near surface atmospheric layer. Urbanization implies the transformation of natural surfaces into massive heat reservoirs, which in addition to building geometries, weather patterns and enhanced human activities, leads to an increased warming compared with their rural surrounding. The energy balance of a surface can be partitioned into different parts according to:

$$Q^*(1-a) + L^* + Q_F = Q_E + Q_H + \Delta Q_S (+Q_G) \quad (3.2)$$

Where Q^* is the total incoming shortwave radiation hitting the surface. A term which is introduced here is the Albedo *a*, indicating the percentage of incident shortwave radiation being reflected from the surface and therefore characterizing the warming potential of the surface. The inverse part of the albedo multiplied by the total incoming solar radiation Q^* defines the total shortwave rest-energy. L^* is the net long wave radiation at the surface and Q_F the heat release by human activities added to the natural heat flux. This term cannot be measured directly, but must be calculated from a fuel use inventory for instance. Typically, it ranges from 5 W/m² in the suburbs to about 50 W/m² in the city centre with an increase from night to day time by about a factor of 3 (Oke 1982b). The energy leaving the surface is divided into a latent heat part Q_E and a sensible heat part Q_H. The ΔQ_S term corresponds to that portion which is stored in the system. The ground heat flux Q_G is further added as a term on the right hand side of the equation as a part of the net ΔQ_S term (Oke 1982b).

Energetic aspects of an urban street canyon need to include the impact of three active surfaces – two walls and a floor (considering a two-dimensional model). By this, the area which is exposed to exchange processes is increased so that the distribution of direct-beam solar radiation is complicated by radiative interactions between the surfaces, loss of long-wave radiation to the sky and modification of the turbulent flow (Oke 1981a). According to its orientation, structure and geometry, each single canyon can create its own microclimate. The diurnal change of the insulation angle evokes different peaks of energy flux densities according to the reflection at the ground and wall surfaces. However, the floor is the most active energy exchange surface. The total received energy from an urban canyon (Q_{total}) is dependent on the sky-view factor, simplified as the ratio between building height *(H)* and road width *(W)* and is the sum of the predominant fluxes at the walls (Q_{wall}) and the floor (Q_{floor}):

$$Q_{total} = 2Q_{wall}\left(\frac{H}{W}\right) + Q_{floor}. \quad (3.3)$$

Moisture availability is one of the key variables controlling the energy balance of an urban canopy. By the presence of vegetation, the water retention potential is increased, whereas plant canopies show a buffering and moderating influence on the wet/dry behaviour of the soil and the surface. Wherever moisture is removed by surface runoff from impervious surfaces, water storage in natural soils and plants is no longer available for evaporative

cooling (Oke 1982b). Increased soil moisture can significantly reduce surface temperatures, which decreases the sensible heat input to the urban canopy layer and consequently leads to reduced urban heat island intensities. Case studies for the urban area of Selangor, Malaysia illustrate that soil moisture alone can have the same effect on UHI formation as natural green surfaces (Ahmad and Hashim 2007).

The heat storage ΔQ_S in the building materials is strongly controlled by their thermal conductivities, heat capacities and the density of the material. A parameter which combines these properties is the thermal admittance μ or thermal inertia of a material. It describes the ability to store and conduct heat energy away from the surface during the day and return heat energy back during the night (Mellon et al. 2000).

In general, energetic properties of the urban canopy layer are dependent on the immediate site character. The heat budget of the UBL is controlled by both advective and convective transport of sensible heat from the ground surface and urban canopy. Additional sensible heat can originate from the entrainment from higher layers and from internal radiative effects. The convergence of heat due to excessive surface warming during the day results in an increasing depth and temperature of the daytime convective mixed layer. The increase of the urban mixing layer height is both triggered by radiative effects due to the presence of aerosols and convective effects due to horizontal and vertical transport and mixing. Both mechanisms are enhanced in the urban boundary layer. Convective heat plumes are generated by an increased sensible heat flux from the city surface caused by increased urban turbulence intensities (Oke 1982b). In special cases, horizontal flow can transport the urban heat plume downwind of the city and the urban boundary layer can be lifted over the attached rural boundary layer, thereby modifying its properties (Fig. 6). The temperature increase is not limited to the urban area itself as it can affect the rural surrounding to the order of kilometres with regard to prevailing wind direction- and speed (Voogt & Oke 2003).

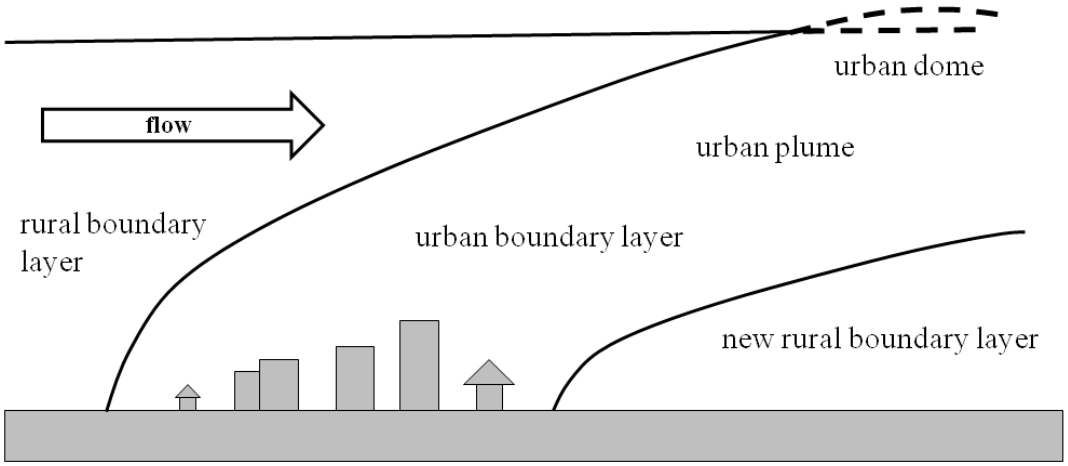

Fig. 6: Urban plume downwind of a large city (redrawn from Emeis 2010)

By mid-afternoon, the UBL can reach 500-1500 m in depth depending on the stability of the air masses. Shortly before sunset, the surface is cooling and the stability of the UBL increases. Over the stable boundary layer, a residual layer can remain as a left over from the daytime convective mixed layer. Because it does not get in contact with the ground, this layer is not counted to the UBL. As surface cooling continues, a stable nocturnal boundary layer develops within the first 200 m or less, being characterized by strong stability, weak turbulence and weak surface wind speeds. This shallow stable layer can also be called a radiation inversion (Stull 1988). Due to weak air mixing, air pollutants can be trapped and increase the local concentrations. They can remain in this layer during the night to return again on the next day by vertical mixing. A scheme of the diurnal evolution of the atmospheric boundary layer is indicated in Figure 7.

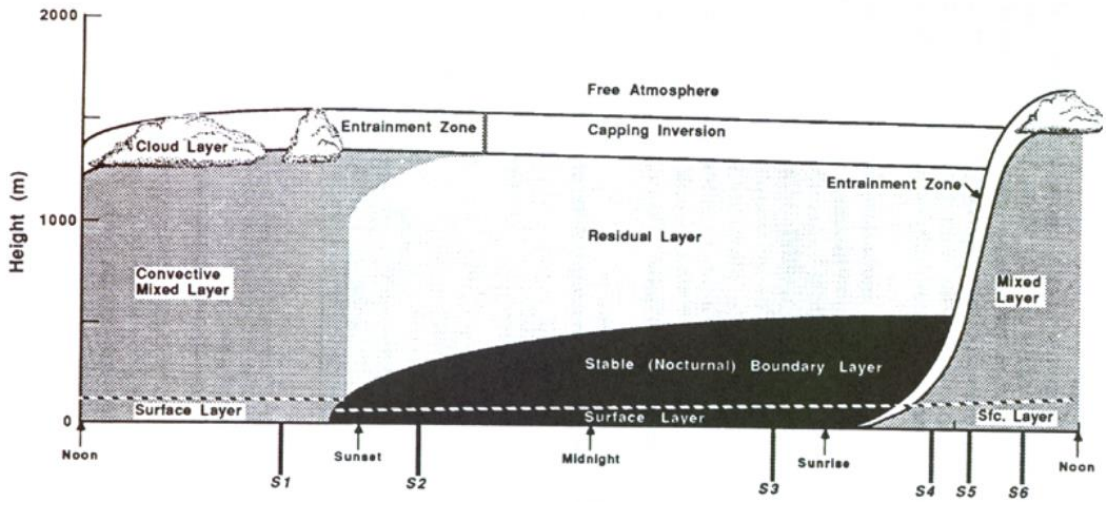

Fig. 7: Typical evolution of the atmospheric boundary layer as explained in Stull (1988)

3.4 Strategies to mitigate UHI formation

In general, urban areas have darker surfaces and less vegetation than their surroundings. Dark surfaces with low albedos and reduced vegetation, warm up the air over urban areas, which leads to the formation of the UHI. By using highly reflective building materials or coating (e.g. whitening of roofs) or by replacing impervious surfaces with natural vegetation, peak summertime temperatures can be significantly reduced. The urban heat island is reduced accordingly. Modifying the urban environment can have direct and indirect effects. Whereas direct effect alter the energy balance of the single building or area, and indirect effects are connected to city-wide changes in climate (Taha 1997a).

In this work, the effects of white roofs, urban greening and changed building density are discussed on the basis of their UHI mitigation potential.

3.4.1 Highly reflective roofs

The albedo describes the reflectivity for uniform and heterogeneous surfaces and is, at least in cities, a function of urban structures. Typically, urban albedos range from 0.1 to 0.2, but can be higher in certain cases due to the use of different materials. These low values are responsible for heat accumulation and the excessive warming of impervious materials which directly contributes to a heating of the air (Akbari et al. 2001). Although for water bodies the albedo is very low, the high heat storage capacity and evaporative cooling prevents them from warming up on a daily timescale. Taha (1997) demonstrated, that white roofs with an albedo of 0.72 are able to reduce the skin temperature by up to 45 °C compared to black coatings (with an albedo of 0.08) in the afternoon of a clear sky summer day. He proves that the temperature reduction strongly depends on the surface albedo by showing that the surface temperature is only 5 °C warmer than ambient air when increasing the albedo to 0.61, whereas regular gravel with an albedo of 0.1 exceeds air temperature by up to 30 °C.

By reducing the temperature of the surface, the intensity of long wave radiation is reduced as well which leads to a decrease of local convective heat fluxes to the ambient air. In turn, this can have significant effects on energy consumption for cooling purposes (Taha 1997b). Taha (1997) demonstrated that increasing the albedo of building roofs by 0.30 can

reduce peak summertime temperatures for the urban area of Los Angeles by up to 2 °C, providing that all roofs would undergo normal repairs. Other studies showed even a decrease of localized afternoon air temperatures on summer days in mid-latitude warm climates by as much as 4 °C by changing the albedo from 0.25 to 0.40. During the DESIREX Campaign 2008, Salamanca and Martilli (2012) stated that a higher albedo leads to about a 5% reduction in energy consumption through air conditioning during summertime periods for the area of Madrid. A temperature decrease of this magnitude is able to reduce urban ozone concentrations by up to 20 % during hot summer days. Another side-effect coming along with the implementation of white roofs and coatings is a potential increase in its useful life, due to reduction of diurnal temperature fluctuations.

3.4.2 Urban greening

Another effective moderator of urban climates is evaporation from soil-vegetation systems. Particularly in warm and dry climates of the low- and mid-latitudes, the near surface air temperature can be reduced by urban greening or water bodies. The energy needed for evapotranspiration is taken from sensible heat and transferred to latent heat by photosynthetic respiration, thus removing the warming potential of the atmosphere, hence leading to cooling. Given the right conditions, evapotranspiration can create ‘pools’ that are 2-8°C cooler than their surroundings. In extreme conditions, the latent heat flux can even cause the sensible heat flux to decrease to negative values. This results in a negative Bowen ratio, which describes the ratio between sensible and latent heat fluxes. By this, the air above the vegetation and over the dry surroundings must provide sensible heat to the vegetated area which results in a net cooling. Besides the transformation of natural land into urban areas, impervious sealed surfaces alter their hydrological properties. Water is removed from the surface more quickly than in rural environments by runoff and consequently, less water remains available for evapotranspiration, thus affecting the urban surface energy balance. Lower urban evapotranspiration rates are a major cause of urban warming and can enhance the urban heat island formation (Taha 1997b). Many studies have reported widely successful application of planting and vegetation to mitigate the UHI and reduce energy consumption (Rizwan et al. 2008)

A vegetation canopy can have different effects. It can actively regulate air temperatures by evaporative cooling, and passively by providing shadow. Bowler et al. (2010) compared 26 studies assessing the effect of creating green areas in cities, retrieving an average difference in air temperature between a built-up urban area and a green park of 0.5-2.5 °C. Rosenfeld et al. (1998) registered a temperature reduction of combined coloured and vegetated roofs of about 3°C for the city of Los Angeles, whereas Tong et al. (2005) found a temperature decrease of 1.6 °C for only vegetated roofs (Rizwan et al. 2008). A negative side effect, which is discussed by the scientific community are biogenic emissions of volatile organic compounds such as isoprene and monoterpenes (BVOCs) by various tree species. This effect has the potential to worsen the air quality by promoting ozone production for instance. The emission intensity can be temperature dependent and thus be especially pronounced during hot weather periods (Owen et al. 2003a). Other side effects of urban greening can be an improvement of the quality of life, increased value of property, decreased run-off which is further leading to flood-prevention and the direct sequestration of carbon dioxide. According to Rosenfeld (1998) however this sequestration only accounts for one fourth of the emission reduction achieved by energy savings due to cool surfaces (Akbari et al. 2001).

3.4.3 Building geometry

The proportion of radiatively active surfaces is increased by the presence of buildings. Roof, wall and road surfaces interact with the incoming solar radiation by the process of absorption and reflexion. Accordingly, distinct energetic patterns develop within the street canyon and can differ due to canyon orientation, building structures and materials, as well as the proportion of vegetation present in the street canyon. Whereas urban trees can lead to shadowing effects, the orientation of the street canyon and building geometry can enhance the circulation of air when aligned in the direction of existing fresh air corridors. The overall canyon geometry has a direct impact on energy exchange processes in urban areas. It affects the net radiation and consequently the temperature patterns. By the regulation of long wave radiation losses at night, the canyon geometry prevents the surface from cooling, thus promoting the development of nocturnal urban heat islands (Loridan and Grimmond 2012; Oke 1981b).

A parameter commonly used to describe the properties of an urban canyon and the prevailing energy exchange processes is the Sky View Factor SVF (ψ_s), which is a dimensionless measure of the sky, visible from inside the canyon. It is expressed in values between 0 and 1, quantifying to what extent the sky is obscured or exposed (Chapman and Thornes 2004).

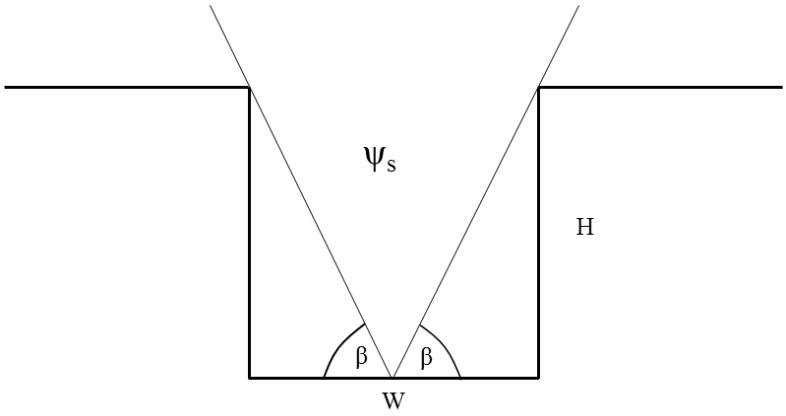

Fig. 8: Sky view factor in a symmetrical street canyon described by its width (W) and its height (H), $\psi_S = \cos \beta$ (Oke 1982b)

Other studies describe ψ_S as the ratio between radiation received by a planar surface and that from the entire hemispheric radiating environment (Watson and Johnson 1987). The exact determination of the SVF is difficult, but can be measured locally from photos made with fish-eye lenses from which the proportion of visible sky within a 360° view is inferred. Mathematical descriptions of ψ_S as well as the effect of building geometry on urban heat island formation are given in Oke (1981a). He uses equations based on the geometry of the site to calculate the SVF, specifically the ratio between height (*H*) and width (*W=2D*) of the canyon.

As the ratio of building height (*H*) to road width (*W*) increases, a considerable proportion of visible and 'cold' sky is replaced by relatively warm building surfaces absorbing the bulk of the radiation. Considering a point in the middle of the canyon floor with symmetric cross-section and infinite length, the sky view factor for the given point at the surface can be expressed as

$$\psi_s = (1 - 2\,\psi_w), \tag{3.4}$$

Where ψ_w describes the wall view factor, represented by each canyon side and is calculated as

$$\psi_w = 0.5\,(\sin^2\theta + \cos\theta - 1)(\cos\theta) - 1, \quad (3.5)$$

with Θ explaining the solar incidence angle. Additional contributions to the net long wave radiation for a point on the floor in the canyon are emerging from two components; one from the sky and the other from the walls. With assuming the radiant flux being isotropic, the modified net long-wave radiation L* is given by:

$$L^* = \psi_s(\sigma T_s^4) + 2\psi_w(\sigma T_{wall}^4) - \sigma T_{total}^4 \quad , \quad (3.6)$$

where T_w and T_s are describing the absolute surface temperatures of walls and floor and an almost linear relationship exists between L^* and the sky view factor at the ground ψ_s (Oke 1981a). According to the experiments from Oke (1981a) any SVF can be obtained for a defined H/W ratio, using the following equation:

$$SVF = -0.291\ln(x) + 0.4815 \quad (3.7)$$

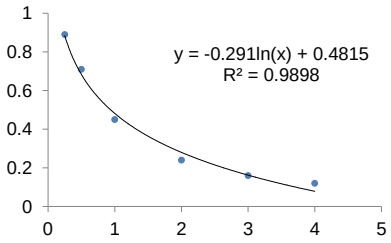

H/W	Rural	0.25	0.5	1	2	3	4
Ψ_s	1	0.89	0.71	0.45	0.24	0.16	0.12

Under the conditions mentioned above, the rural/urban cooling rates are mostly radiatively-driven and since radiative exchange is strongly dependent upon the sky view factor, the urban heat island can also be related to the measure of geometry. Analyzing the relationship between maximum heat island intensity observed in 31 settlements all over the world and the canyon sky view factor in central areas (ψ_s.), Oke (1981a) found a simple equation:

$$\Delta T_{u-r(\max)} = 7.45 + 3.97\ln(\frac{H}{W}). \quad (3.8)$$

This formula may not be universal, but satisfactorily describes the relationship between the urban heat island and building geometry (Grimmond et al. 2001;Oke 1981a). Simulations show that the sky view factor alone can significantly promote local urban heat island formation (Svensson 2004). On the one hand, a small SVF can enable shadowing of the street canyon resulting in a net cooling effect, on the other hand, air mixing intensities can be decreased and thus heat and pollutants can be trapped.

3.4.4 Anthropogenic heating

Anthropogenic heat, Q_f – waste heat released from human activities – is an important contributor to the energy balance of an urban area. The additional input of energy to the system negatively affects the thermal environment and the ambient air quality and potentially aggravates urban heat island formation. Heat in cities is released mainly from three sectors: the building sector, transportation sector and human metabolism. The building sector can be further sub-divided into electrical energy consumption and heating fuels such as natural gas and oil (Fan and Sailor 2005). The highest values of Q_f are basically found in urban centres located in cold climates during winter time where an additional heating load can account for 70 to 210 W/m² on average. For summer periods, values range from 20 to 40 W/m², respectively. According to Grimmond (1992), 10 % of the wintertime energy input (Q^*+G_f) in the city of Vancouver comes from anthropogenic heat, whereas Ichinose (1999) observed daytime summer Q_f values in central Tokyo of a maximum of 908 W/m² and 1590 W/m² in early morning hours in winter. Fan and Sailor (2005) simulated winter Q_f contributions of about 2 - 3 °C in the night time UHI of Philadelphia. Model simulations of Chen (2009) indicate that the heat released by human activities contributes almost 45 % to the summer UHI intensity (UHII) in Hangzhou City and 54 % in winter respectively. Oke (1997) showed that weekday power consumptions in Los Angeles is to rise by about 33 % when temperatures increase from 20°C to 25 °C. The magnitude of Q_f depends on the weather situation, population density, climate background and per capita energy use (Quah and Roth 2012). This additional human induced contribution to the urban energy balance is considered to have side effects on different processes in the urban climate. Next to the additional heat production itself, it modifies the urban heat island and thus urban rural circulation patterns. Another side effect of anthropogenic heating which is often considered as more precarious than elevated temperatures is the emission of greenhouse gases by combustion processes, which in turn supports the global temperature increase as projected by the IPCC.

4. Urban air quality

For cities acting as sources of emissions, urban air pollution can have widespread effects on human health, regional visibility and ecosystem degradation. On a broader scale, it can promote regional climate change and global pollutant transport. The impacts on human health can be manifold, ranging from current respiratory problems to severe cardiovascular deceases (Molina & Molina 2004). According to the latest report on air quality in Europe, the European Environmental Agency (EEA) stated that about 90 % of urban residents in the EU are exposed to hazardous pollutants classified as harmful by the World Health Organization (WHO). For the period 2001 to 2011, the EEA calculated the percentage of urban population exposed to air pollutants exceeding the limits defined by the EU (Guerreiro et al. 2013; WHO 2006):

Tab. 1: Percentage of urban population exposed to air pollutants from 2001-2011 (Guerreiro, de Leeuw, & Foltescu 2013)

Pollutant	EU - Limit	Fraction exposed [%]
Pariculate Matter (PM10)	50 µg/m³ daily mean not to be exceeded on more than 35 days/year	20-44
Nitrogen Dioxide (NO2)	40 µg/m³ annual mean	5-23
Ozone (O3)	120 µg/m³ daily maximum 8-hourly average not to be exceeded on more than 25 times/year	14-65
	year 2003 alone	65
Sulphur Dioxide (SO2)	125 µg/m³ daily mean not to be exceeded more than 3 days/year	1

Next to the pollutants, listed in Tab. 1, carbon monoxide CO and nitric oxide NO can be counted to the 6 most common pollutants when discussing urban air quality.

Sulphur dioxide is the classical pollutant associated with the burning of fossil fuels. However, in industrialized countries, concentrations have been significantly reduced. Acid rain is a negative by-product of SO_2 pollution which can also affect ecosystems downwind of the city. Because it is not seen as a relevant pollutant within the modelling area it is not further discussed in this context. Nitric oxides are generated via oxidation of atmospheric nitrogen during combustion processes, whereas the 'real' secondary pollutant NO_2 is formed by oxidation of the non-toxic nitric oxide NO of which the main part comes from car exhaust. A small amount of NO_2 can also be emitted directly. NO_2 is strongly connected to O_3 formation via photochemical reactions. High levels of tropospheric ozone concentrations can impact human health, especially in periods with extraordinarily high air temperatures. CO originates from incomplete combustion in vehicles. In high

concentrations, it is a dangerous respiration poison and can form climate sensitive CO_2 via reaction with H_2O.

Particulate matter is grouped in the three so-called modes, which are defined as ultrafine, fine and coarse. Ultrafine particles have aerodynamic diameters of less than 1 µm are chemically formed or condensed from hot vapour and can coagulate to larger particles ($PM_{2.5}$). Both are supposed to have a large impact on human health because they can deposit in the human respiratory system causing severe illnesses. The coarse fraction PM_{10} may have natural origins, e.g. sea spray, desert or soil dust, but in combination with the other fractions, the total suspended matter (TSP) can significantly cause air quality problems, also in the context of visibility impairment (Fenger 1999; Molina & Molina 2004). Lead and other heavy metals are industrial sources which are, at least in industrialized countries, regulated by air quality standards. Volatile organic compounds (VOC) should also be taken into consideration as being hazardous pollutants and can also act as precursors for the formation of secondary pollutants (e.g., O_3). They stem from incomplete combustion of fuels in cars or during industrial processes. Benzene and the series of polyaromatic hydrocarbons (PAH) are other important compounds in urban air. Biogenic emissions of VOCs (BVOCs) from natural sources have recently been investigated extensively based on the negative effect of urban greening on air quality due to photochemical air pollution (Fenger 1999).

Next to local emissions, meteorological conditions play a crucial role in urban air quality, especially considering wind speed and wind direction, which are responsible for pollutant dispersion and transport. Urban heat islands promote distinct thermal differences between urban and rural areas which amplify urban-rural circulation patterns. During periods with stable atmospheric conditions and weak winds, strong inversion layers can develop above a city which force the pollutants to remain in the urban atmosphere over a longer period of time (Fenger 1999). On a regional scale, aerosols can have a cooling effect and are able to significantly influence precipitation patterns and cloud formation. The long-range transport of sand dust or smoke originating from beyond urban centres can give rise to episodic pollution events and can, for instance, significantly affect dust levels in cities (Molina & Molina 2004). Acid rain can occur downwind of the city when sulphate compounds accumulate through wet deposition.

In the following Chapters, five relevant urban air pollutants are described based on their chemical formation. The temperature dependence of chemical reaction rates is explained using the example of photochemical ozone production (Chapter 4.4).

4.1 Photochemical formation of tropospheric ozone (O_3) and the NOx-family

About 50 % of the tropospheric ozone concentration is originated from the stratosphere and transported to lower layers by vertical and horizontal mixing and advection. The second half however results from chemical reactions. In highly polluted urban areas, this part is supposed to be even higher. The following reaction chain (4.1) describes the photolysis of ozone to form molecular and atomic oxygen at a wavelength around 300 nm. The most important aspect of this photochemical reaction is the production of single oxygen O(^{1}D), since it has the potential to react with water vapour to form the highly reactive hydroxyl radical OH. This reaction happens very fast (Finlayson-Pitts & Pitts Jr 1999).

$$O_3 + hv\ (\lambda < 310\ nm) \rightarrow O_2 + O(1D)$$
$$O(1D) + H_2O \rightarrow 2\ OH \qquad (4.1)$$

The hydroxyl-radical OH itself triggers a large number of chemical reactions (Roedel 1992). Predominantly dependent on the quantum energy of solar radiation in the ultra violet spectrum, both reactions are independent from temperature (Seinfeld and Pandis 2012).

A substantial aspect of tropospheric chemistry is the dependence of ozone production on the NO_x (NO_2 + NO) abundance. In the process of Ozone generation, NO_x cycles back and forth between NO and NO_2. Therefore, it can be seen as a catalyst in O_3 formation, making it responsible for the ozone production efficiency (Seinfeld & Pandis 2012). Ozone or triatomic oxygen is a powerful oxidizing agent which reacts with some gases such as nitric oxide or NO or with surfaces (particles, plants) via deposition processes. As a secondary pollutant, O_3 needs a number of primary pollutants acting as precursors. Whereas stratospheric ozone is important for reducing ultraviolet light entering the earth's atmosphere, tropospheric ozone generates several negative effects for human health such as aggravation of asthma or decreased lung function. Next to human health, ozone can

harm sensitive vegetation, including trees and plants, and is especially pronounced during the growing season (EPA 2012; Seinfeld & Pandis 2012).

NO_2 is a reactive gas in the air which is formed by the oxidation of nitric oxide (NO) which itself is emitted mainly by traffic (47% in Europe) and industrial combustion processes, agricultural fertilizers, aircrafts or lightning. To a small amount, it can also be emitted directly.

Like ozone, NO_2 primarily affects the respiratory system and can have long and short term effects on human health. Being highly reactive, nitrogen dioxide can also have adverse effects on ecosystems. Extensive deposition can lead to acidification and a surplus of nutrient nitrogen in soils and aquatic systems. In the case of a nutrient oversupply, eutrophication can lead to changes in animal and plant communities and biodiversity loss (Guerreiro, de Leeuw, & Foltescu 2013).

First observed in Los Angeles 1940, it was found that ozone mainly originates from reactions between substances emitted from vehicles, industrial plants and vegetation. In the presence of sunlight, these reactions involve volatile organic compounds and different oxides of nitrogen (NO_x). As a photochemical pollutant, ozone is basically formed during daytime hours and destroyed during the night within complex chemical reaction chains. Significantly following a diurnal cycle, ozone concentrations are highest during periods with hot, sunny and calm conditions. The resulting photochemical smog negatively affects the air quality in urban areas (Seinfeld & Pandis 2012).

In European cities, the dominant reaction during the night is the reduction of ozone by nitric oxide (NO) resulting from car exhaust to form oxygen and nitric dioxide (NO2). Therefore, ozone levels are higher at roof level than in the street canyons and can even be higher in the rural surrounding due to urban plumes being transported according to prevailing winds or due to UHI induced urban rural circulation patterns. The concentration of NO_2 however is largely determined by the available amount of O_3 (Fenger 1999). The sum of NO_2 and O_3, expressed by the variable O_x is often used to describe the oxidation potential of the atmosphere.

The formation and removal of ozone in the troposphere mainly results from the combination of atomic oxygen and molecular oxygen in the presence of a third energy absorbing agent (M), which can be nitrogen or oxygen molecules, but also particles,

surfaces or trace gas molecules (4.1). Oxygen atoms are mainly provided through photo dissociation of NO_2 (4.3), whereas the threshold wavelength for production of ground-state NO and O atoms is 397.8 nm (Finlayson-Pitts & Pitts Jr 1999). Due to titration reactions with the freshly emitted NO in the evening, ozone is depleted and transferred back to NO_2 (4.4) which then closes the nitrogen cycle. With regard to equation 4.2 – 4.4 alone, no net production of ozone is to be observed, the reaction is in the state of equilibrium (Guerreiro et al. 2013).

$$O + O_2 + M \rightarrow O_3 + M \quad (4.2)$$

$$NO_2 + h\nu\ (\lambda < 400\ \text{nm}) \rightarrow NO + O \quad (4.3)$$

$$O_3 + NO \rightarrow NO_2 + O_2. \quad (4.4)$$

Comparing the reaction rate coefficients, the ozone destruction according to equation 4.10 happens comparably faster than the production of ozone in 4.3. For the net production of ozone the presence of nitrogen oxides alone are not enough and a third agent M is needed as it is explained in the following.

The slower photolysis reaction (eq. 4.3) is the rate limiting factor for the nitrogen cycle and the main reason why ozone is formed only during the day and concentrations are high in the summer months with intense radiation. Being dependent on the amount of free oxygen atoms, the formation of ozone via reaction 4.2 is mostly driven by the intensity of solar radiation. The overall cycle time is only a few minutes, whereas the accumulation time of ozone can be several hours depending on the weather situation and emission rates (Finlayson-Pitts & Pitts Jr 1999; Seinfeld & Pandis 2012). At the same time, the rate of the cycling reactions is fast enough to maintain a photo stationary state of ozone controlled by the ratio of NO_2/NO. At equilibrium in ambient air and constant pollution concentrations, a NO_2/NO ratio of 10:1 would be needed to generate 0.01 ppm of ozone. However, in reality this ratio is 1:10 which leads to the assumption that the nitrogen cycle itself cannot be responsible for the high ozone concentrations in urban areas and their vicinity. In order to accumulate according to the photo stationary state, an additional agent has to be present for converting NO to NO_2 without the destruction of ozone. This additional pathway is provided by the photochemical oxidation of VOCs such as aldehydes or hydrocarbons which can be of anthropogenic or biogenic origin (BVOC). Without C-H bonds being

present in the atmosphere, there would be no net production of ozone (Seinfeld and Pandis 2012; Roedel 1992).

Carbon monoxides (CO), carbon dioxides (CO_2) and water are derivatives of VOC oxidation processes in the atmosphere. Intermediate steps of this overall oxidation are driven by hydroxyl radicals (OH) who are formed by photolysis of ozone in the presence of water vapour, nitrous acid (HNO_3) or other sources.

Formaldehyde (HCHO) is used in the following for illustrating the processes of ozone formation and removal. It is basically produced from incomplete industrial combustion processes, forest fires, automobile exhaust, and tobacco smoke. Further, it is a by-product of oxidation of methane. When produced in the atmosphere under the presence of sunlight, it can become a significant constituent of smog in urban areas. HCHO is the simplest VOC containing a carbonyl (C=O) bond (Seinfeld & Pandis 2012).

The oxidation cycle for formaldehyde can be written as follows:

$$OH + HCHO \rightarrow H_2O + HCO \quad (4.5a)$$

$$HCHO + h\nu\ (\lambda < 400\ \text{nm}) \rightarrow H + HCO \quad (4.5b)$$

$$HCO + O_2 \rightarrow HO_2 + CO, \quad (4.6)$$

$$HO_2 + NO \rightarrow NO_2 + OH \quad (4.7)$$

When reacting with a free hydroxyl radical, HCHO is cracked to water and a formyl radical (HCO) which in turn can be an important precursor of smog formation (4.5a). HCO then reacts with oxygen in the air and forms highly reactive hydroperoxyl radicals. This radical can also be formed by photolysis of HCHO (4.5b). Another derivative is carbon monoxide (4.6). To close the reaction cycle, OH returns again in equation 4.7 in addition to the production of NO_2 required for ozone formation (Finlayson-Pitts & Pitts Jr 1999; Seinfeld & Pandis 2012).

The formation of nitric acid (HNO_3) is another reaction important for the understanding of ozone formation, because it provides an explanation for the removal of NO_2 by a radical sink reaction:

$$NO_2 + OH + M \rightarrow HNO_3 + M. \quad (4.8)$$

These equations explain the basis of photochemical reactions, where ozone formation mainly can be attributed to the impact of intense ultraviolet radiation and the presence of precursor substances. The direct dependence of temperature on ozone formation is explained in Chapter 4.4

The equations above display the simplest of many complex reaction cycles. Typical patterns of diurnal ozone concentrations found in urban atmospheres can be explained well with the following simplified image:

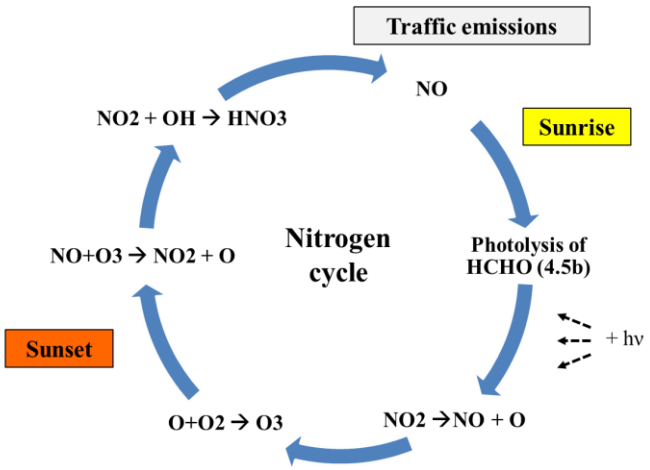

Fig. 9: Diurnal nitrogen cycle producing and removing ozone in urban areas (Summary of eq. 4.2 - 4.8)

Strongly corresponding to the diurnal cycle, the chemistry of the NO_x family differs significantly between night and day time. In the early morning, NO is produced by traffic emissions and remains in the urban atmosphere because free radicals for conversion of NO to NO_2 are not yet present in the ambient air. At sunrise, the photolysis of formaldehyde starts. At the end of this reaction stands the conversion of NO to NO_2 by the peroxy radical (4.7). When the ratio of NO_2/NO is large enough by the end of the afternoon, ozone builds up. With sunset, NO which is emitted by evening traffic removes O_3 by forming NO_2, which again is dissolved via the radical sink reaction during the night generating nitric acid. Increased traffic volume in the morning builds up NO again.

NO_x can further react with ammonia, moisture, and other compounds to form small particles. Through nitrogen formation, they also contribute a great extent to PM_{10} and $PM_{2.5}$ concentrations and the formation of secondary inorganic aerosols (SIA).

Ozone as well as NO_x can be dispersed and diluted by winds and a rising of the inversion layer in the course of a day can especially decrease concentrations by vertical mixing.

Increased mixing almost always dilutes NO_x, whereas considering ozone there is no general rule. The concentration of O_3 depends upon whether higher concentrations are present aloft, trapped above the inversion layer during the night and whether they are available again to increase ozone on the following day (Seinfeld & Pandis 2012).

Urban heat islands are responsible for specific urban-rural circulation patterns and with ozone formation happening relatively slowly, levels can be significantly elevated downstream from the city due to transport within an urban plume. Ozone is a secondary pollutant which means that efforts to reduce concentrations can only be achieved by controlling primary pollutants.

Averaged European ozone levels have increased from 20 μgm^{-3} around 1900 to about double the amount today which is mainly due to the rise of precursor emissions. Summer smog with temporary ozone concentrations of up to 400 μgm^{-3} can occur in many European cities. In particular, in Athens and Barcelona, but also in Frankfurt, Milan, Prague or Stuttgart, photochemical pollution is a known problem (Fenger 1999). The reduction in carbon stored in vegetation due to ozone pollution is assumed to account for 6.2% globally and 4 % in Europe. In general, there is an obvious gradient from low concentrations in the north to elevated values in the south of the continent (Guerreiro, de Leeuw, & Foltescu 2013).

4.2 Carbon Monoxide (CO)

Carbon monoxide (CO) is a colourless, odourless gas emitted from incomplete combustion processes. The highest concentrations can be found in urban centres with high traffic loads. According to estimates, two-thirds of the global tropospheric CO comes from anthropogenic sources, for instance, the oxidation of Methane (CH_4). The most important sink for CO is the reaction with OH radicals. The common lifetime ranges from 20-90 days. In the presence of carbon monoxide, OH and HO_2 cycle between themselves. This leads to a constant steady state partitioning by which CO oxidation is closely linked to the NO_x-cycle (Fig. 10).

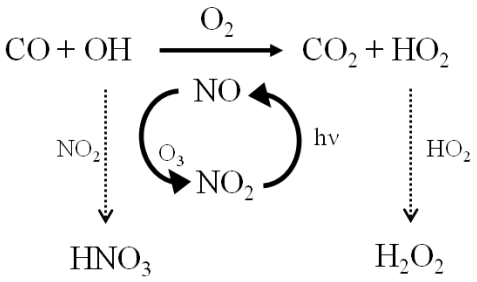

Fig. 10: Reactions involving the HO_x family in CO oxidation

CO has the potential to reduce oxygen delivery to the body's organs (like the heart and brain) and tissues which can result in adverse effects for human health (EPA 2012). As a by-product, CO can also be formed in the course of the oxidation of VOCs (eq. 4.5a). It can contribute to the natural background O_3 concentration by oxidation processes. Air quality limits set by the EU amount to 10 mgm^{-3} with regard to the 8-hour mean (Guerreiro, de Leeuw, & Foltescu 2013). The long lifetime of CO in general leads to elevated ambient background concentrations.

4.3 Aerosols

The term aerosols is used to describe a mixture of solid or liquid particles which are suspended in the air. They are grouped in size depending classes (modes) which can be divided into coarse, fine and ultrafine fractions. Ultrafine particles with sizes (aerodynamic diameters) smaller than 1 µm are formed by chemical reactions or condensed from hot vapour, for example, from diesel exhaust and coagulate into fine particles (≤ 2.5 µm). Fine and ultrafine particles are mainly of anthropogenic origin, coarse particles with sizes less or equal to 10 µm predominantly come from natural sources like dust, sea spray or pollen (Fenger 1999). In the presence of supersaturated water vapour (relative humidity of 100% or higher), particles can act as cloud condensation nuclei, essential for cloud formation and precipitation (Seinfeld & Pandis 2012).

A further classification of particles is based on their genesis. Primary particles are emitted directly into the atmosphere from traffic exhaust or chimneys, whereas secondary particulate matter is formed by oxidation or transformation of primary gaseous emissions. These gaseous emissions are commonly defined as precursor gases like SO_2, NO_x, NH_3 and VOCs. The first three react in the atmosphere to form ammonium, sulphate and nitrate

compounds which can later condense into liquid form, generating new particles in the air. These newly formed particles are called secondary inorganic aerosols (SIAs). Additionally, secondary organic aerosols (SOA) can be formed when certain VOCs are oxidized. The formation of SIA and SOA depends on a number of chemical and physical factors. Meteorological conditions like solar radiation, cloud cover or humidity also control PM concentrations. The number and mass of particles in the ambient air depends on the source of the emission (Fig. 11).

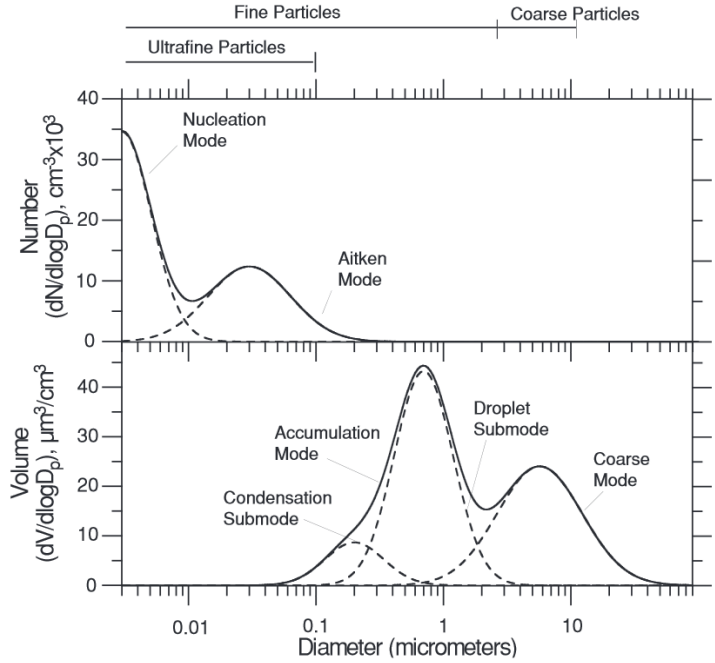

Fig. 11: Mass and number distribution of urban particles with their typical source contribution (Seinfeld & Pandis 2012)

As indicated in Fig. 11, the number of small particles can be very large, although their total mass is not significant, especially for aerosols smaller than 2.5 μm. This fact is important for the transport and accumulation in the human respiratory system (Fenger 2009).

The atmospheric aerosol distribution is usually characterized by different modes (Fig. 11). Considering the volume or mass distribution of atmospheric aerosols, two modes are usually distinguished. The accumulation mode covers particles ranging from 0.1 to 2 μm which predominately result from primary emissions, condensation, and the long range transport of secondary particles or coagulation of smaller compounds. The coarse mode describes particles with aerodynamic diameters larger than 2 μm which mainly are produced by mechanical processes such as wind or erosion (human and natural made dust,

sea salt, pollen, etc.) and enter the system as primary particles, except some secondary sulphates and nitrates.

The condensation sub-mode is based on particle growth by coagulation and water vapour condensation or simply by particle emission. The droplet sub-mode is generated when particles from the accumulation-mode participate in cloud formation. Aerosols with sizes exceeding 0.1 μm are negligible in number compared with smaller sized particles. Usually two modes are dominating the number distributions: The nucleation-mode particles (smaller than 20 nm) can be disregarded in size while the Aitken nuclei (10-100 nm) form the accumulation mode in the mass distribution.

In urban areas, the aerosol size distribution is quite variable and there is an order of magnitude more particles close to major roads compared with the average urban concentration. The chemical composition of fine and coarse urban particles strongly depends on atmospheric and chemical conditions. The main mechanism for transferring particles from the Aitken to the accumulation mode is by coagulation and condensation of vapours onto existing particles. The presence of clouds can also modify the composition when chemical reactions in the aqueous phase result in water droplets. Total Suspended Particulate Matter (TSP) is often used to characterize the full aerosol mass in the ambient urban air, including all particles smaller than 50 μm (Seinfeld & Pandis 2012).

The major threat to human health mainly results from inhalation and penetration into lungs and blood streams, causing adverse effects to respiratory, cardiovascular, immune and neural systems. Here, the ultrafine particles are assumed to be the most hazardous compounds. In Europe, mortality effects are clearly associated with particles smaller than 2.5 μm (Guerreiro et al. 2013).

4.4 Temperature dependence of chemical reactions

A number of factors influence the nature of chemical reactions, with amongst others (nature of reaction, concentration, pressure and reaction order) the thermal conditions play a crucial role in chemical composition of the urban air, having the potential to accelerate or slow down chemical reactions (Finlayson-Pitts et al. 1999).

The temperature dependence can be expressed by the reaction rate or speed of reaction, explaining how fast or slow a chemical reaction takes place. According to the basic principles of chemical kinetics, the rate equation relates the concentrations of two or more compounds to a reaction rate coefficient *k*, which is strongly dependent on the temperature (Finlayson-Pitts et al. 1999).

Following equation is valid for any second-order reaction:

$$k(A + B) \rightarrow AB \tag{4.9}$$

With *A* and *B* being any chemical compound, the reaction rate coefficient *k* can be calculated by applying the exponential *Arrhenius Equation:*

$$k = Ae^{-\frac{Ea}{RT}} \quad [\text{cm}^{-3}\,\text{molecule}^{-1}\,\text{s}^{-1}] \tag{4.10}$$

The parameter *A* describes an empirical pre-exponential parameter which is derived from experiments for different known reactions (Seinfeld and Pandis 2012). Often expressed as frequency factor, it has the unit of s^{-1}, and depends on the number of collisions of molecules. E_a is the activation energy needed to start a chemical reaction. It is given in units of kJ mol^{-1}. R is the general gas constant (R=8.3145 J $mol^{-1}K^{-1}$) and T the temperature given in Kelvin (Finlayson-Pitts & Pitts Jr 1999). Characteristic rates of constants of atmospheric chemical reactions are given in Seinfeld and Pandis (2012) appendix B, page 1182 or Sander et al. (2006) Table 1-1 and 2-1 and Crutzen et al. (1974).

Basically, equation (4.10) describes the relationship between the activation energy and the rate at which a reaction proceeds in dependence of the system's temperature. In more simple words, *k* explains the number of collisions resulting in a reaction per second, *A* would be the total number of collisions and the term $e^{-\frac{Ea}{RT}}$ can be described as the probability that a collision will lead to a reaction. From equation (4.10) it can be inferred, that an increase in temperature will lead to an increase in the rate of reaction (Seinfeld & Pandis 2012). In urban areas, the additional energy for chemical reactions can be partly attributed to elevated temperatures due to absorbed heat.

Several studies have stated, that the emission of these precursor substances strongly depends on the temperature, which indirectly also lead to an increase of secondary

pollutants as for example ozone (e.g. Harley et al. 1996; Monson et al. 1992; Sharkey & Yeh 2001).

By applying a simple box model (supplied by Renate Forkel by personal communication), ozone concentration can be calculated for different temperatures using reaction rate coefficients as explained in Stockwell et al. (1997). The box model relies on the "Regional Atmospheric Chemistry Mechanism – RACM" (Stockwell et al. 1997) which is based upon the earlier "Regional Acid Deposition Module Version 2 - RADM2" (Stockwell et al. 1990). The latter is used for the WRF-Chem simulations presented in Chapters 6.3, 7.2 and 7.3.2. Fig. 12a illustrates daily peaks of ozone concentrations for constant temperatures varying between 293 and 308 K (20-35 °C) using a constant pressure of 1013.25 hPa and a relative humidity of 50 %. Reference latitude is 48 ° N, solar angle refers to summer time. Initial concentrations of chemical compounds are given in Tab. 2.

Tab. 2: Initial concentrations as used within the box model

Compound	CO2	O3	NO	NO2	CO	CH4	ISO	HCHO	SO2
C [ppm]	390	0.01	0	0.05	0.2	1.7	0.003	0.002	0

Fig. 12b shows the temperature dependent increase of Formaldehyde (HCHO) which itself is known for being a precursor to ozone formation. The relationship between ozone and isoprene can be documented when increasing isoprene emission stepwise in the box model (Fig. 12c). As isoprene emissions increase with increasing temperature (Kesselmeier et al. 1999), this relationship depends on the temperature. Another aspect which controls the formation of ozone is the relative humidity. This can be analysed by relative humidity for a constant temperature of 300 K (Fig. 12d).

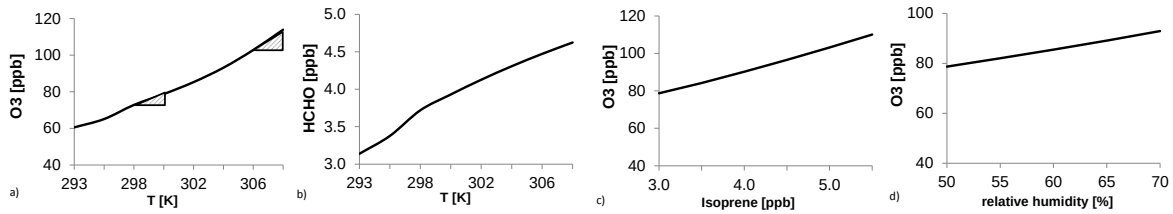

Fig. 12: Results from the box model according to the effect of increasing temperature on ozone (a) and HCHO (b) as well as the effect of rising isoprene levels (c) and relative humidity on ozone concentration (d).

Fig 12a indicates that the effect of temperature on ozone concentration is more intense in higher temperature regions. Increasing the temperature by 2 K, results in an increase of ozone by 6 ppb in the range of 298 to 300 K and by 11 ppb when increasing T from 306 to 308 K (grey triangles). Although the box model accounts for a simplification of a broad

range of complex processes, it is well suitable to illustrate the effect of changing temperature on the chemical composition of the urban air, using the example of ozone formation (Fig. 12).

Explaining the dependence of temperature on ambient concentrations found for a selected chemical compound however is not trivial. A change in temperature promotes a change in atmospheric dynamics, which in turn leads to a modification of the atmospheric state. Warm air is characterized by increased potential for turbulent mixing, whereas cold air can produce stable layers with weak air mixing intensities. Furthermore, many chemical reactions are primarily dependent on the amount of incoming solar radiation or the presence of a precursor substance which can be BVOC's (e.g. isoprene) for instance.

5. The model test bed

In this work, the urban area of Stuttgart serves as a test bed for calibrating the urban canopy model and explaining and modelling distinct features of the urban climate and the effect of modified land surface properties on urban heat island formation. Stuttgart, located in the south-western part of Germany, is the capital of the federal state of Baden-Württemberg. With around 600,000 inhabitants, it is the centre of a metropolitan region of about 2.7 million people. The city is located in a valley with a difference of elevation between the city centre and surrounding hills of about 150-200 m. The climate of Stuttgart is characterized by a large number of days of sunshine and mild weather with weak winds generally from the south-west. At such a low elevation in the Neckar basin, the greater Stuttgart region is one of the warmest areas of Germany. Observations at the inner-city meteorological station Stuttgart-Schwabenzentrum show an annual mean air temperature of 10 °C, a mean wind speed of 2 ms^{-1} and an average annual precipitation of 573 mm (Amt für Umweltschutz Stuttgart 2013). The weak mountain-valley circulation leads to an increasing potential for natural heat trapping in the urban region. This is especially true during heat waves and stable weather conditions. According to modelling work of the Department for Urban Climate (Office for Environmental Protection Stuttgart), the area of the city having more than 30 days/year heat stress is anticipated to increase from 6% in 1971-2000 to 57% in 2071-2100 using the SRES A1B IPCC Emission Scenario (Amt für Umweltschutz Stuttgart 2013). According to the German meteorological service (DWD),

heat stress is defined as feeling of thermal discomfort when the human body is no longer able to regulate its physical heat balance. This effect in particular occurs in periods with elevated temperature, little cloud cover, high humidity and weak winds. The way these conditions impact the human comfort however depends on individual perception, which makes it difficult to find a general definition for this term (DWD 2014). Due to enormous traffic loads during peak hours, especially during periods of aggravated heat stress or weak natural circulation processes, local inhabitants can suffer from air pollution and high concentrations of NOx, O3, CO and particulate matter.

These conditions in particular promote the urban heat island formation in that area. Surface temperature retrieved from satellite data shows distinct patterns for high density residential and commercial areas in the north of the city and can be contrasted with low density residential areas with larger amounts of vegetation in the south. A plot of 2m air temperature for an urban and a rural site illustrates the UHI which is particularly pronounced in the night time hours.

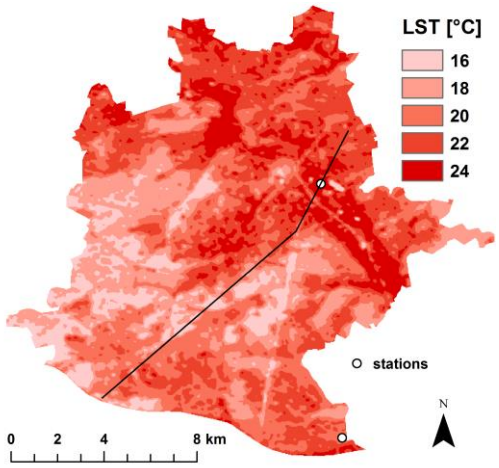

Fig. 13: Land surface temperatures (LST) retrieved from LANDSAT7 radiative temperatures for September 19th 2005 10 am showing distinct temperature patterns throughout the urban area of Stuttgart.

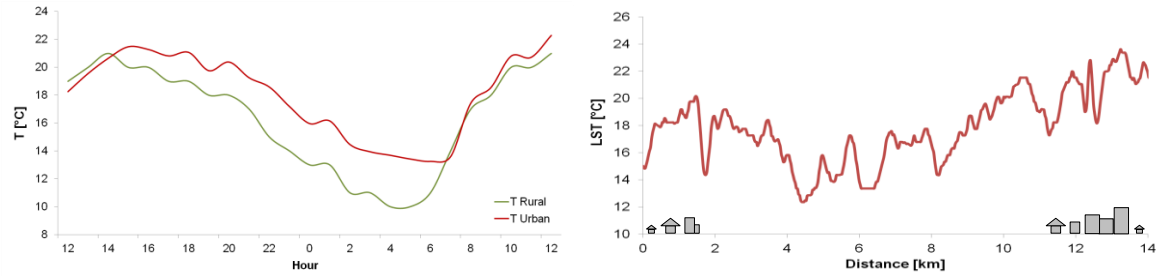

Fig. 14: 2m air temperature for September 19th 2005 10 am for an urban (Stuttgart Schwabenzentrum) and a rural (Echterdingen) measurement station (left), and LST for the transect from Fig. 13

The plots in Fig. 14 show an average temperature difference of 1.3 °C, with maxima reaching about 4 °C in the night time and early morning hours. Prevailing averaged wind speeds of around 1 - 2.5 ms^{-1} are very low while mainly coming from the south-western direction.

6. The WRF model

The major intent of this work is to predict the effect of urban heat island mitigation strategies on dynamical and chemical processes and interactions in the urban environment. Mesoscale meteorological models are adequate tools to investigate the development of local urban climates under changing boundary conditions. Boundary conditions in this case include different urban planning strategies like urban greening, highly reflective roofs and façades or altered building fabrics and canyon geometries. These scenarios of urban development can significantly affect the dynamical state of the urban canopy and boundary layers and modify atmospheric circulation patterns. In general, the mesoscale model solves the conservation equations of mass, momentum, energy and air humidity. In order to represent subscale processes within urban areas, adequate parameterization efforts have to be carried out (Martilli et al. 2002).

The NCAR Weather Research and Forecasting Model WRF (Skamarock et al. 2005) is used which includes an urban canopy model (Chen et al. 2011b) to account for the heterogenic nature of urban environments. In general, WRF is a non-hydrostatic mesoscale numerical weather prediction (NWP) system designed for both research and operational applications, able to treat either real data (observations, analysis) or idealized atmospheric conditions. To describe the evolution of the state of the atmosphere, Reynolds Averaged Navier- Stokes equations (RANS) are solved on a horizontal and vertical grid, whereas the hydrostatic-pressure vertical coordinate is terrain-following (Skamarock et al. 2005). The Navier-Stokes equations represent the conservation of mass by determining three-dimensional velocities and the conservation of energy by the first law of thermodynamics. Atmospheric motions are determined between the model variables due to external forcing like solar radiation and interactions with the earth surface including fluxes of heat, moisture and momentum. In WRF, different schemes are available to account for microphysics, cumulus parameterisation, surface and atmospheric radiation physics as well

as processes in the atmospheric boundary layer. Boundary conditions for driving the model physics are retrieved from global reanalysis data (observations, global models, etc.) and downscaling techniques allow for nesting of model domains down to resolutions of 1 km to transport information from large scale processes down to finer scales.

According to the prevailing land use, the community land-surface model NOAH-LSM provides skin temperature, surface sensible and latent heat fluxes as lower boundary conditions for the meteorological model on the basis of diurnal varying Penman potential evaporation approaches. In addition, a multi-layer soil model, a canopy resistance model, frozen ground physics and surface hydrology are included. Prognostic variables in NOAH provide soil moisture and temperature, water stored in the vegetation and snow water equivalent stored in the ground (Chen 2011). The thermal characteristics and radiative properties of different land use classes and soils are derived from parameter tables linked to the LSM.

When analysing urban systems and the evolution of local climate phenomena like urban heat islands, a careful selection of surface, radiation and boundary layer physics is necessary to maintain model stability. This aspect is achieved by coupling of an urban canopy model to the NOAH land surface scheme in WRF (Zehnder and Grossman-Clarke 2009).

To investigate the effects on air quality, the meteorological component has to be coupled to chemical mechanisms. For this purpose, a fully coupled “online” model (WRF-Chem) has been developed (Grell et al. 2005) which is consistent with all conservative transport done by the meteorological model. Chemical reactions are controlled by governing equations defining meteorological conditions and lower chemical boundary conditions are pre-defined by anthropogenic emission inventories. In the real atmosphere, chemical and physical processes are coupled, whereas chemistry can affect meteorology, for instance, through its effect on the radiation budget or the interaction of aerosols with cloud condensation nuclei (CCN). Accordingly, cloud formation and precipitation strongly affect chemical transformation processes while wind and turbulence influence chemical transport. In WRF-Chem, the aqueous phase chemistry is coupled to some of the microphysics schemes and to three choices of aerosol schemes. For calculating gas-phase chemical and photolysis reactions, different schemes are also available. Dry deposition, meaning the flux of trace gases and particles from the atmosphere to the surface, is calculated from

temporally and spatially varying deposition velocities with physical properties of the surface being retrieved from WRF soil/vegetation schemes. For further information on the basic theories and architecture of WRF-Chem, refer to Grell et al. (2005).

In urban environments, modified circulation patterns impact air chemistry in manifold ways, which requires the proper parameterisation of processes in the urban atmosphere. The most important effects on the airflow are:

- Turbulent wakes generated by roughness elements (buildings) promote mixing and diffusion of momentum, heat, moisture and scalars such as pollutants.
- The mean kinetic energy of the flow is converted into turbulent kinetic energy (TKE) due to the presence of a distinct shear layer at the top of the canopy.
- Pressure differences due to buildings (drag)
- Differences in diurnal heating and cooling cycles of surfaces due to solar radiation, radiation trapping in street canyons and heat storage in buildings.

In order to properly reproduce the chemical composition of the urban atmosphere, one has to be sure that relevant dynamical processes have been portrayed precisely.

For this reason, the modelling work is divided into two parts. The first part calibrates the model according to the selection of the appropriate urban canopy model in WRF in order to sufficiently illustrate the urban heat island of Stuttgart and to calculate the effect of mitigation strategies on dynamical properties. In the second part, WRF-Chem is applied using the setup from the meteorological approach to model the chemical composition of the urban air. Meteorological and air quality observations are used to evaluate modelling results. In order to properly set up the model, basic methods have to be understood and evaluated by executing sensitivity tests. First it is important to understand the basics of urban mesoscale modelling and the way it can be done by WRF.

6.1 Urban mesoscale modelling

The difficulty in modelling processes in the urban system lies in the complex nature and heterogeneity of urban surfaces. On the one hand side, a city is a combination of different surface types and geometrical structures with typical sizes ranging from one to several tens of metres. Each element inherits distinct dynamic and radiative properties which generate

turbulent or non-turbulent atmospheric structures at spatial scales comparable to the urban heterogeneities. On the other hand, mesoscale circulations happen on a scale of several kilometres. Bringing both scales together is the key effort when including urban areas in mesoscale models.

In vertical dimensions, the resolution in the urban canopy should be about the order of 1 m and a time step proportional to Δx (where Δx is the grid-spacing) would be needed for fulfilling the Courant-Friedrichs-Levy (CFL) condition necessary for stability while solving certain partial differential equations describing atmospheric motions. Consequently, an increase in spatial resolution of three orders of magnitude will result in a reduction in the time step of the same amount. The gap between spatial and temporal resolutions can only be closed via proper parameterisation of the sub-mesoscale processes (Martilli 2007).

In principle, there are two ways to include urban areas in mesoscale models (Taha 1999):

a) Varying the soil constants and parameters that are used in the surface heat balance equation (e.g., thermal conductivity, albedo, roughness, soil moisture)
b) Coupling of an urban canopy model to an atmospheric model

To represent different types of land surfaces and their interaction with the lower atmosphere, WRF is coupled with the NOAH- Land Surface Model – LSM (Mitchell et al. 2005) which numerically calculates relevant physical processes at each grid cell. The presence of a city has effects on momentum, turbulence and thermal exchanges between the surface and the atmosphere. A bulk urban parameterisation representing only zero-order effects of urban surfaces is already implemented within the LSM. A predefined roughness length of 0.8 m represents turbulence and drag due to buildings, an albedo of 0.15 accounts for radiative properties of urban canyons and averaged volumetric heat capacities (3.0 J m^{-3} K^{-1}) and soil thermal conductivities (2.24 W m^{-1} K^{-1}) characterize heat transfer in building fabrics. In order to better reproduce the processes induced by the city's heterogeneity, urban canopy models (UCMs) are coupled to the LSM to better account for the modification of surface energy budgets within the model (Liu et al. 2006). Such coupling is achieved through the parameter of urban fraction (F_{urb}) that represents the proportion of impervious surfaces in the WRF sub-grid scale. For any given grid scale

defined as ‘urban’, the LSM calculates fluxes for vegetated urban areas, whereas the UCM treats fluxes induced by anthropogenic surfaces (Chen et al. 2011b).

The skin temperature is approximated from the weighted areal coverage of impervious and natural surface temperature (Chen et al. 2011b). Owing to the coarse resolution of 1 km at best, surface properties have to be averaged for one grid cell according to the predefined land use.

Urban canopy models include sensible heat fluxes from roof, wall and road surfaces and aggregate them into the exchange of momentum and energy between the urban surface and atmosphere. Surface temperatures are calculated from the upward long wave radiation. Wind shear calculations allow for increased roughness, shadowing from buildings and characteristic radiative properties within street canyons. Thermal properties of building materials, as with the additional heat generated by human activities, are considered as well (Chen et al. 2011b).

Initially, three different urban categories are defined within WRF urban canopy models. Low-intensity residential (class 31) includes areas with a mixture of built-up structures and vegetation with vegetation accounting for 20-70% of the land cover. In contrast, vegetation is under 20% for high-density residential areas (class 32). Industrial/commercial (class 33) includes infrastructure and highly developed areas not classified as residential (USGS 2006).

Different urban parameterization schemes are available in WRF. Two of them are tested for their ability to model local climate and circulation patterns for the test bed of Stuttgart. In general, there is a simpler *Single Layer Urban Canopy Model* (SLUCM) (Kusaka et al. 2001) as well as the more detailed multi-layer *Building Effect Parameterization BEP* (Martilli 2002). Schematic diagrams of both schemes are shown in Fig. 15.

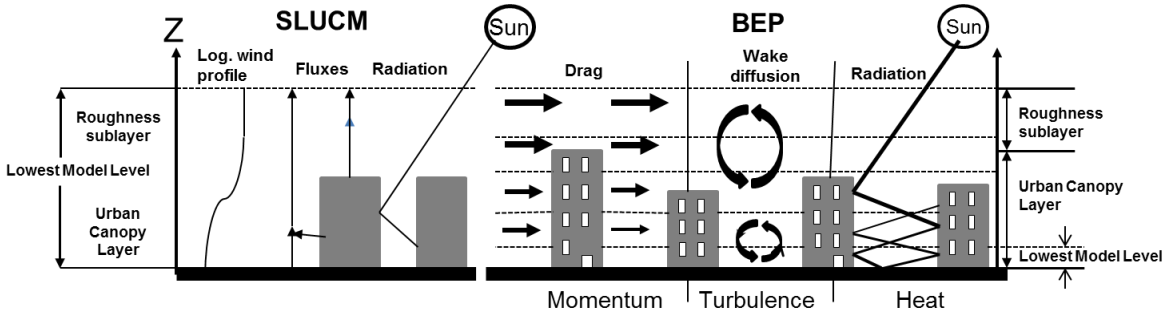

Fig. 15: Schematic figure of the Single Layer Urban Canopy Model (Kusaka 2001) (left) and the multi-layer model: Building Effect Parameterization (Martilli 2002) right. These differ in representing the processes in the urban canopy layer (Chen 2011)

6.1.1 Basic Concept of SLUCM in WRF

The SLUCM (Kusaka 2001) assumes infinitely long street canyons representing shadowing, reflection and radiation trapping in the street canyon and specifies an exponential wind profile. The model considers the three-dimensional nature of urban surfaces including both canyon orientation and diurnal variation of solar azimuth angle. Surface temperatures of walls, roofs and roads are derived from the surface energy balance (equation 3.2) and from various surface fluxes. The surface sensible heat flux is computed using Monin-Obukhov similarity theory. The canyon drag coefficient and friction velocity is approximated by a similarity stability function for momentum. SLUCM uses about 20 parameters describing the canyon dimension and surface parameters to be adapted according to the area under investigation (Chen et al. 2011). The current state of the atmosphere is the boundary condition forcing the canopy model. By an explicit time stepping, modified variables and physical constants due to the presence of an urban surface are used to update the atmospheric model.

a) Short and long wave radiation

The building height plays an important role in the radiative properties of an urban area. Therefore, the model treats shadowing, radiation trapping and reflection of shortwave and longwave radiation, whereas the surface is assumed to act like a lambertian emitter. The amount of incoming solar radiation on a central point within the urban canyon is calculated from the latitude dependent solar zenith angle and the normalized building and road width. The net amount absorbed by the roof is obtained from

$$S_R = S_D(1 - \alpha_R) + S_Q(1 - \alpha_R), \quad (6.1)$$

with S_D and S_Q representing direct and diffuse radiation received at the surface and α the surface albedo. The implementation of wall and road surfaces is similar, but gets more complex when including the three dimensional geometry of the street canyon. Sky and road view factor for the wall and wall view factor for the road are calculated by integrating different sky view factors on arbitrary points on the surface areas. Canyon orientation is assumed to be homogenous.

The net long wave fluxes are calculated for each surface and dependent on the emissivity and temperature of the walls, roofs and roads according to the Boltzmann Radiation Law,

$$L^* = \varepsilon(L\downarrow - \sigma T^4). \quad (6.2)$$

b) Sensible heat flux and wind speed

The sensible heat flux is calculated at each surface separately by using Jurges's formula for a wall and road and including a replaced canyon surface temperature (Kusaka et al. 2001). Wind speeds at different heights are included additionally. The air within the urban canopy layer has a negligible heat capacity, so the sensible heat flux H through the canyon top can be presented in a simplified way by the area averaged (ω) heat fluxes from two walls and one ground surface:

$$\omega H = 2hH_w + \omega H_G. \quad (6.3)$$

Due to anthropogenic heat production, additional heat sources are to be added. The roughness length for heat and the total momentum fluxes are based on Monin-Obukhov similarity theory. The mean wind speed in the canyon is used as a reference to calculate H_W and H_G. The wind profile within a canyon is exponential.

c) Surface temperatures

In order to obtain the surface temperatures of the wall, road and roof, the one-dimensional energy conservation equation is solved numerically, whereas the boundary condition is a constant temperature (zero heat flux) at the bottom of the canyon. The ground heat flux $G_{Z,i}$ and interior temperatures $T_{Z,i}$ with depth Z at the i surface are calculated as

$$G_{Z,i} = -\lambda i \frac{\partial T}{\partial z} \tag{6.4}$$

and

$$\frac{\partial T_{Z,i}}{\partial t} = -\frac{1}{\rho_i c_i} \frac{\partial G_{Z,i}}{\partial z}, \tag{6.5}$$

where λ is the thermal conductivity and ρc is the volumetric heat capacity that is specific to surface i (Kusaka 2001). Exact formulations and extensions of equations describing the full functionality of the SLUCM are not discussed here, but can be found in Kusaka (2001).

6.1.2 Basic concept of BEP in WRF

The Building Effect Parameterization BEP (Martilli 2002) accounts for the three-dimensional nature of urban surfaces and treats the buildings as sources and sinks of heat, moisture and momentum. By impacting the thermodynamic structure of the urban roughness sub-layer in the lower part of the urban boundary layer, the BEP allows a direct interaction with the PBL. The effects of horizontal and vertical surfaces on the turbulent kinetic energy (TKE), potential temperature (Θ) and momentum are also covered by this model by allowing a high vertical resolution close to the ground. For these simulations, the internal temperature of the buildings is assumed to be constant (Chen 2011

In the BEP, a city consists of a combination of different urban classes. Each class is characterized by an arrangement of buildings of the same canyon width but with a distribution of different heights h according to a certain probability. The length of the street canyon is thereby consistent with the horizontal grid size.

The urban structure however is defined on a grid different from the mesoscale model to provide the greatest flexibility in calculating sub-scale processes. Areas of urban surface types are defined with regard to the total horizontal and vertical surface area. The crucial effects of urban surfaces on atmospheric dynamics are computed as follows (Martilli 2002):

a) Effects on airflow

The presence of horizontal surfaces like roofs and the ground induce a consequent loss of momentum due to the generation of a frictional force. This term is similar to the mesoscale model, with the exception that it is vertically distributed from the ground up to the highest building. Moreover, it is proportional to the fractional area of the horizontal surfaces existent in the cell. In general, momentum fluxes are produced due to the presence of vertical surfaces of the buildings (Martilli 2002).

Momentum

The turbulent flux of momentum due to horizontal surfaces is calculated for every model level in the urban canopy using the Monin-Obukhov Similarity Theory (MOST). The flux at level U on the urban scale is thus computed using the wind speed and air temperature at some level M calculated at the mesoscale model grid. The roughness length is represented by the roughness of the specific surface types (roof or canyon floor). Buildings induce pressure and drag forces on the flow which is used accordingly to parameterise the exchange of momentum on vertical structures (walls). This approach can be compared with modelling the impact of vegetative canopies on the flow. All forces explained above occur orthogonal to the direction of the street canyon and have components against the horizontal wind direction. The exact equations are presented in Raupach (1991) for horizontal and in Louis (1979) for vertical surfaces. For an overall explanation and calculation within the BEP model, refer to equations (13) and (14) presented in Martilli (2002). Changing some features of the building geometry can modify relevant parameters which results in an alteration of modelled momentum fluxes

Temperature

The turbulent fluxes of sensible heat from the roof and canyon floor are mainly calculated from the gradient between the air and surface temperature and described accurately by equation (15) in Martilli (2002) with reference to Louis (1979).

Temperature fluxes from the wall are also a function of the gradient between the air and wall temperatures and calculated from the sensible heat coefficient as a function of the wind speed between the buildings (calculated by an urban canopy budget model in Arnfield and Grimmond (1998) using a formulation by Clarke (2001)). The temperature of

roofs, walls and streets are computed by solving a heat diffusion equation for several levels in the materials whereas surface-specific energy budgets are computed. Details of this calculation are given in the appendix of Martilli (2002).

By increasing the surface albedo by using light façades and roof colours, or urban greening, one can significantly impact the temperature fluxes within the urban canopy.

Turbulent kinetic energy

In urban areas, the conversion of mean energy into turbulent kinetic energy is increased by the presence of buildings. In the BEP, this aspect is calculated by the impact of the surface at the lowest level in the shear and buoyant production terms of the turbulent kinetic energy (TKE). The considerations are similar with those of momentum fluxes, but since the effect is considered to be volumetric, the terms of the MOST-equation are multiplied by a reference volume above the surface (Martilli 2002).

b) Computation of urban terms

In urban areas, the general energy conservation equations are modified by an extra term $D_{A,}$ where A can be any variable like temperature, wind speed or TKE. This extra term is generated by fluxes due to interactions between buildings and the airflow. It can be simplified by the following equation:

$$D_A = \frac{Fa^H + Fa^V}{V^A}, \tag{6.6}$$

with V being the volume of air in a grid cell and Fa^H and Fa^V the average of the fluxes computed on the urban grid due to the presence of buildings and interpolated to the grid of the mesoscale model (Martilli 2002).

c) Modification of the turbulent length scale

In order to estimate the dissipation of TKE, the parameter of the turbulent length scale l is introduced. In general, the term turbulent length scale defines a physical variable describing the size of the large energy-containing eddies in a turbulent flow. The presence of a building generates vortices which are of the order of the building's height. Whereas lower levels are influenced by both high and small buildings, higher buildings are predominantly affected by self-induced eddies. Consequently, the myriad of buildings

leads to an increased energy transfer from the mean kinetic energy to the TKE which consequently increases the dissipation rate. Compared to usual mesoscale modelling, the BEP uses an approach to modify the length scales by an 'urban' term.
Detailed information about all terms and equations used in the BEP model are given in Martilli (2002) and a short user's manual is given in Martilli et al. (2009).

6.2 Setting up WRF for real data application

6.2.1 Input data

The urban canopy model has to be adapted to the geometrical features of the urban area of Stuttgart. Relevant parameters are retrieved from observational data or set to predefined values specified in Chen (2011). For each urban class, parameters are defined to represent properties like building height, street width, surface albedo or vegetation cover in addition to building and street orientation, as well as thermodynamic properties and roughness features.

By default, WRF implements a 24 class USGS land use classification, incorporating only one single urban class. To use the UCM to its full capacity, it is mandatory to extend and reclassify the existing database in order to distinguish between three urban land use classes instead. For this reason, the basic USGS land use classification is replaced by CORINE 33 class land cover data (EEA 2000). Several steps have to be considered within this self-created process of land use transformation. First, the basic WRF land use data has to be transferred from binary format to a grid based latitude/longitude format readable by a cartographical analysis tool (ArcGIS 10.1). Second, the old land use grid is replaced by the new land use data with regard to the dimension of the initial WRF land use tile. The re-classified land use tile is then re-transferred to binary format and implemented within the existing WRF geographical database (Fig. 16). A full documentation of the land use processing is given in the appendix A.1.

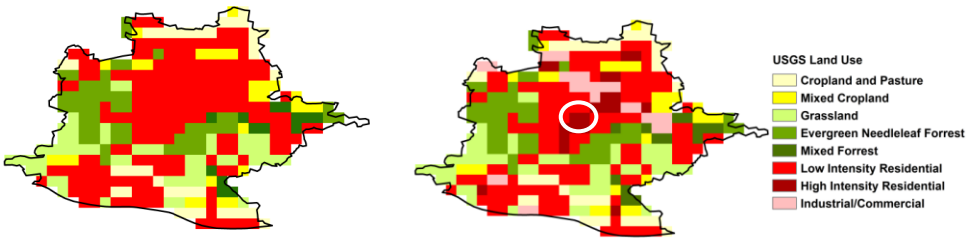

Fig. 16: Urban area of Stuttgart (200 km²) before (left) and after land use transformation. The white circle indicates the central urban grid cell used for evaluation and sensitivity tests.

After the process of land use transformation, we are able to distinguish between the 3 different urban classes: low-intensity residential (class 31), high-density residential areas (class 32) and industrial/commercial (class 33). Fig. 17 gives a visual impression of the 3 classes to be found in the urban area of Stuttgart.

Fig. 17: Aerial photography showing as low density residential 31 (left), high density residential 32 (middle) and industrial/commercial 33 (right) (Source: Google Earth)

According to Fig. 16, the urban area of Stuttgart extends to about 200 km². In the model it is represented by 200 grid cells. Within this area, 45% is classified as urban, from which 80 % is defined as low density residential, 7 % as high density residential and the remaining 13 % as industrial and commercial areas.

Mean building heights for each urban class are calculated from a high resolution digital elevation model which resolves the height of every building. It is supplied by the land surveying office of Stuttgart (2012) (*'Landesamt für Geoinformation und Landentwicklung Baden-Württemberg'* - LGL). A 30 m land use classification retrieved from Landsat satellite data is used to mask the DEM according to the appearance of the certain land use class (Fig. 18). The landuse data can be obtained from the data- and map service of the

'Landesamt für Umwelt, Messungen und Naturschutz Baden-Württemberg' (LUBW) (LUBW 2014).

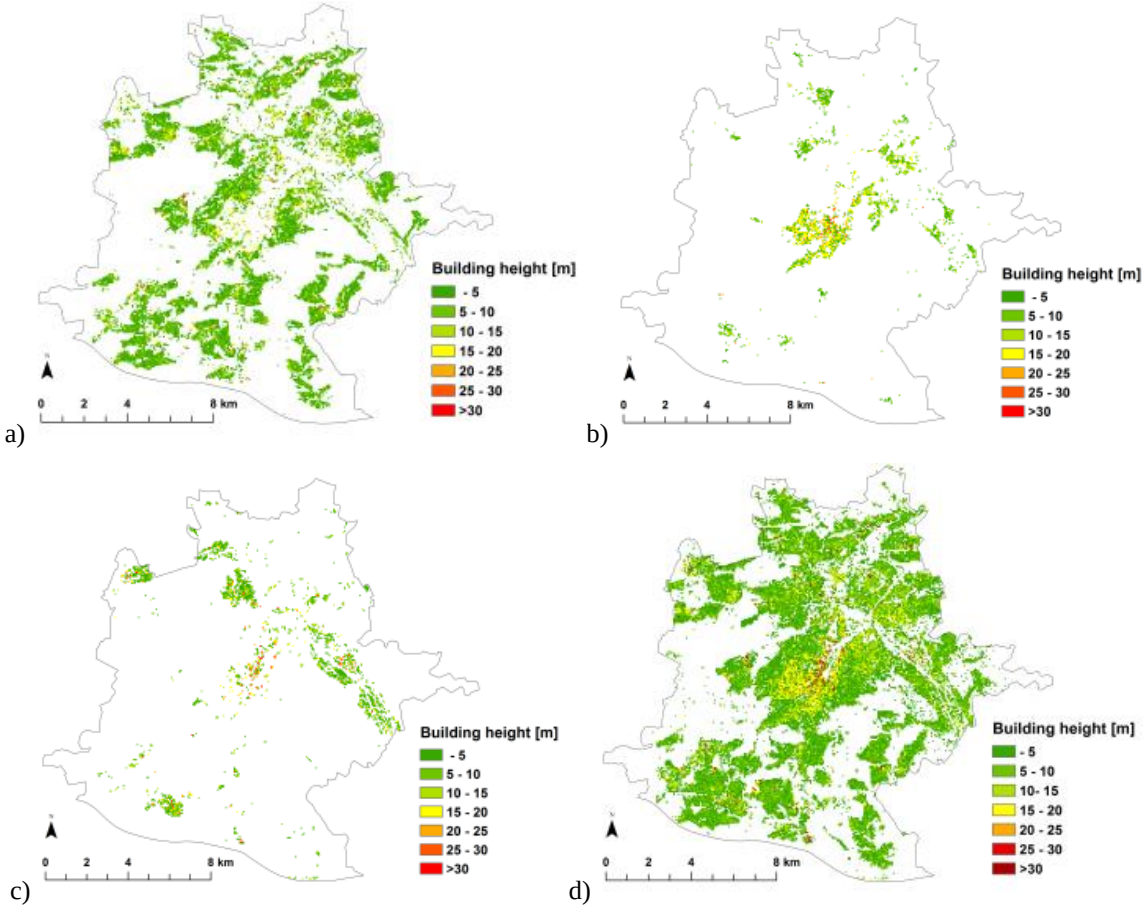

Fig. 18: Building heights extracted from high resolution DEM resolving every building height for one of the three defined urban classes according to the LUBW (2014) dataset: 31: low density residential (a), 32: high density residential (b), 33: industrial/commercial (c) and all three land use classes combined. (Geobasisdaten © Landesamt für Geoinformation und Landentwicklung Baden-Württemberg, www.lgl-bw.de, Az.: 2851.9-1/19)

Mean building heights in Stuttgart range from 5 m as mainly found in the low density residential areas, to over 30 m for some buildings in the city centre. The mean values for each class are implemented in the urban parameter table (Tab. 3).

Orientation and the mean width of roads are visually obtained from Google Maps images and only roads at a 90° and 0° inclination from the north are counted. The averaged road width per cardinal direction and urban category is then estimated from selected samples. The road width parameter is important for calculating the airflow within the urban canopy model.

Anthropogenic heat (20-90 W/m²) and other thermal and dynamical urban parameters are included using the estimated values proposed by Chen (2011). The complete set of parameters used for the urbanization of WRF is displayed in Tab. 3:

Tab. 3: Urban parameter table for input to the urban parameterization scheme. Parameters are derived for the three CORINE based urban classes: commercial (33), high density (32) and low density residential (31). The lower part of the table is only valid for the BEP by representing the distribution of the buildings in height and street characteristics for each class (changed from Chen 2011)

Urban Parameter	Commercial	High Density	Low Density
ZR: Roof level (building height) [m]	8.5	9.7	6.4
SIGMA_ZED: Standard Deviation of roof height [m]	6.8	6.4	4.5
ROOF_WIDTH: Roof (i.e., building) width [m]	27.5	13.3	10
ROAD_WIDTH: road width [m]	19	16.2	18
AH: Anthropogenic heat [W m/m²]	90	50	20
FRC_URB: Fraction of the urban landscape which does not have natural vegetation [Fraction]	0.95	0.85	0.5
CAPR: Heat capacity of roof [J m³/ K]	1.00E+06	1.00E+06	1.00E+06
CAPB: Heat capacity of building wall [J m³/ K]	1.00E+06	1.00E+06	1.00E+06
CAPG: Heat capacity of ground (road) [J m³/ K]	1.40E+06	1.40E+06	1.40E+06
AKSR: Thermal conductivity of roof [J/ msK]	0.67	0.67	0.67
AKSB: Thermal conductivity of building wall [J/ms K]	0.67	0.67	0.67
AKSG: Thermal conductivity of ground (road) [J /ms K]	0.4	0.4	0.4
ALBR: Surface albedo of roof [fraction]	0.2	0.2	0.2
ALBB: Surface albedo of building wall [fraction]	0.2	0.2	0.2
ALBG: Surface albedo of ground (road) [fraction]	0.2	0.2	0.2
EPSR: Surface emissivity of roof [-]	0.8	0.9	0.93
EPSB: Surface emissivity of building wall [-]	0.8	0.95	0.94
EPSG: Surface emissivity of ground (road) [-]	0.95	0.96	0.97
Z0B: Roughness length for momentum, over building wall [m]	0.0001	0.0001	0.0001
Z0G: Roughness length for momentum, over ground (road) [m]	0.01	0.01	0.01
Z0R: Roughness length for momentum over roof [m]	0.01	0.01	0.01
AKANDA_URBAN: Coefficient modifying the Kanda approach to computing surface layer exchange coefficient	1.29	1.29	1.29
TBLEND: Lower boundary temperature for building wall temperature [K]	293	293	293
TGLEND: Lower boundary temperature for ground (road) temperature [K]	293	293	293

Street Parameters

Urban Category [index]	street direction [geg from N]	street width [m]	building width [m]
33	0	19	25
33	90	19	25
32	0	15	13
32	90	15	13
31	0	18	10
31	90	18	10

Building Heights

height [m]	33 Percentage [%]	32 Percentage [%]	31 Percentage [%]
5	44	33	48
10	26	20	37
15	14	23	11
20	8	18	3
25	4	4	1
30	2	2	
35	2		

Referring to Tab. 3, the main features which are to be adapted according to the local urban characteristics are the building heights (ZR), their standard deviation (SIGMA_ZED) as well as the roof width (ROOF WIDTH) and road width (ROAD_WIDTH). These four parameters define the morphology of the urban canyon in WRF. According to Oke (1982), the sky view factor (SVF) can be calculated from the ratio between ZR and the road width. Applying eq. (3.8) from Chapter 3.4.3 in Oke 1982), the settings defined in Tab. 3 result in a mean SVF of 0.65. Values for different urban classes are shown in the table below:

	33	32	31
H	8.5	9.7	6.4
W	19	16.2	18
H/W	0.45	0.60	0.36
SVF	0.72	0.63	0.78

Tab. 4: Sky View Factors calculated from building height H and road width W according to the formula of Oke (1982)

In the default configuration used by Tewari (2007), parameters are referred to a standard American city which would result in a mean SVF of 0.51. This lower value mainly results from differing building geometries assumed for class 33. Skyscrapers, which are mainly found within a central business district (CBD) of a standard American city, are dominating this class. A mean SVF of 0.42 is assumed here compared to 0.72 calculated from the model input data with respect to a mid-European city (Stuttgart).

Within the urban canopy model (‘module_sf_urban.F’), urban parameters are initialized based on the information from Tab. 3 and used by the multi-layer module (‘module_sf_bep.F’) by looping over 13 vertical layers in the canyon, 2 street directions and 7 different building heights. The calculations are processed on an urban grid and the modified fluxes re-interpolated to the NOAH land surface model of WRF.

Initial meteorological conditions are obtained from the ECMWF ERA Interim 0.5° resolution reanalysis data (Dee et al. 2011). It consists of a set of global analyses describing the state of the atmosphere and land and ocean-wave conditions from mid-1957 to mid-2002.

For Stuttgart located in complex terrain, it is important to provide topographical input data with sufficiently high resolution (USGS). With regard to Fig. 19 (left), the city is embedded in an area with heterogeneous terrain heights ranging from below 160 in the north-western part in the direction to the Rhine valley, up to more than 750 m towards the Swabian Alb (south-east). The topography in the urban region (right) ranges from less than 250 m NN in the city centre to almost 500 m NN in the south-western part. The topographical situation has a significant impact on airflow and promotes distinct circulation patterns. The trapping of heat and air pollutants are two negative side effects.

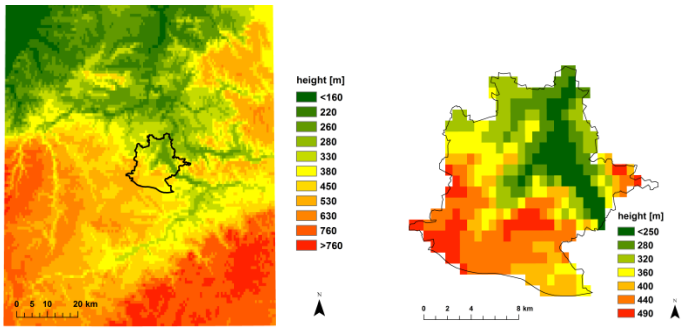

Fig. 19: Topographical input data used for WRF at the highest resolution of 1 km (30s). The extent does not correspond to the actual domain size (left). The topography as displayed only for the urban area of Stuttgart (right)

Next to land use and terrain data, WRF needs several inputs that characterize the geographical properties of the study area. For this reason, the classification of soil types, soil temperatures, and the green vegetation fraction and slope information are implemented within the modelling framework. These properties are retrieved from the default settings from WRF Version 3.2 (Skamarock et al. 2005)

Whereas the three dimensional nature of urban canopies is represented by an urban parameter table (*URBPARM.TBL*) as explained above, additional information is needed to characterize the radiative properties of natural and impervious surfaces to then be processed in the land surface model (NOAH-LSM). In WRF, this additional information is basically retrieved from two tables (*LANDUSE.TBL and VEGPARM.TBL*). With regard to the modified land use database, both tables have to be extended from the default 24 to 33 classes. Specifications of both tables are presented in the Appendix Figure A.2 and A.3.

6.2.2 Processing an urbanized WRF run

Basically, the WRF framework includes 2 main components: a pre-processor (WPS) and a main processor (WRF). WPS aggregates the global ERA-Interim meteorological boundary conditions to the WRF-grid according to the spatial dimensions of the model domains, the vertical resolution, the geographical input data and the modelling period (August 11 – August 17 2003). Three basic programs are needed for data processing in WPS:

- *Geogrid.exe* generates a 2-dimensional geographical input file with the predefined horizontal dimensions
- *Ungrib.exe* transfers the ERA-Interim Reanalysis data files to a WRF readable format

- *Metgrid.exe* aggregates the vertical information from the meteorological boundary conditions to the horizontal WRF grid for each domain and daily time step.

A two way nesting approach to include three domains is defined with a horizontal resolution of 1 km and 36 vertical levels. The lowest model level accounts for an atmospheric layer of ~11 m depth. Any result of this work, which refers to this level, describes the average value for this column. For higher levels, the layers get thinner and the numbers approximately equal the 'real' height. The innermost domain covers an area of 64 x 49 grid cells within the urban area of Stuttgart (200 grid cells) and is located in the centre (Fig. 20). The basic settings of WPS are defined in the file 'namelist.wps'(Appendix A.4). All times refer to GMT +2, daylight saving time for the Central Europe.

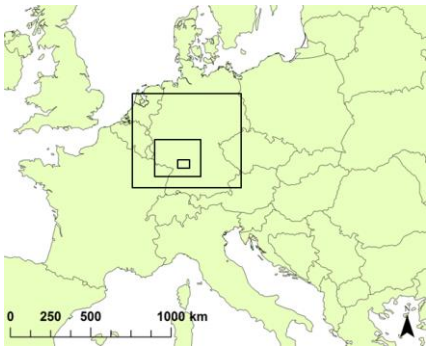

Fig. 20: Model domains 1,2,3 for the WRF run projected to UTM WGS84 Europe Zone 32N

In the following, the previously generated meteorological files are linked to the WRF main processor for real data applications ('em_real'). It is mandatory at this point that the correct number of land use classes (33) has been set within an index file in the geographical data repository and within the general WRF configuration file 'Registry.EM' (num_landcat=33).

Within the main processor WRF, the meteorological boundary conditions are used to drive the mesoscale model. At this stage, the appropriate physical schemes are to be set in the configuration file 'namelist.input'. The selection and combination of physical schemes defines the way the model solves the equations of motion and the calculation of output variables. Other specifications like modelling time steps, runtime, debugging mode or domain specifications are to be set here as well. The three parameter tables for vegetation, land use and urban characteristics are also introduced at this stage of the modelling. In order to save computing time, the urban canopy model is only applied within the third domain with the 1 km resolution. Next to general settings which are not to be discussed

into detail here, there are a number of configurations which have to be considered when using an urban canopy model in WRF. In particular, the setting up of the multi-layer canopy model 'BEP' requires the selection of specific physical schemes (Martilli 2002). In order to avoid strong oscillations that may arise due to changes in roughness at the border of the city, a 6^{th} order filter is preferred. NOAH-LSM is the only land surface model which operates with the BEP. For calculating the planetary boundary layer, the Mellor-Yamada-Janjic (Hu et al. 2010) parameterisation is used to better represent the vertical structure of the urban atmosphere. Within this scheme, the PBLH is directly related to the turbulent kinetic energy term TKE. By this, it is defined as the height, were the TKE drops below 0.01 $m^{-2}s^{-2}$. Further specifications of the two urban canopy models can be found in (Martilli et al. 2009) and (Tewari, Chen, Kusaka, & Miao 2007). The urban canopy model in theory runs independently by using the meteorological information of the mesoscale model and urban parameters from the specific tables. Building and street parameters are defined on the urban grid with a horizontal resolution of 5 m and with a maximum of 13 vertical levels in the urban canopy. The terms of sources and sinks are calculated on the urban grid as well. Finally, the modified variables are re-interpolated to the mesoscale grid. Parallel with this, the NOAH land surface model calculates fluxes for natural surfaces. The modelling integration time step is set to 30 seconds with model output generated on an hourly basis. The final version of the WRF configuration file equals to that one of the chemical run (appendix A.6). The basic settings of the WRF run are presented in Tab. 5:

Tab. 5: Modelling setup used for meteorological part according to Skamarock et al. (2005)

Parameter/Scheme	Specification	Parameter/Scheme	Specification	Parameter/Scheme	Specification
geographical input data	1km USGS land use	lowest model level	10 m	shortwave	RRTMG
dx, dy	15km, 3km, 1km	meteorological BC	0.5 Deg ERA-Interim	land surface model	Noah LSM
west-east [km]	750, 228, 61	time frame	8/11 - 8/17/03	urbanization scheme	BEP/ SLUCM
south-north [km]	600, 168, 49	microphysics	Lin et al	cumulus scheme	Kain-Fritsch
vertical layers	36	longwave	RRTMG	boundary layer	MYJ

The simulations for the meteorological part are performed on the IMK-IFU water and climate 64 bit high performance computing (HPC) cluster KEA, which is specifically designed for parallel applications. For compiling the WRF code and performing the control and the scenario runs, 48 central processing units (CPUs) of an AMB Opteron computer, type Magnycour are used. A regular urbanized WRF-run with three nested domains with a 1 km resolution for simulating a 7 day period is executed in about 8 hours computing time. The ratio between the computational and real-time hours accounts for $\frac{1}{21}$.

6.2.3 Sensitivity study

With the parameters adapted for the urban area of Stuttgart, the sensitivity of three different urban schemes - SLUCM, BEP or bulk approach – to observed temperature and wind speed is tested. The observational data is retrieved from the meteorological station *'Stuttgart Schwabenzentum'* located in the centre of the city (48.77° N 9.18° E). Data is recorded continuously since 1986 at a height of 20 m and supplied by the Environmental Protection Agency of Stuttgart.

Three model runs are performed, each using a different urban scheme. To validate modelled temperature and wind fields, results for each urban scheme are extracted for a single grid cell in the urban centre (Fig. 16) and compared against observations from a measurement station located within this pixel (1 km²). For this reason, the potential 20 m air temperature is taken from the WRF output and compared against measured temperatures at one location for the whole time frame (August 11 - August 17 2003).

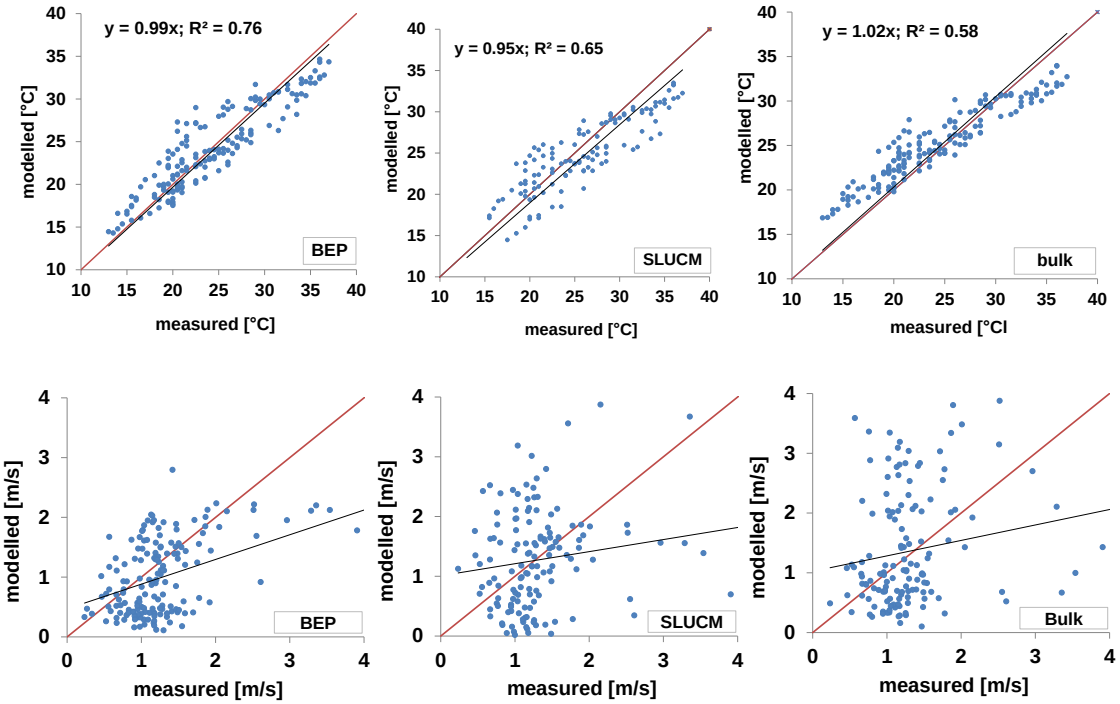

Fig. 21: Comparison between measured and observed 20 m potential temperature (upper three plots) and 20 m wind speed using BEP (left), SLUCM (middle) and the Bulk approach (right). Measurement station '*Stuttgart Schwabenzentrum'* is located in the centre of the innermost domain and the centre of the urban area of Stuttgart. Model output is retrieved for the central urban grid cell as pointed out in Fig. 16.

With a coefficient of determination (R^2) of about 76 %, the Building Effect Parameterisation scheme seems to be the most suitable for reproducing the thermal

conditions of the test area. The SLUCM approach shows a reduced R^2, as does the bulk approach using no particular urban parameterization. By using this setup, it seems that WRF is not able to capture the prevailing wind speeds for this period very well. Only the multi-layer approach is able to reproduce the observed wind speed by a certain amount (R^2=0.27). For the other schemes a comparison is not possible. For wind speed showing very heterogeneous trends, it is even more difficult to compare grid averaged wind speed with a point measurement. In general, the BEP approach simulates an average wind speed of 1.2 ms^{-2} for the central urban grid cell, underestimating the mean observed value by 0.4 ms^{-2}. The simulated 15 m wind speed accounts for 1.5 ms^{-1} with regard to the single layer – and for 1.8 using the bulk approach. Due to the lack of vertical temperature observations in the urban centre, profiles can only be validated for the rural station *'Stuttgart Schnarrenberg'*, which is located about 7 km north-east from the city centre at an elevation of 320 m NN, compared to the 227 m of *'Stuttgart Schwabenzentrum'*. Fig. 22 shows the profiles of dry temperature (TC), wet-bulb temperature (TD) and horizontal wind speed for August 13 2003 1200 h, comparing radiosonde data and WRF model output. The observational data is provided by the global atmospheric soundings database of the University of Wyoming, College of Engineering, Department of Atmospheric Science and can be downloaded from http://weather.uwyo.edu/upperair/sounding.html.

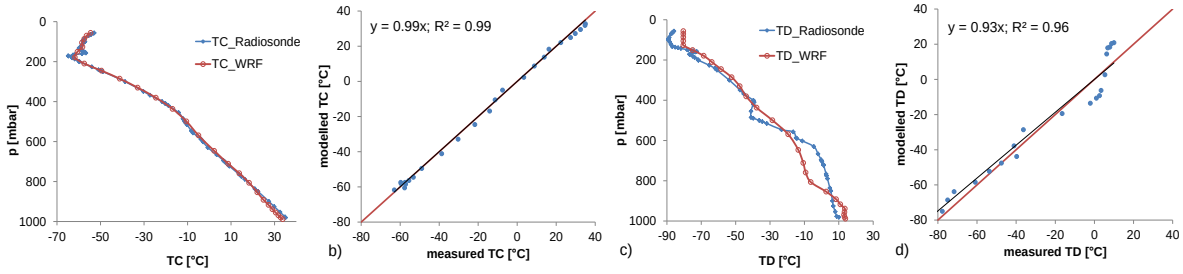

Fig. 22: Comparison between radiosonde data and WRF output at *'Stuttgart Schnarrenberg'* for August 13 2003 1200 h. Dry (a) and humid air temperature (c) are compared. Scatter plots show the correlations for TC (b) and TD (d)

Fig. 22 indicates a good representation of vertical dry and humid temperature profiles. Both variables show the largest deviations in the bottom layers with an underestimation of the observed value of about 1.2 °C with regard to TC and an overestimation of almost 3 °C for TD. In general, the modelled results show quite good agreement with the observations (Fig. 22b,c). Comparing profiles of the horizontal wind speed for the same period of time

(Fig. 23a), a quite good agreement can be observed as well. The scatter plot (Fig. 23b) confirms this result by showing a coefficient of determination of 0.87.

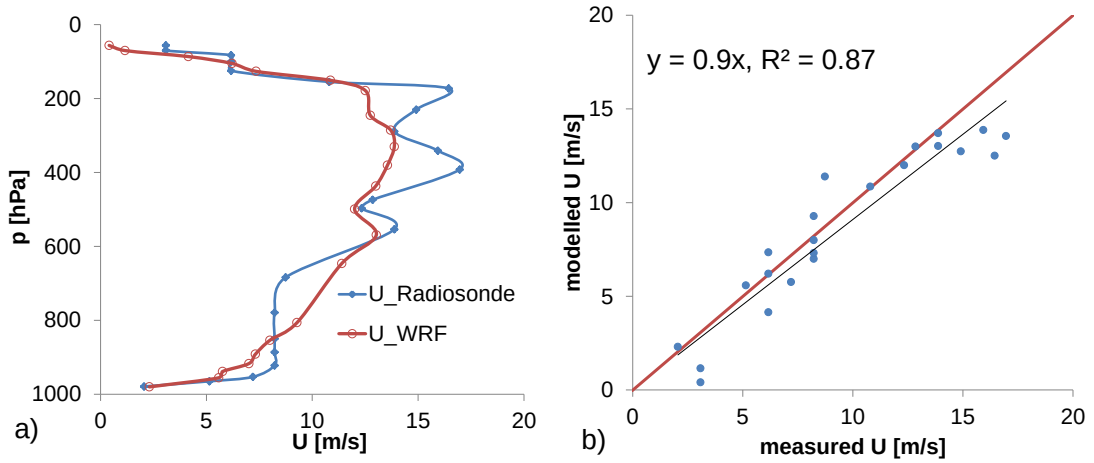

Fig. 23: Observed (blue) and modelled (red) horizontal wind speed at 'Stuttgart Schnarrenberg' on August 13 2003 1200 h (a) and scatter plot comparing the two data sets (b)

By using different urban canopy models, vertical profiles of horizontal wind speed and temperature show different characteristics (Fig. 24).

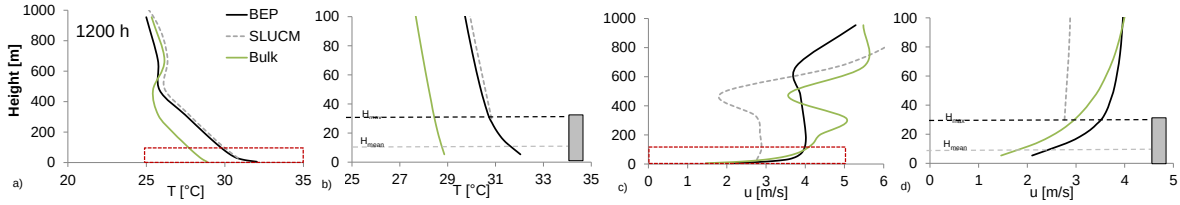

Fig. 24: Simulated vertical profiles for actual temperature (a-b) and horizontal wind speed (c,d) at noon August 13 2003. The plots concentrate on the first 100 m including the urban canopy height indicated by maximum (dark dotted line) and mean building height (light dotted line).

At noon, the bulk approach simulates potential temperatures in the lowest model level which are about 3-4 °C lower than projected with the BEP approach (Fig. 24a, b). Due to limitations in vertical resolution, the SLUCM barely allows the lowest model levels of about 30 m (maximum roof level height) which makes it impossible to draw conclusions for temperature characteristics in between the urban canyon. At about a 500 m vertical distance, the influence of the urban canopy model is reduced and the simulated temperature corresponds to the bulk approach. In general, a temperature decrease within the first 500 m can be observed for all three approaches with an intensity of about 1 °C per 100 m. During the solar noon (a), a distinct temperature inversion develops above that height

where temperatures start to increase again for the next 200 m and decrease again at a height of 700 m. According to model output, this value reflects the height of the planetary boundary layer (740 m) simulated for this time step (Aug 13 2003 1200 h). The same effect can be observed within the profile of horizontal wind speed for the curve representing the BEP approach (black). Here, the top of the boundary layer can clearly be distinguished by an abrupt increase of the wind speed (c). Compared with the Bulk and the SLUCM approach, the BEP scheme simulates a constant wind speed from the top of the canopy layer up to the boundary layer, which can be attributed to a barrier generated by strong advection over the city. This effect is generated by neither the Bulk nor the SLUCM approach (c). Both Bulk and BEP models show a decrease in wind speed within the canopy layer (d).

Corresponding to the results from the sensitivity study, the multi-layer BEP scheme is applied for conducting different scenario runs and analysing the effect of several urban planning scenarios on urban heat island and temperature.

6.2.4 Mitigation Scenarios

a) Urban Greening

This scenario will be accomplished by running two different urban greening simulations. The first is the ‘Central Park’ scenario where 25 grid cells classified as urban in the centre of Stuttgart are replaced by natural vegetation. This change accounts for 25 km² or approximately 12% of the total city area transferred into grassland. For the other urban greening scenario (‘Many Parks’), several smaller green areas are installed. The sizes of these parks within the city borders are equal and their total area is the same as in the ‘Central Park’ simulation. The transformation from an impervious surface into vegetation is represented by changing the characteristic parameters. These modified parameters create new boundary conditions for the NOAH LSM and WRF such as an increased albedo from 0.17 to 0.23, increased soil moisture, surface emissivity and vegetation fraction. The roughness length as used by the land surface model is reduced from about 80 cm to 12 cm when replacing urban surfaces by grassland.

b) Albedo

Changing the reflectivity of buildings in the model can be achieved by changing the albedo of roofs and building walls in the urban parameter table from 0.2 to 0.7. This results in the modification of radiative terms in the energy balance equation (3.2). Below, this scenario is represented by the term ‘Albedo’.

c) Building density

This scenario reflects a direct intervention in the building structure. Within the urban table, the proportion of roof width to road width is increased by 20% which in turn results in more area being covered with natural vegetation such as trees and grassland. The SVF is increased too. This scenario is identified by the term ‘Density’ below.

6.3 Basic configuration of WRF-Chem

WRF-Chem (Grell et al. 2005) is used in order to assess the effect of UHI mitigation strategies on atmospheric chemical composition. For reasons of computational limitations, the domain structure is slightly changed in WRF-Chem. Only the coarse domain of the WRF run (Fig. 20) is used within this approach with a horizontal resolution of 3 km. Initial emissions are obtained from the MACC 2003-2007 emission inventory with 7 km resolution (Kuenen et al. 2011). The emissions are converted to effective concentrations and consequently aggregated to the model-grid. The physics schemes are adapted from the previous WRF-run with a number of chemical schemes to be included and configured according to the objective target. Biogenic emissions are used from global MEGAN emission database (Guenther et al. 2012) and global chemical boundary conditions are retrieved from MOZART-Data (Horowitz et al. 2003). Different schemes are to be adapted due to the improved land use classification. Basic settings of WRF-Chem are displayed in Tab. 6:

Tab. 6: Most important parameters and schemes added to the modelling setup for WRF-Chem

Parameter/Scheme	Specification	Parameter/Scheme	Specification	Parameter/Scheme	Specification
dx, dy	3km	chemical option	RADM2, MADE/SORGAM aerosols	chemical boundary	MOZART global dat
west-east [km]	750			biochemistry	MEGAN global dat
south-north [km]	600	emission inventory	7km MACC 2006	photolysis scheme	FastJ
time frame	8/9 - 8/18/03				

The RADM2 (Regional Acid Deposition Model) scheme is applied for calculating the gas-phase chemical mechanism and the MADE/SORGAM approach represents the formation of aerosols. MADE/SORGAM stands for *Modal Aerosol Dynamics Model for Europe* (MADE) (Ackermann et al., 1998) with the *Secondary Organic Aerosol Model* (SORGAM) of Schell (2001).

6.3.1 Initialization of the new land use data in WRF-Chem

By default, WRF-Chem uses the basic 24 land use classes. A number of chemical schemes have to be adapted and settings have to be changed in order to incorporate the new land use classification as explained in Chapter 6.2.

a) Initialization

The first step which is mandatory for the correct initializing is the definition of 33 classes instead of 24 within the module 'chemics_init.F' when asking for the number of land use categories. To avoid an error message, this variable has to be changed in line 315 of the module. This setting sets the basis for processing of the new land use data in WRF-Chem.

b) Dry deposition module

The process by which aerosol particles accumulate or deposit themselves on solid surfaces is defined as deposition. As a result, the effective concentration decreases. The rate of deposition depends on particle size and, for example, on the size and distribution of obstacles or land surface characteristics. The latter is controlled mainly by the land use type in the model. In mesoscale models like WRF-Chem, the surface resistance to gaseous dry deposition has to be parameterized within suitable schemes. By changing the land use input data, these schemes have to be adapted accordingly. The basic assumptions for the calculation of dry deposition mechanisms in WRF-Chem are related to the findings from Wesely (1989). His module basically computes dry deposition velocities of SO_2, O_3, NO_x and HNO_3 and is used with the Regional Acid Deposition Model (RADM) (Wesely and Lesht 1989). The module is based on micrometeorological formulas and parameters that define the surface resistance to uptake of the gases. For RADM, additional substances include H_2O_2, HCHO and other aldehydes, organic peroxides, peroxyacetic acid, organic acids, NH_3, peroxyacetyl nitrate (PAN) and HNO_3. The effect of changes in surface

resistance due to surface wetness caused by rain and dew is also accounted for (Wesely 1989).

For correctly identifying the newly found land surface types (31,32,33) in the deposition module 'module_dep_simple.F', they have to be initialized in the source code (line 11, 20). Each land use class found in the input data is transferred to a so-called Wesely type which classifies different surface types according to their resistance to gaseous dry deposition (Wesely 1989). Analogue to Ohm's law in electric circuits, surface resistance is calculated for 11 Wesely types. For reasons of simplification, the land use classes 'high density residential', 'low density residential' and 'industrial/commercial' are combined to Wesely class 1 ('Urban Land'). With respect to the growing season, five seasonal classes are distinguished:

1. midsummer with lush vegetation
2. autumn with unharvested cropland
3. late autumn with frost, no snow
4. winter, snow on ground and subfreezing
5. transitional spring with partially green short annuals

According to Wesely (1989), the surface is divided into several layers each having a distinct resistance to dry deposition. For every Wesely type, a bulk surface resistance r_c is calculated by adding up the single resistance terms:

$$r_c = \left[\frac{1}{(r_s+r_m)} + \frac{1}{r_{lu}} + \frac{1}{(r_{dc}+r_{lc})} + \frac{1}{(r_{ac}+r_{gs})}\right]^{-1} \quad (6.8)$$

with: $r_s + r_m$: stomata – and mesophyll resistance representing the vegetation layer

r_{lu}: resistance of the outer surfaces in the canopy

$r_{dc} + r_{lc}$: deep canopy and lower canopy resistance

$r_{ac} + r_{gs}$: canopy height - and ground surface resistance

A schematic of the dry deposition model of Wesely is shown below.

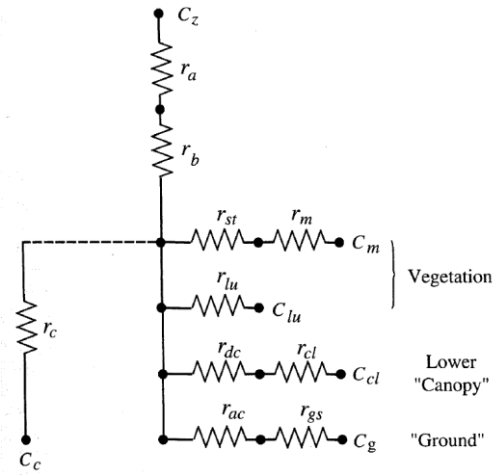

Fig. 25: Resistance schematic for dry deposition model of Wesely (1989)

According to the new land use classes, all resistance terms from equation (6.8) have to be adapted in a revised version of the dry deposition module in WRF-Chem to extend the land use array from 24 to 33 variables for each season (‘module_dep_simple.F’, line 1385 ff).

Further, an additional factor K has to be defined for every new land use class to calculate the surface deposition velocity of fine aerosols (line 2583). According to the model of Erisman et al. (1994), this value is set to 500 for Wesely class 1.

Within the dry deposition module, a simplified landuse scheme is applied for deposition and biogenic emission subroutines that follows the assumptions from Erisman (1994). This requires that the 33 land use classes are merged into 6 simplified categories:

1. Urban and bare soil
2. Agricultural
3. Grassland
4. Deciduous forest
5. Coniferous and mixed forest
6. Other natural land use categories

c) Biogenic emission module

Analogue to the dry deposition module, the correct number of land use classes (33) has to be initialized as well when calculating the biogenic emissions (‘module_bioemiss_simple.F’, line 11). Emission factors of isoprene (line 296), monoterpenes (line 420) and other VOCs (line 534) and nitrogen (line 666) have to be included in the module representing the three newly implemented land use classes. As urban use is dominating, biogenic emission factors are set to 0, 0.1 and 0.2 for the urban

class 31, 32 and 33 respectively. Again, a simplified land use scheme is applied which has to be adapted respectively.

6.3.2 Chemical initial conditions using the MACC emission inventory

In general, the modelling of the chemical composition of the atmosphere requires preliminary information about initial emissions of chemical compounds within the modelling domain. Not only the total amount is important, but also diurnal cycles and classification of different sources and the origin of emissions. Emission inventories describe the amount of pollutants discharged into the atmosphere and contain the total emissions for one or more specific greenhouse gases or air pollutants. They are generated by aggregating satellite and ground observations, models and traffic statistics, assumptions about economic development and on official reports. For closer specification of the various pollutants, it is important to know whether a source is point or area based. All the information about chemical initial conditions is interpolated to the WRF model grid, whereas diurnal cycles are included in the interpolation process. For this study, the TNO 2005 gridded emission inventory (Denier van der Gon et al. 2010) is used.

Between 2007 and 2009, a detailed European gridded emission inventory was developed referring to the year 2005. It is a European-wide, high resolution database (0.125° latitude by 0.0625° longitude) including emissions for nitrate oxide (NO_x), sulphate dioxide (SO_2) non-methane volatile organic compounds (NMVOC), methane (CH_4), carbon monoxide (CO), coarse particulate matter (PM_{10}) and fine particulate matter ($PM_{2.5}$) from the year 2005. The data for the emission inventory was collected in the course of the EU FP7 project MACC (Monitoring Atmospheric Chemical Composition) and provides the pre-operational service under the European GMES program (Global Monitoring for Environment and Security). Furthermore, it provides data records on atmospheric composition for recent years, data for monitoring present conditions and ways to forecast key parameters a few days ahead (Kuenen et al. 2011). The accuracy of the data base however is strongly dependent on the accuracy of the report from the specific countries and authorities. If certain emissions are missing or have not been reported in a sufficient quality, gaps in the database are closed by using the IIASA GAINS (Greenhouse Gas – Air Pollution Interactions and Synergies) model. This is an online model which calculates emissions based on emission factors or activity data (IIASA 2009).

Emissions have been split into point and area sources and are available in aggregated source categories. By convention, the categorisation of pollutants is based on the Standardized Nomenclature for Air Pollutants (SNAP) code. The so called SNAP level 1 classification is used for the TNO emission inventory and can be described as follows:

Tab. 7: SNAP level 1 source categories 1 to 10 classified by the emission source

SNAP	Sector name
1	Energy industries (power plants and refineries)
2	Residential combustion
34	Industry *(includes both industrial combustion & industrial processes, in previous inventories individually included as SNAP 3 and SNAP 4, now aggregated as SNAP 34)*
5	Extraction and distribution of fossil fuels
6	Solvent and other product use
7	Road transport
8	Non-road transport
9	Waste
10	Agriculture

For the TNO 2005 inventory, the emissions of transport (SNAP 7) are additionally split into 5 more detailed sub-classes:

- SNAP 71: Road transport exhaust emissions, gasoline
- SNAP 72: Road transport exhaust emissions, diesel
- SNAP 73: Road transport exhaust emissions, other fuels
- SNAP 74: Road transport non-exhaust emissions, evaporation of gasoline
- SNAP 75: Road transport non-exhaust emissions, road, brake and tyre wear

After the initial choice of data per country is made, scaling factors that relate the actual reported emissions to the year 2005 are calculated dependent on country, SNAP level, pollutant and year. Two sources have been used to determine scaling factors: GAINS emissions (IIASA 2009) and data which were officially reported by the single countries. After error checking, the final emissions are calculated for each individual grid cell, whereas each emission value is attributed to a country, SNAP code and pollutant. In the case of a grid cell being situated at a border to different countries, multiple values are given in this grid cell and are averaged based on SNAP and pollutant. To obtain the final emission value for each grid cell and year, results have to be multiplied with the scaling factors:

$$E_{c,s,p}(x,t) = SF_{c,s,p}(t) * E_{c,s,p}(x, t = 2005) \quad (6.9)$$

Here, E is the emission for the grid cell x and year t with regard to the specific country c, SNAP code s and pollutant p. SF describes the scaling factor per country, SNAP and pollutant and E the emission for the year 2005 with regard to the above mentioned parameters c,s,p and t.

To account for temporal characteristics of emissions, time profiles accounting for seasonal, weekly and daily cycles have to be added with regard to the specific SNAP code (Kuenen et al. 2011).

In order to incorporate the TNO emissions into the WRF-Chem regional modelling setup, several steps have to be conducted beforehand. Firstly, the MACC yearly emissions (ASCII - file containing total yearly emissions [t/year] for each grid cell and each of the 8 pollutants for the year 2005) have to be interpolated to the WRF grid. Accordingly, 14 files (one for each SNAP code) are generated according to the spatial dimensions of the WRF grid. By introducing dimensionless time dependent emission factors, generalized monthly, daily and hourly time profiles can be calculated from the total emissions. The actual emission for a certain point in time depends on seasonal, weekly and hourly cycles, whereas the latter two imply the human activities in the course of a day or a week. For example, the emission of nitrate oxide, which is closely linked to car exhaust, is mainly pronounced in the morning and evening hours (rush hours) and during the weekdays. In Fig. 26, urban agglomerations and road tracks can clearly be distinguished by displaying the ambient NO emissions with regard to the evening hours of a normal working day.

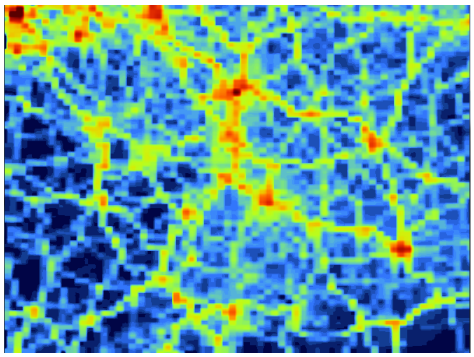

Fig. 26: MACC NO emissions for a weekday in August 2003 2000 h. Urban agglomerations can clearly be distinguished by road tracks (yellow, red)

In the following, all 15 SNAP-code related files are combined to one file and linked to the WRF modelling frame work in order to provide the chemical initial conditions for the

WRF-Chem run. The 7 km emission data has to be computationally aggregated to the 3 km model grid cell. The standardized time profiles are static on a weekly basis, enabling no distinction between weekday and weekend.

6.3.3 Boundary conditions from MEGAN biogenic emissions

Natural terrestrial eco-systems produce reactive gases and aerosols which are processed within the plant canopy and emitted into the atmosphere above. Estimates of these above-canopy fluxes are needed as additional input to air quality models. The Model of Gases and Aerosols from Nature (MEGAN) is used in this approach to quantify the net terrestrial biosphere emission (Guenther et al. 2012). MEGAN is designed for regional and global regional emission modelling and has a base resolution of 1 km² (30s latitude by 30s longitude). The emission controlling factors include biological, physical and chemical variables which are derived from models, satellite and ground observations. Annual global emissions depend on variables including temperature, solar radiation, leaf area index and plant functional type. Although a vast amount of biogenic VOCs have been identified, methane and isoprene dominate the annual global flux to the atmosphere.

The total emission for a location is estimated by summing up the single emissions calculated for each plant functional type (PFT). The emission factor of a certain canopy type is mainly based on leaf and branch scale emission measurements that are extrapolated to the canopy scale by the use of a canopy environmental model. In this way, different light and temperature distributions for different canopy types (e.g. needle and broadleaf trees) can be accounted for. Additionally, each PFT can differ in LAI or leaf area seasonal patterns (e.g. deciduous and evergreen).

The emission activity factor λ is estimated for three different options:

a) Canopy environment emission activity factor λ_{CE} as a function of PFT, monthly LAI, hourly temperature, radiation, wind speed, humidity and soil moisture
b) Leaf age emission factor λ_{age} as a function of LAI development within the past 7 to 30 days and average temperature
c) Soil moisture emission activity factor λ_{SM} as a function of soil moisture and wilting point

d) Canopy loss and production factor ρ_{iso} as a function of canopy depth, friction velocity and chemical lifetime

Data from the MEGAN model is downloaded for August 2003 and interpolated to the model grid with regard to the dimensions of the domain. An additional input netcdf file (wrfbiochemi_d01.nc) is added to the WRF-Chem processor containing the boundary conditions for biogenic emissions calibrated to modelling time and domain dimension. Next to the anthropogenic emissions (wrfchemi_d01.nc), it defines the chemical initial conditions (Guenther et al. 2006 and Guenther et al. 2012). Descriptions of standard methods and available options for calculating MEGAN variables are given in Guenther et al. (2006) Table 1.

6.3.4 Global chemical boundary conditions using MOZART

MOZART (Model of Ozone and Related Chemical Tracers) is a 3-dimensional global chemical transport model, which simulates the distribution of tropospheric ozone and its precursors. Detailed chemistry schemes for tropospheric ozone, nitrogen oxides, hydrocarbon chemistry are included in the model. Concentrations of 63 chemical species (Horowitz et al. 2003) are simulated from the surface up to the lower stratosphere. The model itself is driven by various meteorological inputs from a mesoscale model (WRF) and tied to its horizontal, vertical and temporal resolution. Meteorological parameters, including wind speed and –direction, specific humidity, surface pressure and fluxes of heat and momentum at the surface are provided every 3 hours. Chemical species are updated every time step by using operators for advection, surface emission and dry deposition. Additional vertical diffusion, convection and wet deposition chemistry is also accounted for. An own pre-processor allows the model to use the settings of WRF concerning model grid and settings as input. By that, the MOZART model modifies the chemical reactions by providing chemical boundary conditions to the actual modelling framework of WRF-Chem.

6.3.5 Evaluation

With the settings described above, a control run is conducted by applying the BEP scheme with the chemical and dynamical options displayed in Tab. 5 and Tab. 6. The configuration files ‘namelist.wps’ and ‘namelist.input’ used for executing the chemical simulations are added to the appendix as Figure A.5 and A.6. The WRF-Chem runs are performed on a 382 Tflop SGI based high performance computing system which is located at the NOAA Environmental Security Computing Center (NESCC), Fairmont, West Virginia, which is the location of NOAA's newest High Performance Computing Data Center. An urbanized WRF-Chem run with full online chemistry for one domain with 3 km resolution simulating a 9 day period is executed in about 4 hours computing time when using 240 nodes. The ratio between computational time (wall-time) and real-time accounts for $\frac{1}{54}$. A comparable run with the previously explained setup using the KEA environment would imply a ratio of $\frac{1}{15}$. Considering a spin up time of 2 days, the modelling time period is extended to begin on August 9 0000 h and to end on August 18 2003 0000 h. The evaluation of the WRF-Chem run is executed by comparing the model output for selected variables from the full period at one grid cell (Fig. 27) with the mean of observations within that grid cell.

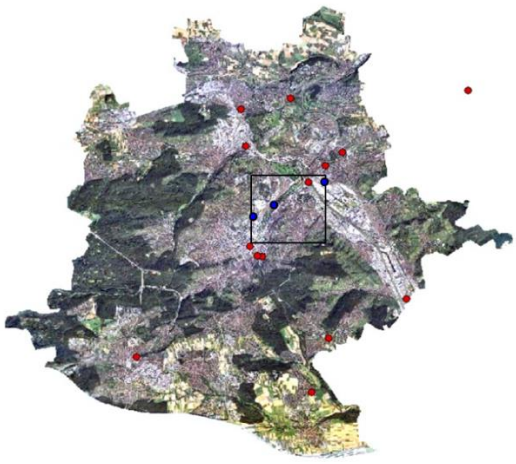

Fig. 27: Urban area of Stuttgart (Source: Google Earth) with meteorological and air quality measurement stations (red dots). The square in the middle indicates the WRF-Chem grid cell of 9 km² used for evaluation of the chemical model runs. For comparison, a mean of 3 stations (blue dots) is calculated.

Tab. 8: Measurement stations used for evaluation of the urbanized WRF-Chem run

Station	Height NN [m]	Measurment Height [m]	Provider
Stuttgart Schwabenzentrum	250	20	Envir. Prot. Agency Stuttgart
Stuttgart Bad Cannstadt - Gnesener Str.	235	3.5	LUBW
Stuttgart Mitte - Arnulf Klett-Platz	245	2.5	LUBW

Each station is located at about the same geographical height, whereas the measurement heights differ by several meters. The average measurement height is calculated to 8.6 m. The first model level however refers to an atmospheric column of ~11 m depth. By averaging over three different heights, the mean concentration of pollutants in the urban canopy is approximated by including observations close to the ground and close to local emission sources, as well as concentrations in the upper canopy layers. The results for the evaluation of 5 compounds (O_3, NO, NO_2, CO and PM_{10}) are illustrated in Fig. 28. Due to the high fluctuation rates of hourly concentration observed within an urban environment, diurnal variations are calculated for both model and measurement as a basis for model evaluation. Modelling results are displayed for the multi-layer approach (Urban) and for a simplified bulk approach (No_Urban).

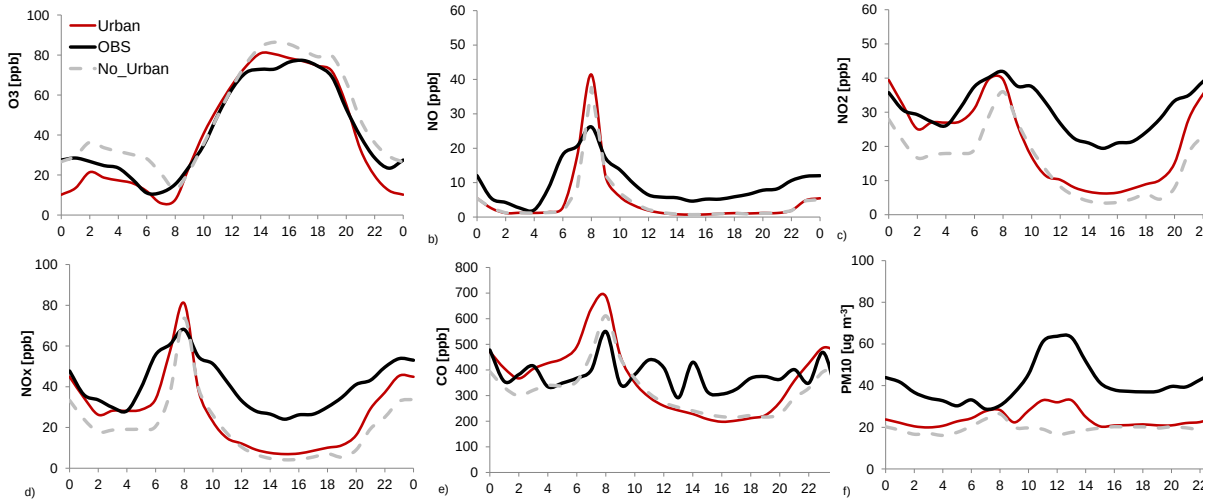

Fig. 28: Average daily trend of modelled concentration at an urban grid cell using the multi-layer approach (red) and the simple bulk approach (grey) in comparison to the mean of equivalent observations from 3 measurement stations located within that pixel (Fig. 27). From left to right: Ozone (a), NO (b), NO_2 (c), NO_x (d), CO (e) and PM_{10} (f).

With regard to Fig. 28, the multi-layer model is able to reproduce the mean concentrations of ozone (40 ppb) as observed throughout the time period and shows a quite good agreement with the diurnal cycle (a). The coefficient of determination for hourly output amounts to 77 %. For NO and NO_2, the morning concentrations can be better reproduced than during the day (b,c). The low daytime values can be caused by an overestimation of photolysis rates or overestimated turbulent mixing near the ground. Low NO values might also be the cause of the slight overestimation of Ozone during the day. The modelled NO_x (d) on average underestimates the observations by 13 ppb (~30 %). With respect to carbon

monoxide (e), WRF-Chem on average underestimates the observations by about 7 ppb (~3 %) and the diurnal variation is smoothed. The peak concentration seen in the observations however are overestimated which can be due to generally higher modelled background concentrations of CO being transported into the domain from boundary conditions retrieved from the global chemistry model MOZART (Chapter 6.3.4). Particulate matter is underestimated by almost 40 %.

When switching off the urban canopy model for the chemistry run and using a simple bulk urban parameterization, the simulated concentrations change in comparison with the observations. The diurnal trends are captured as well when using the bulk approach but mean concentrations tend to underestimate the multi-layer modelled concentrations of NO, NO_2 and PM_{10} and overestimate ozone concentrations.

The effect of an urban canopy in trapping pollutants is simulated better when using a multi-layer canopy model but still the observations cannot be reproduced in their full intensity, even for averaged diurnal variations. The reasons for this can be manifold. On the one hand, schemes in the model representing turbulent exchange or photolysis rates are not configured in the proper manner, so that certain fractions of pollutants are removed. Another problem lies in the selection of the emission inventory which is causing insufficiencies in the modelling result due to coarse resolution. The short modelling period and short spin up time could also be a source of probable errors. However this could not be proven when extending the modelled timeframe by two weeks. The major part of the discrepancy between the model and observations however is ascribed to the fact of comparing the model output for a 3 by 3 km grid cell with one, or at least the average of 3 point measurements. Whereas the model accounts for an average value for an urban grid cell, the measurement stations are predominately located near places with high traffic loads and close to major emitters. This makes it difficult to characterize one single measurement as representative for a larger area and is especially true when studying processes in heterogeneous environments such as urban areas. Although the difference between the multi-layer approach and a simple urban parameterization is smaller than expected, the use of an urban canopy model is mandatory for discussing changes in surface properties based on the effect of urban planning strategies on local air quality.

7. Results

The presentation of the results follows a similar order than the previous Chapter 6.2 and 6.3. First, the dynamical structure of the urban heat island is presented for the modelling area under different aspects, also considering urban rural circulation patterns; second the impact of urban planning scenarios on dynamical patterns is discussed. This structure is maintained when presenting the chemical composition of the urban atmosphere and the impact of reduced temperature on urban air quality. This chapter only shows the results, a detailed discussion follows in Chapter 8.

7.1 Modelling of the Urban Heat Island (UHI) using WRF

The following results are presented for the third model domain (Fig. 20) with 1 km resolution. The multi-layer urban scheme (BEP) is applied. Parameters for the city of Stuttgart are set as explained in Chapter 5. Different tools are used to extract and visualize the model output:

- NCL - NCAR Command Language (UCAR et al. 2013)
- MATLAB
- Microsoft Excel

With the aforementioned settings for the urbanized version of WRF, it is possible to display the urban heat island and the related processes for the urban area of Stuttgart. The characteristics of the urban climate are presented in relation to their rural counterpart to illustrate distinct atmospheric features over urban and rural areas.

Surface plots for potential 2 m air temperature for different times of the day indicate the typical diurnal characteristics of an urban heat island for a Central European city of moderate size, such as Stuttgart, within a period with an extreme weather event. The middle of the lowest model level is located at 5.6 m. By this, potential 2 m temperature has to be integrated downwards, which is done automatically by the model. Fig. 29 shows modelling results for August 13 2003 for the innermost model domain with Stuttgart in the centre. All times refer to GMT +2, daylight saving time for the Central Europe. The lowest model level describes the average value for an atmospheric column of 11 m depth.

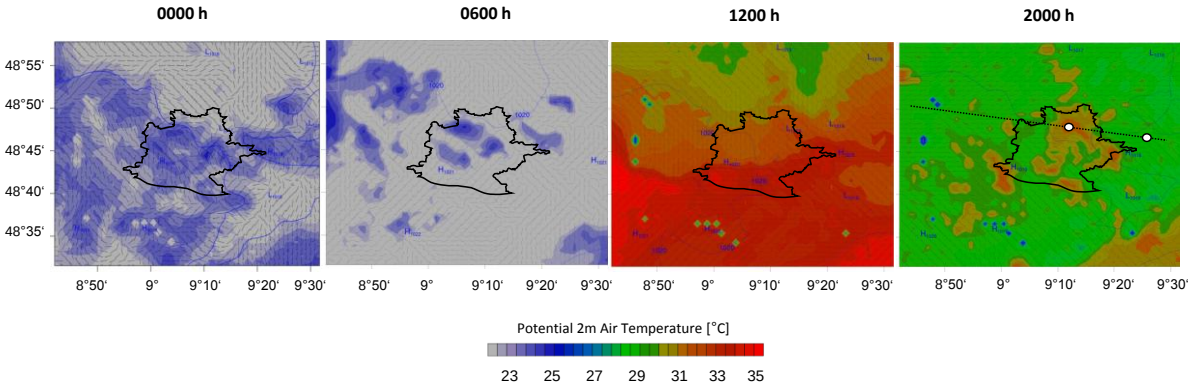

Fig. 29: Potential 2 m air temperature displayed for the innermost domain with Stuttgart in the centre (black outline). Four plots indicate the course of the day (August 13 2003), from left to right showing midnight, morning, solar noon and early evening hours. Light blue lines indicate the surface pressure. Dotted line in the rightmost figure indicates the cross section used for further analysis. White dots indicate the urban and rural grid cell used for the vertical profiles.

The surface plots (Fig. 29) confirm the diurnal warming and cooling cycles of different land surface types. In the night-time, morning and evening hours, the UHI can be clearly identified by higher near surface temperatures due to both heat accumulation in building materials and evaporative cooling of vegetation in the rural vicinity. The difference between averaged urban and averaged rural 2 m potential temperature within the domain accounts for 2.52 °C for evening hours (2000 h) and for 2.6 °C in the early morning hours (0600 h). The potential temperature is chosen to disregard the height dependence of temperature. At noon (1200 h), the difference between urban and rural temperatures is cancelled out by the overall constant high solar radiation in that area. Here, the area west of Stuttgart in the direction to the Rhine Valley shows especially high temperatures and as it accounts for one of the warmest regions in Germany.

Analysing the mean difference of an urban and a rural 1 x 1 km grid cell over the whole modelling period from August 11 to August 17 2003, an average heat island of 1.3 °C is simulated, whereas maximum values can reach up to 4.5 °C (Fig. 30a). As stated by Oke (1982), the largest temperature difference occurs in the night-time and early morning hours as displayed by Fig. 30b, valid for August 12 1200h – August 13 1200h.

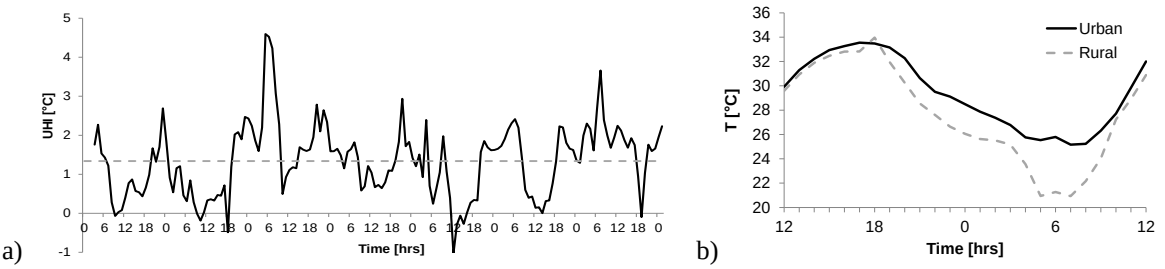

Fig. 30: Urban Heat Island intensity for the modelling period Aug 11-Aug 17 2003 calculated from the differences in 2 m potential temperature for an urban and a rural grid cell (a) and diurnal development of urban and rural temperature for Aug 13 2003 (b)

The urban heat island is pronounced in different layers, ranging from the surface layer to the urban canopy, up to the overlying atmosphere. Accordingly, urban-rural temperature differences are pronounced in skin temperature, temperature within the street canyon and above the canopy.

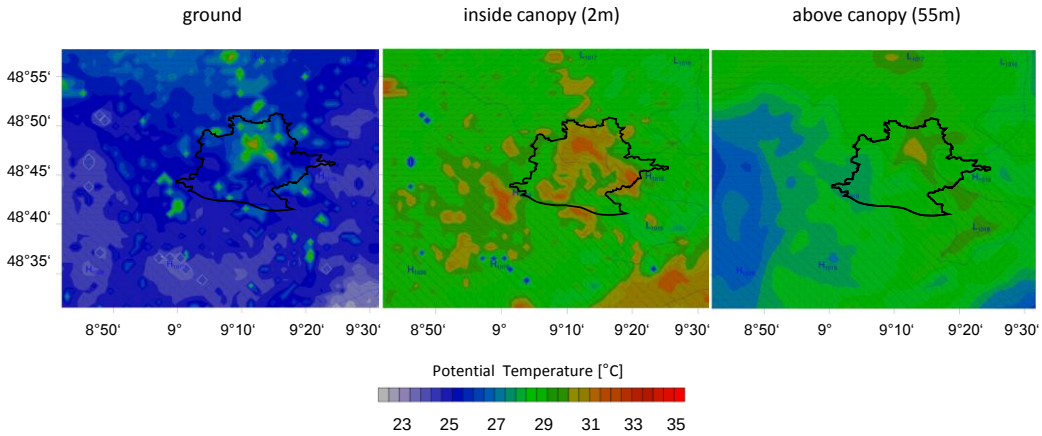

Fig. 31: Surface plots showing skin temperature (left), potential 2 m temperature (middle) and 55 m potential temperature (right) for Aug 13 2003 2000 h

On August 13 2000 h, the urban heat island is well pronounced for three compartments of the urban atmosphere. With regard to the skin temperature (left), the difference between an urban and a rural location amounts to between 4 and 4.5°C, depending on the orientation of the rural grid cell in the eastern or western direction to the city. Taking mean urban and mean rural temperature into account, the UHII amounts to 1.6 °C. In the early evening hours, heat is still accumulated within the urban canopy, whereas natural surfaces in the rural surrounding have already started to cool down. This aspect is mirrored by the near surface temperatures at 2 m (middle) and also by a small amount by the above canopy temperature at 55 m (right), with an UHI intensity of 2.54 °C and 1.8 °C, respectively.

Due to increased buoyancy, the mixing layer height is elevated and excessive heat accumulation within the different layers of the urban atmosphere can result in the formation of an urban plume. Due to advection, the urban plume is elevated to higher levels and can even be recorded in the rural surrounding depending on prevailing weather conditions (Fig. 32).

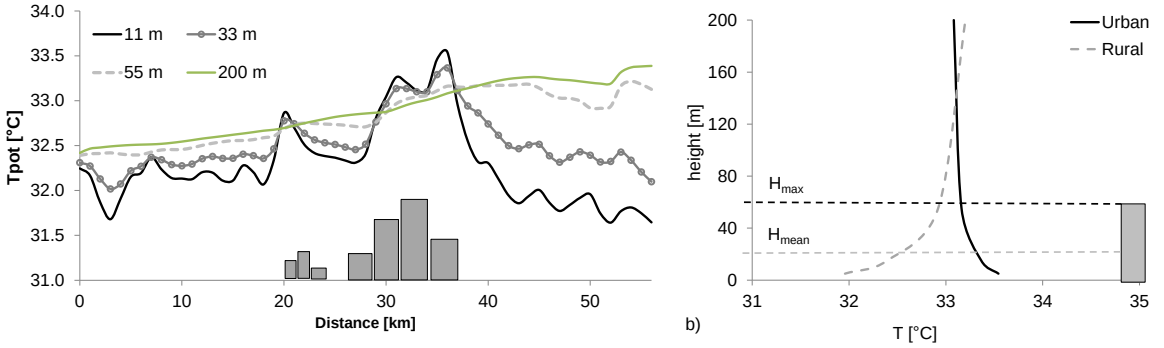

Fig. 32: West-East cross-section (Fig. 29) of temperature in 4 model levels 5m, 15m, 50m and 200m through the centre of the urban area of Stuttgart following the prevailing wind direction (west). Vertical profile of potential temperature over an urban and a rural grid cell (Fig. 29) is shown on the right (b)

Fig. 32 shows a horizontal west-east cross section of potential temperature following the main wind direction. Four model levels are illustrated to account for vertical temperature differences. Modelling results are presented for 2000 h local time. The actual wind speed is modelled with 2 ms^{-1} for the lowest level, 3 ms^{-1} at 15 m, 4.5 ms^{-1} at 50 m and 5.2 ms^{-1} at 200m. The horizontal distance amounts to 60 km.

With regard to the lowest model level, the difference between urban and rural areas is well pronounced for both directions upwind and downwind. Upwind temperatures are elevated compared with their downwind counterparts, because of the presence of single smaller urban agglomerations. Here, the temperature slightly increases with height, whereas in the urban atmosphere a decrease with height can be observed. Surface warming increases the potential for vertical motions of air masses which leads to a de-stabilisation of the atmosphere above. This effect is proven by a negative temperature gradient within the first 200 m. The positive flux of sensible heat from the urban surface is the source for buoyancy and the driver of the secondary circulation system between the urban and rural environment.

The shape of the temperature profile changes significantly when looking at the downwind side of the city. A distinct increase with height can be observed with a difference of almost

2 °C between the lowest and highest (200 m) level. Due to elevated temperatures over the city, an urban plume can emerge which can be transported to the rural surrounding in the city's vicinity. According to Figure 32, this can particularly be observed above a height of 50 m. On the contrary, evaporative cooling of the rural surface leads to a surface urban heat island intensity of almost 2 °C when comparing an urban grid cell at about 40 km with a rural grid cell located at around 55 km horizontal distance. The vertical profiles of the potential temperature for an urban and a rural grid cell (Fig. 32b) well indicate the degree of atmospheric stability for both cases.

In general, during the day and evening hours a convective boundary layer evolves, in night-time, the boundary layer is stably stratified (Roedel 1992). These effects differ between urban and rural environments and can be shown by modelled temperature and wind profiles. The following plots basically concentrate on the first 2000 m and take a closer look at the lowest 100 m, resolving the urban canopy layer height as limited by the height of the highest buildings (35 m). As the potential temperature is considered here, the degree of atmospheric stability can be derived from the curve's deviation from the adiabatic temperature gradient (displayed in green in Fig. 33 d,f).

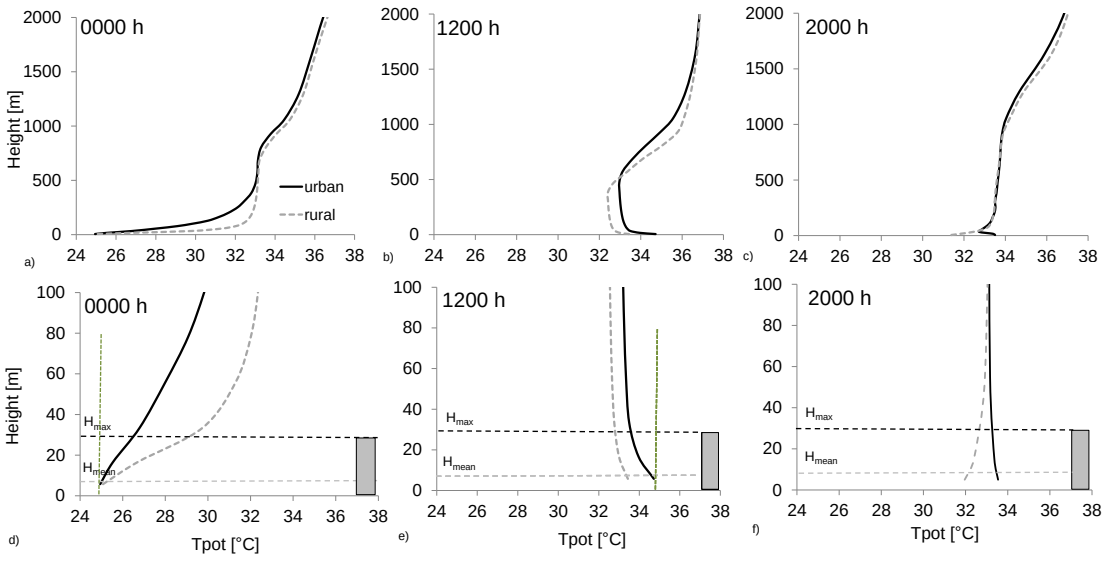

Fig. 33: Vertical profiles of potential air temperature for an urban and a rural location (grid cell) on August 13 2003 at 0000 h, 1200 h and 2000 h – displayed are the first 2000 m (upper plots) and a closer look at the first 100 m (lower plots). The dotted lines in the lower plots indicate the maximum and mean building height of around 35 m and 8 m, respectively. The green line stands for the adiabatic temperature decrease.

At midnight (a,d), the temperature gradient is positive which leads to stable conditions and to a temperature inversion most obvious in the first 300 m. Especially within the bottom

layers, there is a high degree of stability, whereas this effect is more pronounced for the rural case, because heat accumulated within the urban canopy results in a residual of sensible heat flux at night. Following the considerations of Stull (1988) presented in Fig. 7, a stable nocturnal boundary layer forms within the lowest 500 m of the atmosphere. At noon (b), the temperature curves show a negative gradient, which reflects a higher degree of instability in the urban atmosphere. The negative temperature gradient continues up to a height of 500 m for the rural and 600 m for the urban location before turning positive. This turning point and the characteristic c-shape of the profile reflect the depth of the daytime convective boundary layer CBL (Fig. 7). In the evening hours the urban and the rural curves show opposed characteristics in the first 100 metres (f), which can be attributed to the overwarming of the urban canopy which leads to a destabilization of the overlying air. On the contrary, a temperature increase can be found for the rural case. The simulated boundary layer height at 1200 m (urban) and 600 m (rural) is hard to discriminate from figure 34 f.

The horizontal wind speed reflects the thermal conditions, whereas an increase with height within the first 100 m is simulated for different times of the day (Fig. 34).

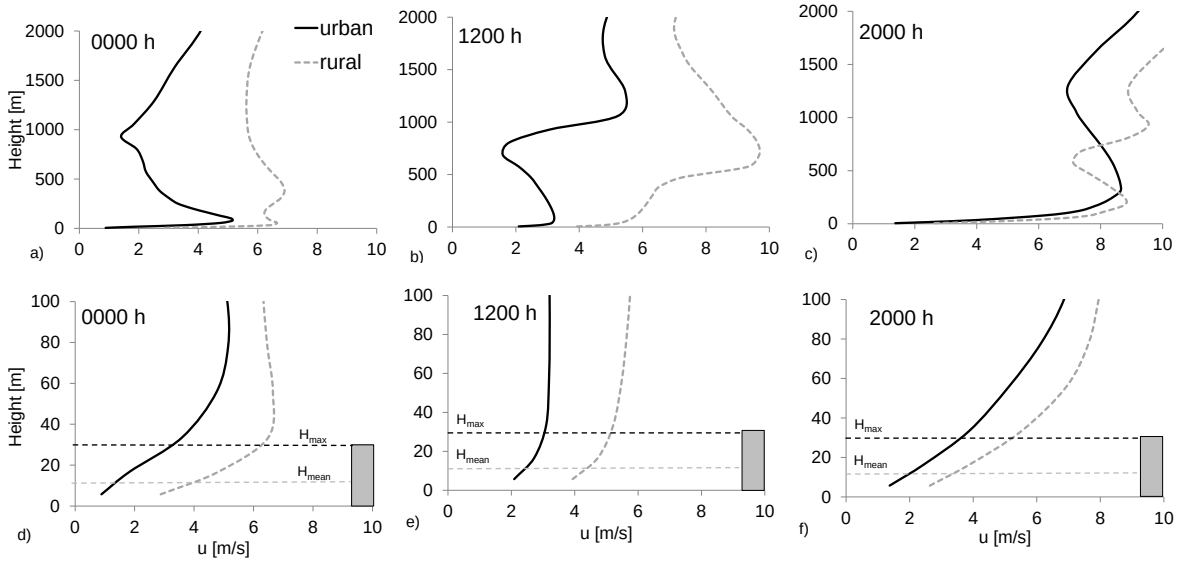

Fig. 34: Vertical profile of horizontal wind speed for the first 2000 m (upper plots) and the first 100 m (lower plots) for the rural (dashed) and the urban (black) grid cell presented in Fig. 29. Maximum (black dashed line) and mean building height (grey dashed line) are added to the plot. Plots are generated for Aug 13 2003 0000 h, 1200 h and 2000 h

In general, urban wind speed is reduced compared with the rural location. Within the lowest model level, both curves differ by about 2 m s^{-1}. The vertical wind shear is proportional to the surface roughness which leads to a significant decrease of wind speed within the urban canopy. At noon, the rapid increase of horizontal wind speed at 600 m (urban) and 500 m (rural) might represent the location of the PBLH for both cases. Same is valid for the evening cases where a significant increase of wind speed at 1200 m (urban) and 600 m (rural) may represent the vertical extend of the boundary layer.

Excessive warming of impervious surfaces during the day foster convective processes, which can be distinguished by vertical motion of air over a west-east cross section (Fig. 35). The contour lines of equal vertical wind speeds (isotachs) indicate upwards directed vertical motions. The main focus is being put at the first 1200 m, where the atmosphere is significantly affected by the presence of the city. The chosen time in Figure 35 is 2000h on August 13 2003. The black pattern indicates the topography over the cross-section.

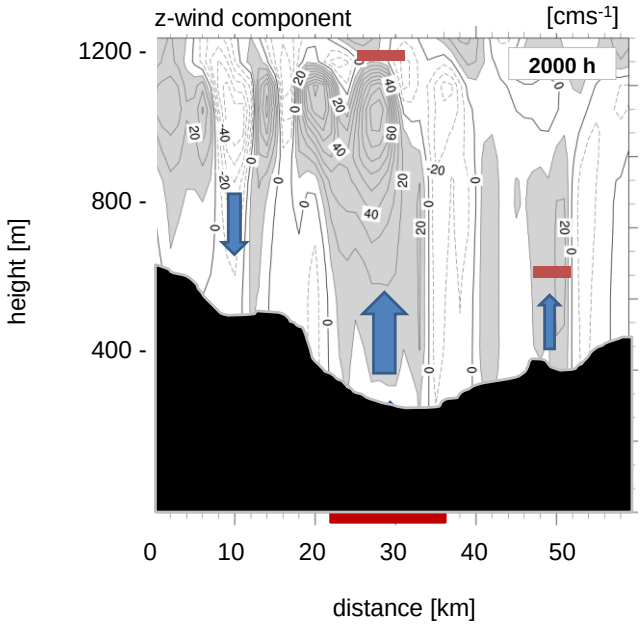

Fig. 35: Horizontal cross section of the wind component in vertical direction through the city centre of Stuttgart (red bar). Positive values (grey shading) indicate uplift. White shading indicates negative (downdraft) or zero values. Results are displayed for Aug 13 2003 2000 h As vertical wind speeds show considerably low values, they are presented in cm s^{-1} here. The red bars indicate the simulated height of the PBLH, the black shading represents the topography

At 2000 h vertical wind speeds reach up to 40-60 cm s^{-1}, reaching up to a height of about 1200 m, above the city (illustrated by the red bar on the bottom). Positive values indicate

upward directed fluxes due to an excessive warming of the urban surface during the day. The intensity of the positive fluxes is partly compensated by negative fluxes in the cities vicinity (left). Further the vertical velocities follow the shape of the topography, leading to downward directed fluxes upwind (left) and upward motion downwind of the city (right) with regard to the prevailing wind direction from west to east. According to model output at 2000 h, the PBLH (red bars) is located at around 1200 m for the urban and 600 m for the rural locations. As indicated by Fig. 35, vertical fluxes due to topography and due to an overwarming of the urban surface are overlapping. If the city were located in an even topography the urban induced vertical uplift would even be more pronounced.

The complex nature of the topography has an effect on the diurnal characteristics of the wind direction. For the whole modelling period, the ‘mean’ wind is coming from north-westerly directions. When separating both day and night situations, a diurnal change of wind direction can be observed mainly in the complex terrain attached to the west, south and east of the urban area.

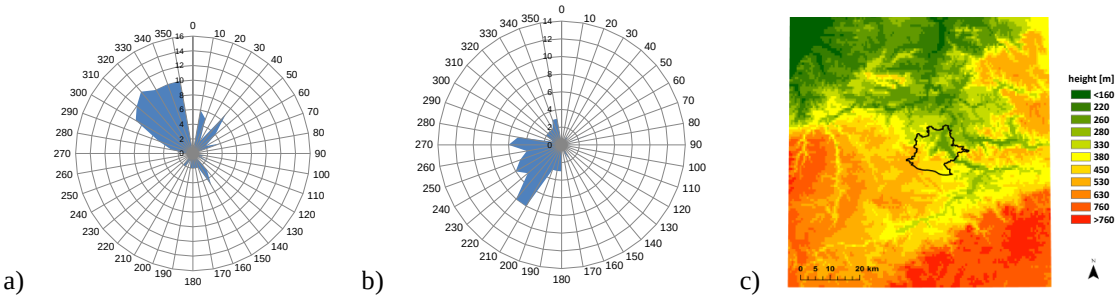

Fig. 36: Mean wind directions at canopy height (33 m) in the city centre averaged over the modelling period presented for daytime (a) and night-time (b) situations. The topography is displayed on the right (c).

In complex terrain, wind can change direction during the course of the day (b). The surface of the slopes and the overlying air cools down. By this the air gets denser and heavier, which leads to a subsidence of large parcels of air following the gradient of the slope. For Stuttgart, this effect is more pronounced in the south western rural surrounding where height differences to the city centre reach 200 m or more. The prevailing topography (c) thus generates a diurnal change in wind direction from north-west to south-west when averaging over the modelling period (Fig. 36).

Referring to Chapter 3, the surface energy balance is mostly driven by the partitioning of latent and sensible heat due to irradiative properties. Impervious surfaces and urban

canopies tend to absorb a major part of the incoming solar radiation, resulting in a massive release of sensible heat. In combination with human activities, the amount of heat release is increased even more. On the contrary, vegetative surfaces are able to transform a certain amount of radiation to latent heat via photosynthesis and changes of state without increasing in temperature which can even promote a net cooling effect. The Bowen ratio, B (the ratio between sensible and latent heat) is an indicator for quantifying the heat gained or lost in a substance. When the magnitude of B is greater than 1, a greater proportion of the available energy at the surface is passed to the atmosphere. The converse is true for values less than 1. The daily course of latent and sensible heat flux for an urban and a rural grid cell as indicated in Fig. 29 is shown by Fig. 37

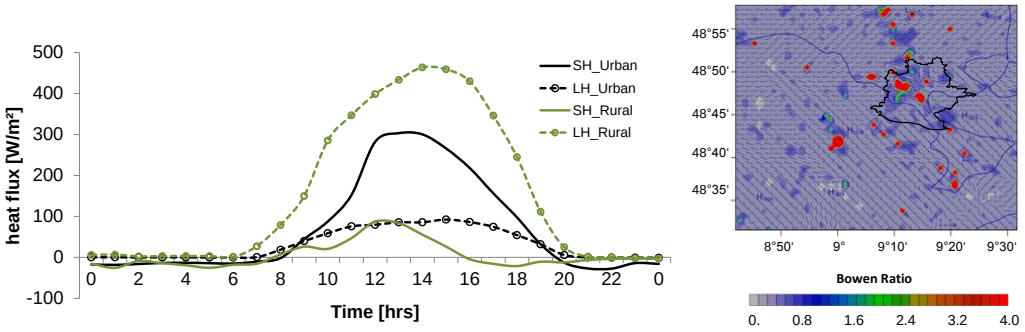

Fig. 37: Diurnal course of latent (LH) and sensible (SH) heat flux from an urban and a rural location (left) and Bowen ratio calculated from SH/LH presented for the model domain at 6 pm. Both plots present results for Aug 13 2003

The urban heat island is also pronounced in the soil and in deeper layers under the ground due to a significant amount of heat flux into the ground. Simulations show, that this amount accounts for 20 % (111 Wm^{-2}) of the average total incoming solar radiation with regard to the modelling period. This can negatively affect the quality of soil and even ground water and plays a significant role in the energy balance of an urban environment. In this study, the main focus is being put on atmospheric effects. For this reason, ground fluxes are not discussed in detail.

The following table summarizes the most important effects of the urban heat island on meteorological conditions, based on the comparison between model output for an urban and a rural grid cell.

Tab. 9 Important meteorological features of urban and rural environments, presented as an average for the modelling period Aug 11 to Aug 17 2003

	TSK [°C]	TH2[°C]	Q10 [%]	PBLH [m]	TKE10 [m²/s²]	SH [W/m²]	LH [W/m²]	U10 [m/s]
Urban	27.02	25.56	51.10	709.07	0.34	90.27	29.33	0.80
Rural	23.30	24.46	54.70	340.88	0.20	28.00	138.12	1.30

Referring to Tab. 9, average urban heat island intensities can be calculated for the modelling time period. Surface UHI calculated from ground temperature (TSK) accounts for 3.72 °C and for 1.1 °C when taking the 2 m potential temperature as a reference. The relative humidity is increased in rural environments by a small amount. Differences in atmospheric dynamics can be well documented by vertical mixing intensities represented by the turbulent kinetic energy (TKE). On average, the TKE is reduced by almost 50 % for the rural compared with the urban location. Due to increased buoyancy, the planetary boundary layer is elevated above the city. As being defined as the height where the TKE drops below 0.01 $m^{-2}s^{-2}$, the PBLH is directly calculated from the TKE (Hu, Nielsen-Gammon, & Zhang 2010). The wind speed differs by 0.5 m s^{-1} on average and the Bowen ratio differs by a great amount, showing a mean value of 3.2 for the urban and 0.2 for the rural grid cell.

7.2 Air Quality modelling with WRF-Chem

7.2.1 Chemical features of the urban atmosphere

Tab. 10 shows the mean concentration of NO, NO_2, CO, PM_{10} and O_3 for a modelled grid cell in the urban centre (Fig. 27), averaged over the time period (Aug 9 – Aug 17 2003). VOCs are added to the list represented by formaldehyde (HCHO) and isoprene (C_5H_8) is used as representative of biogenic compounds. In addition, results for daytime (0700 h – 2200 h) and night-time (2300 h – 0600 h) are separated. The same is shown for a rural grid cell classified as ‘mixed forest’. It is located at a distance of 120 km north east of the city at the same height above sea level and beyond the area of influence of other urban agglomerations.

Tab. 10 Atmospheric composition of urban and rural air, explained on the basis of selected primary and secondary compounds. Values represent mean urban and mean rural concentrations for the modelling period August 9 to August 17 2003 on a single urban and rural grid cell. The day (0700 h – 2200) is distinguished from the night (2300 h to 0600 h).

		NO [ppb]	NO2 [ppb]	PM10 [µg/m³]	CO [ppb]	O3 [ppb]	HCHO[ppb]	ISO[ppb]
Urban	**mean**	4.71	20.62	21.84	345.74	40.05	5.48	1.03
	Day	6.13	14.49	21.30	291.98	54.92	4.91	1.44
	Night	2.34	30.84	21.64	432.30	15.27	6.43	0.33
Rural	**mean**	0.21	3.22	15.20	175.24	45.67	3.78	2.54

Due to traffic emissions, mean concentrations of nitrate oxide (NO) are significantly higher in urban areas than in a forested rural area, at remote distance from the city. Ambient ozone concentrations can be equal or even higher in rural surroundings because the NO compounds responsible for ozone destruction are missing. Another cause can be the increased emission of biogenic compounds (Isoprene C_5H_8) which can also act as a precursor to ozone formation. Due to the elevated rural ozone, small concentrations of NO_2 can be found as well. The amount of CO indicated in the rural air can be explained by generally high atmospheric background concentrations. Due to a long life time, CO can be transported over long distances and slowly forms to CO_2. Further, it can act as a precursor to natural background O_3. VOCs like formaldehyde can also be recorded in the rural air. Common sources are the metabolism of mammals, photo-oxidation in the atmosphere and emissions from wood (Guerreiro, de Leeuw, & Foltescu 2013). The modelled amount of aerosols for the rural case is about 35 % less than for the urban grid cell.

NO, NO_2 and ozone are coupled via photochemical reactions (Chapter 4.1 and Fig. 38), with solar radiation being the key driver for Ozone production. Concentrations therefore are significantly higher during the daytime. The sum of NO_2 + NO (NO_x) can be seen as a catalyst for ozone formation, being responsible for the ozone production efficiency (Seinfeld & Pandis 2012). The concentration of NO is coupled to daily emissions by combustion processes connected mostly with car exhaust. The emission peaks are located at the beginning (0800 h) and end (1800 h) of the working day, which results in modelled concentrations being comparatively higher during the day than at night. With regard to NO_2, this effect is reversed with higher values found at night. The concentrations of NO_2 however can be attributed to primary and secondary effects. The first is related to direct emissions from local traffic, whereas the latter is linked to chemical reactions, where NO_2 is oxidized from locally produced NO and ozone from the urban background. On average,

the ratio between NO and NO_2 contributing to mean NO_x emissions (40 ppb) amounts to 2 ppb (NO) and 38 ppb (NO_2).

Over the course of the day, NO_x is depleted at the expense of ozone, which is formed by oxidation of NO_2 in the presence of sunlight. NO can be further removed from the atmosphere through vertical mixing and deposition or by gas phase reaction with OH radicals, which are produced by photolysis of nitrous acid (HONO), VOCs (e.g. HCHO) or O_3. In the night-time and morning hours, ozone is titrated by NO to form NO_2. When reacting with ozone, NO_2 can be depleted to form the nitrate radical NO_3. The latter again can react with available NO_2 to form dinitrogen pentoxide N_2O_5. Fig. 38 shows the daily trend of NO_2, NO and ozone simulated for August 13 2003.

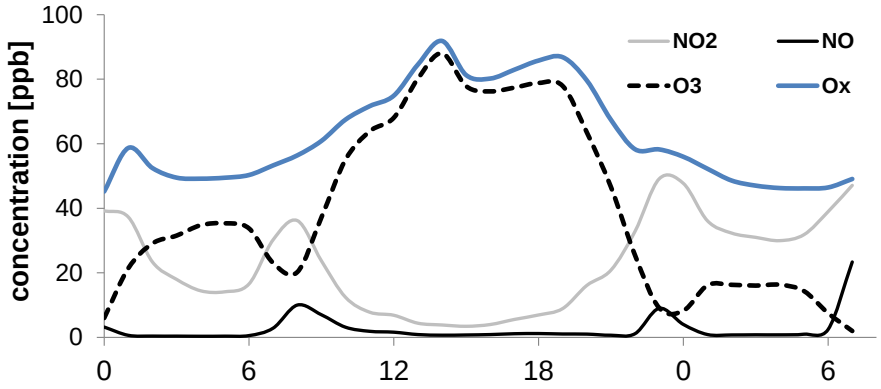

Fig. 38: Diurnal trend of near surface concentrations of NO, NO_2 and Ozone for an urban grid cell for a selected day (August 13 0000 h – August 14 0600 h)

The high morning concentrations of NO_2 originate from the low rates of depletion during the night-time due to the lack of photolysis reactions. The NO concentrations do not differ significantly between day and night, because emitted NO in the morning is removed by atmospheric mixing during the day and by reaction with freshly formed ozone. In the evening concentration of NO is attributed to traffic emission again. The blue line in Fig. 38 indicates the oxidant Ox, (sum of NO_2 and O_3) which is often used to describe the oxidizing potential of the atmosphere. It serves as an appropriate indicator of photochemical ozone production, because it approximates the total oxidant concentration without being affected by reactions between NO and ozone via the O_3 pathway (reaction 4.7) (Tang et al. 2009).

The relation between NO and NO_2 with ozone concentrations is illustrated by the figure below, indicating a decrease of O_3 with both increasing NO and NO_2 concentrations.

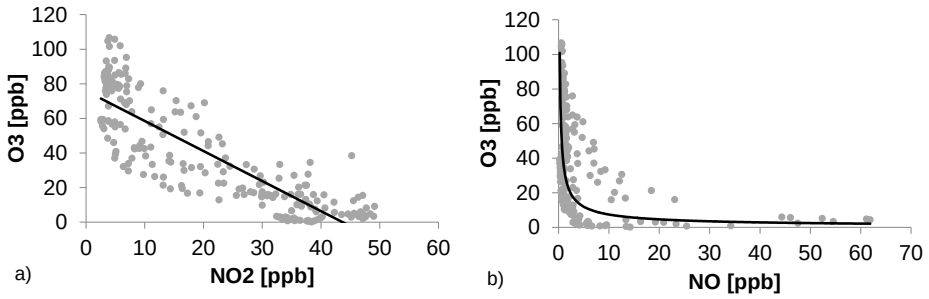

Fig. 39: Correlation between near surface concentrations of NO_2 and ozone (a) and NO and ozone (b) for hourly model output of the modelling period (Aug 09 - Aug 17 2003).

Ozone and nitrogen dioxide show a negative linear relationship with a coefficient of determination of about 0.73. In the case of NO, ozone decreases exponentially with an increase of NO.

However, these effects do not fully explain the elevated ozone concentrations between 0000 h and 0600 h and the significant increase in the morning hours, as depicted in Fig. 38. Next to photochemical reactions, another reason for rising ozone levels is the mixing into the boundary layer by downward transport from higher layers or the horizontal advection from surrounding rural areas (Seinfeld et al. 2012). This effect can be documented by vertical and horizontal profiles extracted from WRF-Chem model output Fig. 40.

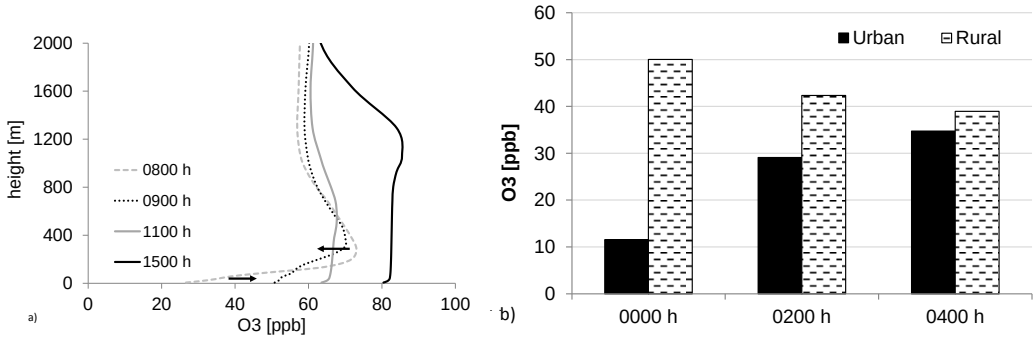

Fig. 40: Vertical profile of ozone concentrations (a) for the same urban grid cell than analysed in Fig. 38 at four different times of the day (Aug 13 2003). Horizontal arrows indicate the direction of the shift in ozone concentration. O_3 concentrations for three different times during the night for an urban and a rural location upwind of the city (b).

The vertical transport of ozone from higher layers is documented by Fig. 40a. Between 0800 h and 1100 h, the profile illustrates an increase of surface O_3 levels at the cost of a decrease in higher levels (indicated by the black arrows). The daily peak of ozone concentration is reached at about 1500 h. Fig. 40b indicates the horizontal advection of ozone from the rural surroundings as the wind direction changes in the course of the day (Fig. 36). Between 0000 h and 0400 h no net production of ozone occurs and the major

part has already been removed by evening emissions of NO. By this, the increase of surface levels of ozone can potentially be explained by the inflow from neighbouring areas, which itself encounter a decrease respectively.

Concentrations of aerosols (PM_{10}) can be slightly elevated at night. Cooler air temperatures lead to a reduction of buoyancy, air mixing and a subsidence of the boundary layer. By this, atmospheric stability is increased, which leads to a net increase of concentrations.

In general, these assumptions are also true for carbon monoxide, whereas a certain amount of daily CO concentrations can be reduced by the presence of hydroxyl-radicals (OH) which form from water and ozone by the impact of ultraviolet radiation.

Primary pollutants are emitted directly, which leads to concentrations being highest within the urban canopy and decreasing quickly with height. Secondary pollutants like ozone show different characteristics. The following graph (Fig. 41) shows vertical profiles of CO, NO_x and O_3.

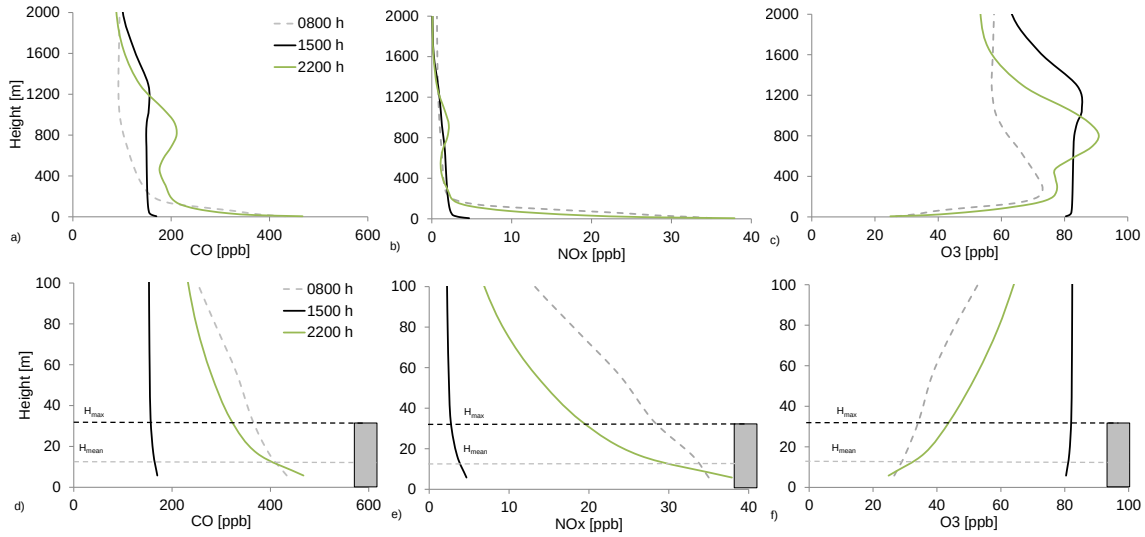

Fig. 41: Vertical profiles of urban CO NO_x and O_3 retrieved from WRF-Chem model output for August 13 2003 and three points in time (0800 h, 1500 h, and 2200 h). For each compound, an atmospheric column of 2000 m (a-c) and 100 m (d-f) is displayed for a central urban grid cell

In the morning and evening hours, near-surface concentrations of CO and NO_x are increased due to enhanced traffic and human activity. Strong negative gradients within the urban canopy show a decrease of 200 ppb for CO and 20 ppb for NO_x respectively within the first 35 m. Due to a decrease in emissions during the day as well as a removal of NO and NO_2 via photochemical reactions, concentrations decrease. In contrast, ozone is

formed when nitrate oxide, carbon monoxide and VOCs react in the atmosphere in the presence of sunlight. As explained earlier, they act as precursors for ozone formation. The daytime concentrations of CO are still almost 200 ppb because of generally high background concentrations. During daytime, concentrations for all three compounds remain constant over the vertical column. At 1500 h, ozone is significantly increased at the cost of NO_x and CO. O_3 reaches a maximum at the time other compounds reach a minimum in concentration, until the emission of primary pollutants starts over again in the evening and ozone again is removed when oxidizing with NO to form NO_2.

7.2.2 Urban-rural circulation patterns

Enhanced urban temperatures lead to increased vertical mixing (Fig. 35). Urban heat island formation and meteorological conditions enhance urban rural circulation patterns with primary pollutants of urban origin being transported into the rural surrounding over the course of a day. Fig. 43 shows the modelled concentrations for three vertical levels (5, 33, 55 m) and three locations (urban, rural northwest (NW) and rural southeast (SE)), with values representing the average concentration for the whole modelling period. Both rural locations represent grid cells at a distance of about 20 km from the urban centre in each direction. In average wind direction is northwest with a mean modelled wind speed of 2.3 m s^{-1}. A distribution of daily wind directions as well as the location of the three grid cells used for further executions are displayed in the figure below.

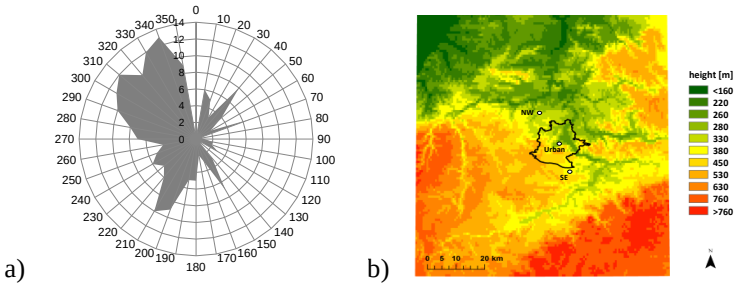

Fig. 42: Distribution of all modelled wind directions in a height of 10 m of hourly WRF-Chem output with regard to the modelling period Aug 09 - Aug 17 2003 (a) and topographical map (WRF output) of the modelling area with location of the grid cells (white dots) used for the illustration of urban-rural circulation patterns (b)

Different than expected, mean concentrations of selected compounds (CO, NO_x and PM_{10}) are higher in the upwind (NW) compared with the downwind (SE) location when considering the mean wind direction, and is most pronounced for the lowest model level.

The strongest effect is to be observed with regard to NO_x, while the effect for ozone is reversed with higher concentrations simulated for the rural grid cells (Fig. 43).

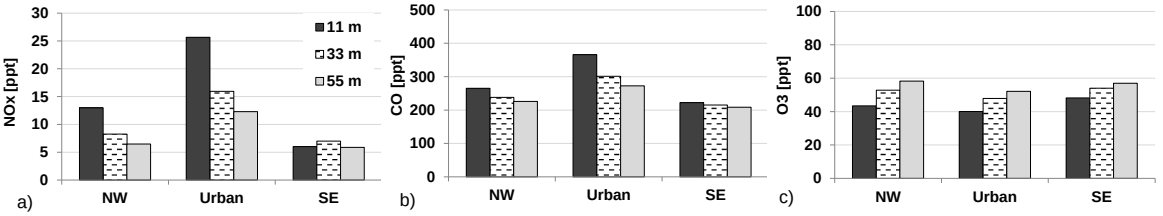

Fig. 43: Concentration of NOx, CO and O_3 averaged over the time period Aug 09-Aug 17 2003. 3 vertical levels (10m, 33m and 55m) are displayed for an urban location (Urban) and two rural locations - one upwind (NW) and the other one downwind (SE), both with a distance of about 20 km to the urban centre. Values are retrieved from the WRF-Chem 'Control Run'. Locations of grid cells are shown in Fig. 42b.

In general, the largest difference between urban and rural locations with regard to primary pollutants is simulated for the near surface layer (black bar). Because traffic is considered to be the main source of primary pollutants, the lowest level represents the height which is close to the pollution sources. At greater heights, concentrations of primary pollutants decrease rapidly, in particular when crossing the upper level of the urban canopy (Fig. 41). This assumption however is not true for ozone concentrations which increase with height, partly attributable to the height dependent decrease of NO_x. Both compounds are negatively correlated according to Fig. 39. The average concentrations simulated for the north western part are imbalanced compared with the south eastern rural counterpart with a surplus of 6 ppb (NO_x) and 43 ppb (CO), accounting for a relative increase of 100 % (NO_x) and 20 % (CO) for the NW compared with the SE direction.

Fig. 43 represents an average for the whole time period. As already indicated in Chapter 7.1 (Fig. 36), the mean daily wind direction is reversed over the course of the day. By this it is necessary to separate day time and night-time conditions (Fig. 44). Only near surface concentrations are to be discussed here, showing the largest effects for all three variables

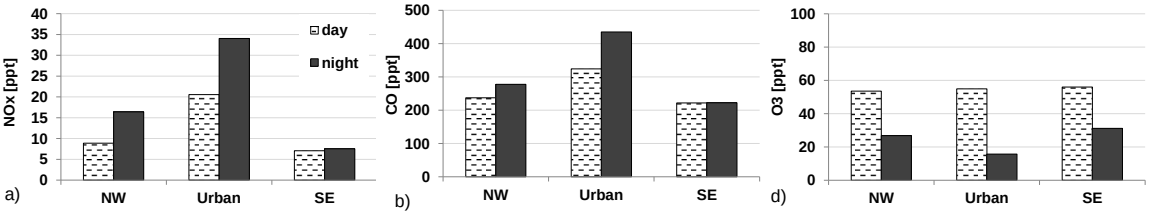

Fig. 44: Night and daytime concentrations of NOx, CO and ozone (O3) averaged over the time period Aug 09 - Aug 17 2003 for an urban location and two rural locations - one northwest (NW) and the other one southeast (SE), both with a distance of about 20 km to the urban grid cell (Fig. 42). Values are retrieved from the WRF-Chem 'Control Run' with daily mean calculated based on the time frame 0700 h – 2200 h. Night-time values represent the time frame 2300 h – 0600 h local time.

The separation of day and night time conditions reveals significant features with regard to the transport of pollutants. Here, the main part of increased rural concentrations falls upon the north-western part due to a change in wind direction over the course of the night.

a) Night

Due to a higher degree of atmospheric stability over the urban area at night, the air mixing is decreased thus leading to comparatively higher concentrations of CO and PM_x. The large difference in nitrate oxide concentration in a night time urban environment is caused additionally by the lack of sunlight hampering the transformation of NO_2 to O_3 via photochemical reactions. Ozone values are comparatively lower at the urban than at the rural location. Differences between the rural locations are only marginal. Night-time concentrations of NO_x, CO and PM_x are elevated at the north western part. The urban area of Stuttgart is embedded into a complex terrain surrounded by moderately sized hills in three directions. The only opening of the valley is in the north-northwest, which is also the common wind direction. At night, the rural surrounding starts to cool down, happening faster at the elevated regions to the south east. During the process of cooling, the air becomes denser and heavier and starts to descend along the direction of the slope, generating wind. This process is able to reverse the general wind direction and to transport urban pollutants into the rural surrounding, previously located upwind. Wind directions for the three cases are displayed in Fig. 36. The average wind speed is modelled with 2.3 m s^{-1}. Considering night time conditions, the effect of inverted wind direction results in an increase of 118 % for NO_x, 25 % for CO and 12 % for PM_x downwind, compared with upwind. When setting the upwind location as the ‘undisturbed’ base case, the concentration surplus found downwind could be attributed to an external source - the city. In other words, 54 % of NO_x, 20 % of CO and 10 % of PM_x which are recorded 20 km downwind of the city, is assumed to have urban origin. During night-time, the urban heat island intensity is slightly elevated when comparing the mean urban with the mean rural temperature found for the grid cell in the north-western direction. This aspect might promote the differences in concentrations as well.

b) Day

During the day, the situation gets more complex due to enhanced atmospheric turbulence caused by excessive warming of the surface. The prevailing wind is blowing from north westerly directions. This situation would be expected to increase the concentrations in the south-east part (downwind) of the city, but this is not the case. Upwind and downwind concentrations differ only marginally during the day. Model results document the urban heat island being equally pronounced for both cardinal directions.

7.3 Effect of urban planning scenarios on UHI and chemical composition

This chapter discusses the various effects of urban planning strategies on the urban heat island intensity and further on the chemical composition of the urban atmosphere. Scenarios treat white roofs and walls (‘Albedo’), urban greening (‘Central Park’ and ‘Many Parks’) and decreased building density (‘Density’) as explained in Chapter 6.4.4.

7.3.1 WRF: Effect of urban design on UHI

The following results are based on the data and methods explained in Chapter 6.2.

The effectiveness of the single strategy to reduce urban temperatures and the UHI intensity can be discussed by comparing near surface temperatures retrieved from the control run representing ‘real’ conditions (Control) and the respective scenario run. Other aspects include the vertical temperature distribution, dynamical properties of the atmosphere and effects on the energetic state. The following figure shows the potential 2 m temperature for the control run (Fig. 45 a) and 4 different scenarios (Fig. 45 b-e) for the area of Stuttgart, with regard to Aug 13 2003 2000 h. In order to smooth the patterns, the graphics show a nearest neighbour interpolated temperature field. Interpolation leads to a reduction of grid spacing from 1 km to 50 m.

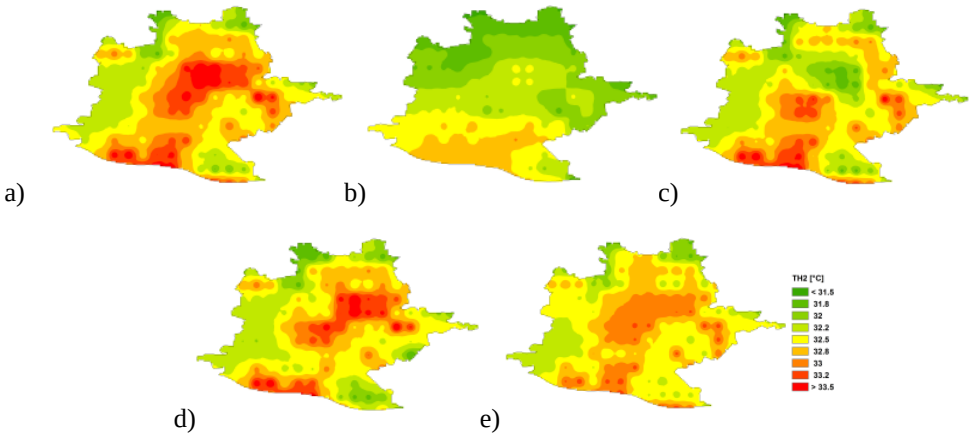

Fig. 45: 2 m potential air temperature for the urban area of Stuttgart extracted from model output for Aug 13 2003 2000 h with regard to the 4 scenarios explained in Chapter 6.2. Nearest neighbour interpolated temperature fields are presented for the control run (a), changed albedo (b), inclusion of a central park (c) and many smaller parks (d) and changed building density (e)

The sensitivity of the different strategies to potential temperature in the urban canopy can be discussed by visually comparing the temperature patterns in Fig. 45. For the 'Albedo' scenario (b), a temperature decrease over the entire urban area can be observed and the patterns disappear compared with the control run (a). Concerning the two urban greening scenarios, the effect of the single central park can clearly be distinguished by the green pattern in the city centre (c) whereas the 'Many Parks' scenario (e) shows a general reduction of the red and orange shaded areas and a changing in the pattern wherever the land use is modified. For the density case (d), the general pattern remains unchanged compared with (a), but with an observed temperature decrease of 0.5 to 0.8 °C.

Probability density functions (PDF's) are retrieved for hourly temperature output over the whole modelling period for a grid cell located within the urban centre, where the curve shape indicates the effect of the scenario. As only one grid cell is taken into account, the urban greening scenario 'Central Park' is used here. In the following, it is specified as 'Park'.

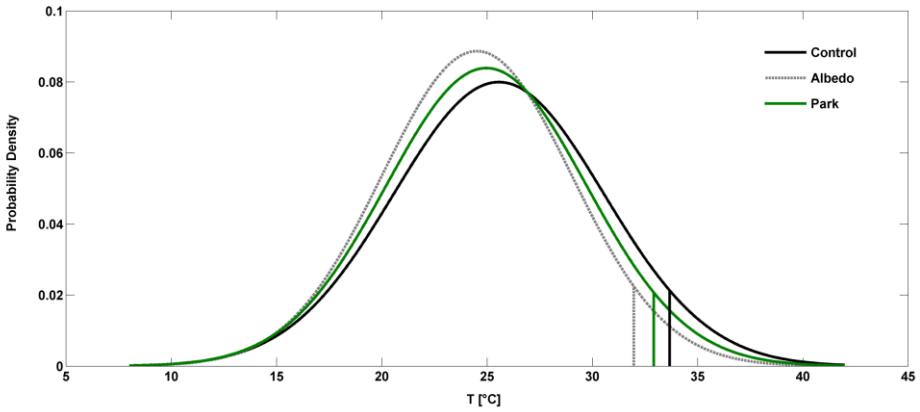

Fig. 46: Probability density curves (left) showing hourly modelled 2 m potential temperature for the whole modelling period and three scenarios with regard to an urban grid cell. Vertical lines indicate locations of the 95th percentile.

The efficiency of a strategy to reduce urban temperature can be analysed by comparing the location of the 95th percentile. This shift accounts for 1.7 °C for the 'Albedo' and 0.8 °C for the 'Park' scenario. No effect is to be observed for the 'Density' case. Additionally, significant changes are simulated for maximum temperatures, with a 2.7 and 2.3 °C reduction concerning white roofs (Albedo) and urban greening (Park), respectively and about 1 °C with regard to decreased building densities (Density). The location of the temperature mean indicates a shift of about 1 °C in the direction to cooler temperatures. In general, the probability density distribution is flattened and shifted towards smaller temperatures.

The spatial effect of each scenario to reduce the urban heat island intensity can be calculated by the difference between modelled temperatures for scenario and control runs with regard to a 25 by 20 km extract of the innermost model domain (Fig. 47). The city of Stuttgart is located in the centre and accounts for about 40 % of the total area. Fig. 47 illustrates the difference in 2m potential temperature (Θ) for each urban planning strategy. August 13 2003 2000 h is used as an example. Urban heat island intensities are calculated from the average urban temperature (defined by the city borders) and the average temperature of the surrounding area. NCL uses a nearest neighbour interpolation method to smooth the patterns of the temperature field.

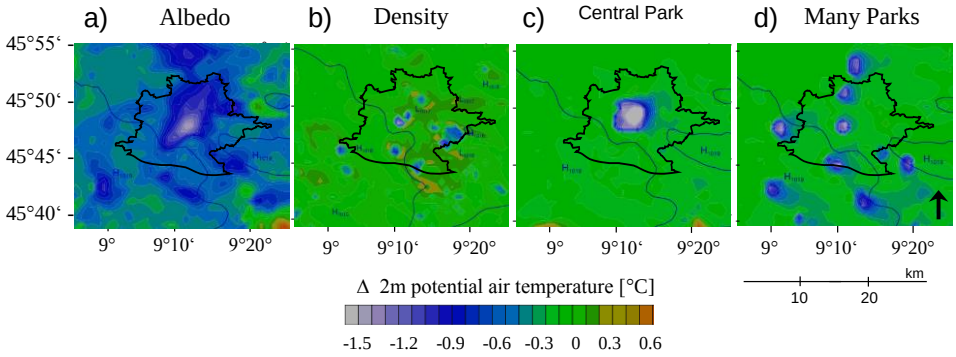

Fig. 47: Difference in potential 2m air temperature for the four scenarios: a) changed albedo for roofs and walls, b) modified proportion street width/building height and the two urban greening scenarios with one big park (c) and a number of smaller parks (d); projected time is August 13 2003 2000h

The changes in Θ range from -2 to 0 °C, whereas in certain areas an increase in air temperature is registered, but only up to 0.5 °C. The areas with blue and white shading indicate a decrease of near surface temperature. For the ‘Albedo’ scenario (a), the reflectivity for each urban grid cell throughout the domain is modified, which results in a net temperature decrease throughout the domain. The strongest effect, i.e. the largest decrease in Θ, exists in the city centre with the highest building densities. For the ‘Density’ case (b), the impacts are seen mostly in the high density urban areas where the building geometry has the largest influence on near surface potential temperature. The effect of urban greening is clearly to be distinguished by the light spots in figure c and d. The effect of one single park in the centre extends well beyond the borders of the actual green surface (c). This is partly due to the wind coming from western directions, leading to a net cooling of the air to the east of the park. The same effect can be observed for the different smaller parks (d) showing downwind directed patterns. Here, the total amount of green area in the centre equates to the area depicted in figure c. The following table displays the effect of the different strategies on mean and maximum urban temperature, as well as on UHI intensity

Tab. 11: Impact of urban planning strategies on mean and maximum urban temperature and UHI intensity calculated from model output for August 13 2003 8 pm. The control run indicates ‘real’ conditions.

Scenario	Control	Albedo	Many Parks	Big Park	Density
T mean urban [°C]	33.1	31.5	32.5	32.3	32.4
T max [°C]	34.3	31.9	33.5	33.3	33
UHI; delta Θ	**2.52**	**0.84**	**1.47**	**1.19**	**1.32**

Referring to Tab. 11, a modification of the albedo of wall and roof surfaces has the strongest effect on urban heat island formation, causing a decrease of the UHI intensity by almost 2 °C. Both vegetation scenarios show a decrease of about 1 °C, similar to the 'Density' case. The difference in maximum potential temperature between 'Albedo' and 'Control Case' retrieved for the urban area accounts for 2.4 °C. The mean and maximum temperatures as displayed in Tab. 11 indicate the average over all grid cells and the highest pixel value within the urban area respectively. Because of insufficient observational data in the rural surroundings, it is difficult to retrieve the UHI intensity from measurements. The difference between 2 m temperatures observed at 'Stuttgart Schwabenzentrum' (37.4 °C) and at The University of Hohenheim in the near rural surrounding (33.1 °C) amounts to 4.3 °C for August 13 2000 h local time. Considering the difference in elevation for the two locations (150 m), this value still amounts to 3° C.

In the following, the effect on the vertical temperature distribution is discussed by presenting the development over a 60 km west-east cross-section passing the urban centre. By comparing upwind and downwind conditions, the potential to form an urban plume can be discussed.

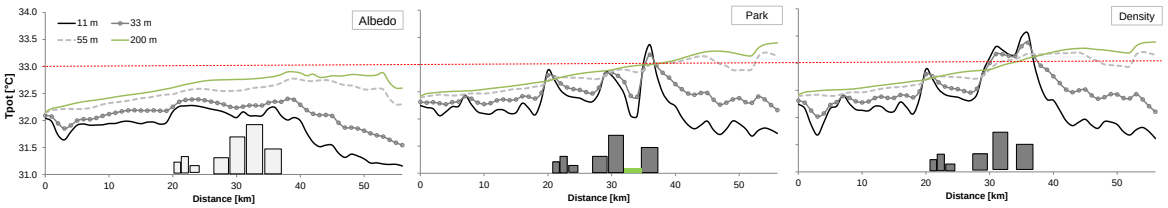

Fig. 48: West-east cross section as indicated in Fig. 29 following the main wind direction and crossing the urban are of Stuttgart. The potential temperature for three different layers (5 m, 15 m, 55 m and 200 m) is illustrated for August 13 2003 2000 h with respect to the 'Albedo' scenario (left), the urban greening scenario 'Central Park' (middle) and changed building densities ('Density') (right). The red line marks the value of 33 °C to merely facilitate the comparison between the scenarios. Control Run is shown in Fig. 32.

Only by comparing the results for the lowest model level (black line), clear differences between the 'Albedo' (left) and 'Central Park' scenarios (middle) can be observed. Whereas the temperature curve is degrading for the entire transect for the left, the effect of a single green area is pronounced more locally with regard to the middle figure. By transforming a rural into a fully vegetated grid cell, air temperature can rapidly decrease by up to 1.5 °C. The effect of changed building density is only minor with regard to the cross section. With changing reflectivity, the increase of temperature with height in the rural surrounding is less than in the Control Run (Fig. 32), because the urban plume effect is

reduced by the intensive cooling of near surface air masses. This is mostly recorded for the 55 and 200 m layers. At about 15 km east of the city, the influence of the urban plume is attenuated noticeably by a decline of the temperature curve. When increasing the reflectivity, the atmospheric layering remains stable throughout the cross-section, an increase of stability in the urban greening scenario only occurs for the atmospheric column directly above the green area. For reduced building densities this effect is not to be observed. A reduction of the surface temperature leads to an increase of the atmospheric stability in the overlying layers. This effect is expressed by lower vertical velocities as presented in Fig. 48.

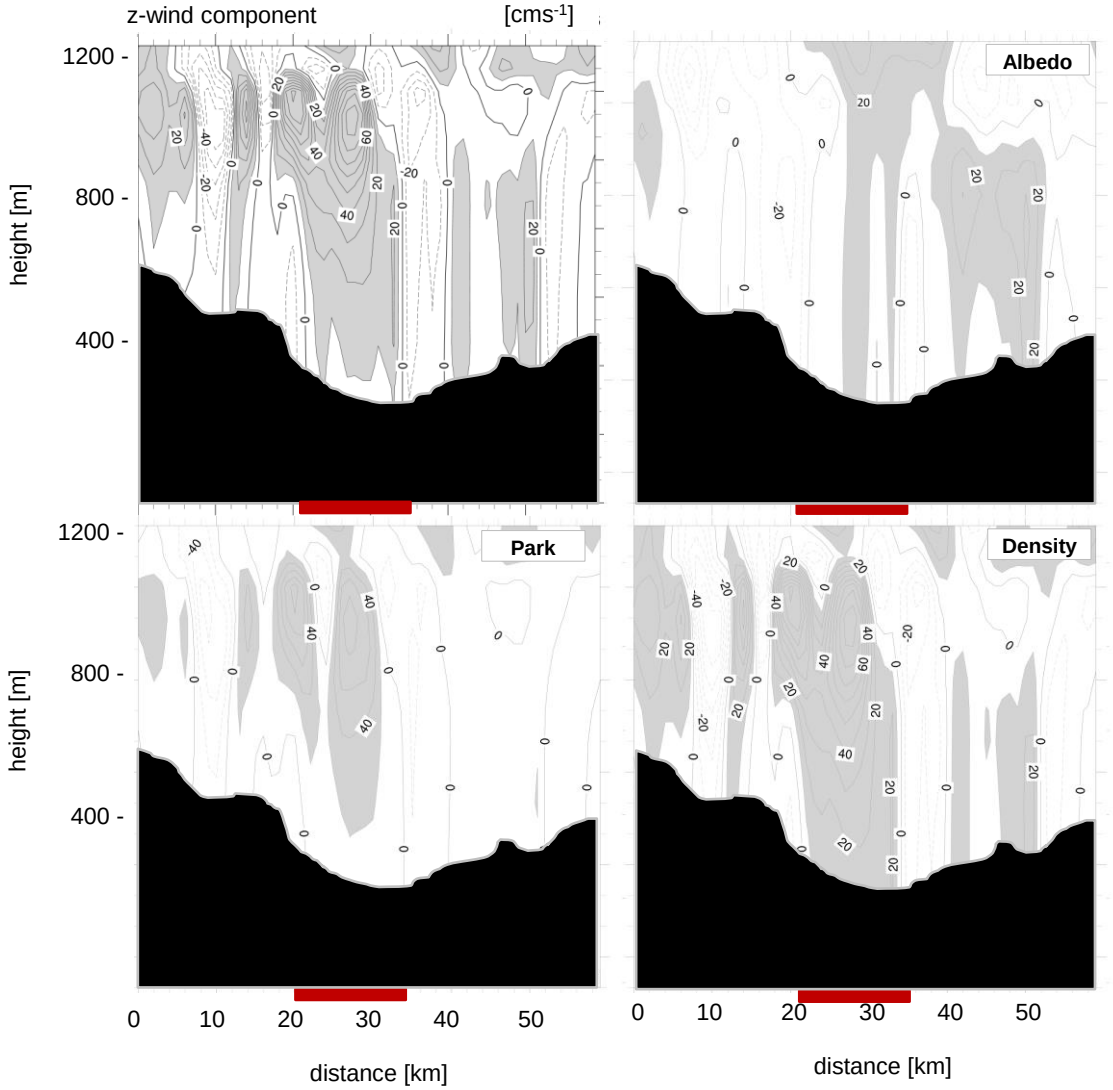

Fig. 49: Same cross section as indicated in Fig. 29 and Fig. 48 showing the vertical wind speed as modelled for the 3 scenarios and the Control Run. The red bar represents the urban area, grey shading indicates positive and white shading negative values or zero. The black pattern represents the topography.

Fig. 49 shows equal cross-sections as already discussed in Fig. 48 for each scenario and the Control Run for an atmospheric column of 1200 m thickness. Grey shading indicates positive (buoyancy) and white colouring negative (subsidence) or zero velocities.

For the albedo- and the urban greening scenario, a decrease of the grey areas just above the city (red bar) can be observed, indicating a reduction of vertical velocities of about 20 to 40 cms^{-1}. For the scenario 'Density', this effect is less pronounced. The 'Albedo' case also shows an effect on the downwind directed side of the valley, with negative values being increased from - 40 to - 20 cms^{-1}. With regard to the urban greening scenario ('Park') the positive fluxes on the lee side disappear.

Tab. 12 summarizes the most important effects of different urban planning scenarios on characteristics of the atmosphere on the basis of mean values for the whole modelling period, with regard to a single urban grid cell.

Tab. 12: Effects of different urban planning scenarios on atmospheric characteristics within the urban canopy. Results are presented for the modelled mean at the urban grid cell as defined in Chapter 6.2. The same is displayed for a rural grid cell isolated from the area influenced by the city. The urban heat island is calculated from the difference between urban and rural mean temperature for both the surface (surface_UHI) and canopy UHI (2m_UHI).

	TSK [°C]	TH2[°C]	TKE10 [m²/s²]	SH [W/m²]	LH [W/m²]	U10 [m/s]	surface_UHI	2m_UHI
Control	27.02	25.56	0.34	90.27	29.33	1.29	3.72	1.09
Albedo	23.55	24.51	0.19	15.53	15.79	1.10	0.25	0.05
Park	23.92	24.97	0.20	28.60	135.88	1.87	0.62	0.50
Density	27.17	25.58	0.34	94.72	29.96	1.29	3.87	1.12
Rural	23.30	24.46	0.20	28.00	138.12	2.30		

With regard to changed albedo and urban greening (Park), the reduced temperature leads to a substantial decrease of air mixing expressed by the turbulent kinetic energy (TKE). This effect is not pronounced for the modified building density. Taking energetic aspects into account, the most dramatic effect is observed for the urban greening scenario, where the Bowen ratio on average is 0.2, compared with 1 for the 'Albedo' case and 3 for the control run. This is due to the fact that a huge part of the total energy flux is attributed to the latent fraction due to the photosynthesis of vegetative surfaces. In the case of a changed albedo, the major reason for cooling is due to the reflection of a large portion of the incoming shortwave radiation. Here, on average, 75 % of the total incoming shortwave radiation is reflected. On the contrary, this value reaches 26 % for 'unchanged conditions' (Control). Changed surface reflectivity shows the highest decrease in average 10 m wind speed, while vertical mixing (TKE) is equally decreased. Referring to Tab. 12, the most efficient way to reduce the UHII is the modification of the reflective properties. According to model

results, it can be reduced by 1 °C with regard to air temperature in the canyon, and even by about 3.5 °C considering the surface temperature. The urban greening scenario leads to a reduction of 0.5 and 3.1 °C, respectively. On average, the effect of changed building densities, such as those applied in the course of this study, are of minor importance.

7.3.2 WRF-Chem: Effect of urban planning strategies on chemical composition

The following results are based on the data and methods explained in Chapter 6.2.

To assess the regional impact of urban temperature reduction on chemical composition, model output for a grid cell in the urban centre is compared for both the Control Run and Scenario Case. The location of the grid cells and chemical compounds are chosen analogue to Chapter 7.2.

Tab. 13: Effect of UHI mitigation scenarios on modelled runtime mean concentrations of O_3, NO, NO_2 and CO as well as formaldehyde (HCHO) and isoprene (C_5H_8) in the urban centre showing absolute values. In addition, the effect on mean potential 2m temperature is shown in the grey shaded area below. A decrease is presented in italics and the maximum effect is presented in bold. Normal formatting reveals an increase.

Scenario	Control	Albedo	Park	Density
NO[ppb]	4.69	**5.84**	4.92	4.71
NO2[ppb]	20.57	**23.37**	22.02	20.97
PM10 [ug/m³]	21.84	**23.39**	23.08	22.43
CO [ppb]	366.74	**398.84**	381.95	368.95
O3 [ppb]	40.10	*38.40*	***36.92***	*39.87*
HCHO [ppb]	5.48	5.84	**5.46**	5.47
C5H8 [ppb]	1.03	1.34	**1.23**	1.03
Tmean [°C]	26.81	25.64	25.50	26.40

In contrast to previous results, the values in Tab. 13 represent an average for a single 3 x 3 km grid cell in the centre of the city (Chapter 6.3.5) over the whole modelling period. The main focus is being put on selected chemical compounds commonly used to assess the air quality in urban areas in Europe (Guerreiro, de Leeuw, & Foltescu 2013). The nitrate compounds NO and NO_2 are often incorporated into NO_x, PM_{10} represents the coarse fraction of aerosols commonly measured in urban air and CO is another measure for classifying the pollution of urban environments. Ozone, O_3 is a secondary component whose formation strongly depends on temperature, radiation and the presence of precursor substances such as NO_x or VOCs, which are represented by formaldehyde (HCHO) and

isoprene (C_5H_8). The chemical interactions are manifold and there are a lot of other compounds interrelating in a various number of reactions. These eight compounds however, are used in the following to classify the urban air quality of the modelling area and further relate the change in concentrations to the expected change in temperature according to the specific urban planning scenario. All values are discussed in parts per billion (ppb). In the following, the main focus is being put on NO_x, CO and ozone showing the largest effects.

On average, ozone concentrations are decreasing for each scenario, whereas the strongest effect is projected for urban greening. In this case, a reduction in mean urban temperature by about 1°C (comparable to an UHI reduction of 1°C) results in a decrease of O_3 concentration by 2 ppb (8 %). For the albedo scenario, the temperature effect also constitutes a 1°C reduction, albeit with the effect on ozone being less (1.5 ppb - 5%). Peak ozone concentration is an important indicator for the impact of air quality on human health. For this reason, the 8h-mean value for daytime ozone concentrations (WMO standard) is calculated from the model output. This reveals a decrease of 4 % for the 'Albedo' and 5 % for the 'Park' scenario. The effect of an altered building density is only marginal.

The effect however is different with regard to primary pollutants NO and CO and to a small amount also primary NO_2. The latter accounts for 5 % of the total nitrate oxide emission within the emission inventory. A temperature reduction of 1 °C causes a significant relative increase of up to 25 % for NO with regard to modified roof albedos ('Albedo'). With respect to the urban greening scenario, this number only amounts to 5 %. The 'Albedo' scenario shows the largest effects for all compounds listed in Tab. 13 except for ozone, where the highest impact is projected for the urban greening scenario ('Park'). Because the model has problems with correctly simulating the PM_{10} and $PM_{2.5}$ concentrations (Fig. 28), the effect is not well pronounced. The amount of isoprene is increased for 'Albedo' and 'Park'.

Although concentrations are higher during night time due to enhanced atmospheric stability, the impact of land surface modifications is higher during the day, as relative changes in Tab. 14 reveal for urban greening (Park) and increased albedo (Albedo).

Tab. 14: Modelled relative effect on mean daytime and night-time concentration of NO, NO_2, CO and ozone during Aug 09 - Aug 18 2003

Delta [%]		NO	NO2	CO	O3
Albedo	**Day**	27.75	19.23	24.52	-3.94
	Night	11.11	9.21	5.85	-6.22
Park	**Day**	3.69	11.40	18.42	-7.97
	Night	9.00	2.82	1.88	-5.06

With regard to the urban greening scenario (Park), the day-night effect for NO is reversed with higher concentrations to be found during the night. A higher amount of NO on the contrary results in a lower amount of ozone represented by a smaller relative decrease of daytime concentrations.

In order to illustrate the individual scenarios' impact on a daily basis, model output is extracted for August 13 2003. Fig. 50 shows daily trends of NO_x (NO_2+NO), CO, Ozone and equivalent potential temperature. Changing the surface properties by either incorporating more vegetation or by changing the reflective properties of roof areas tends to have larger effects on near surface concentrations of primary compounds than by changing geometrical features.

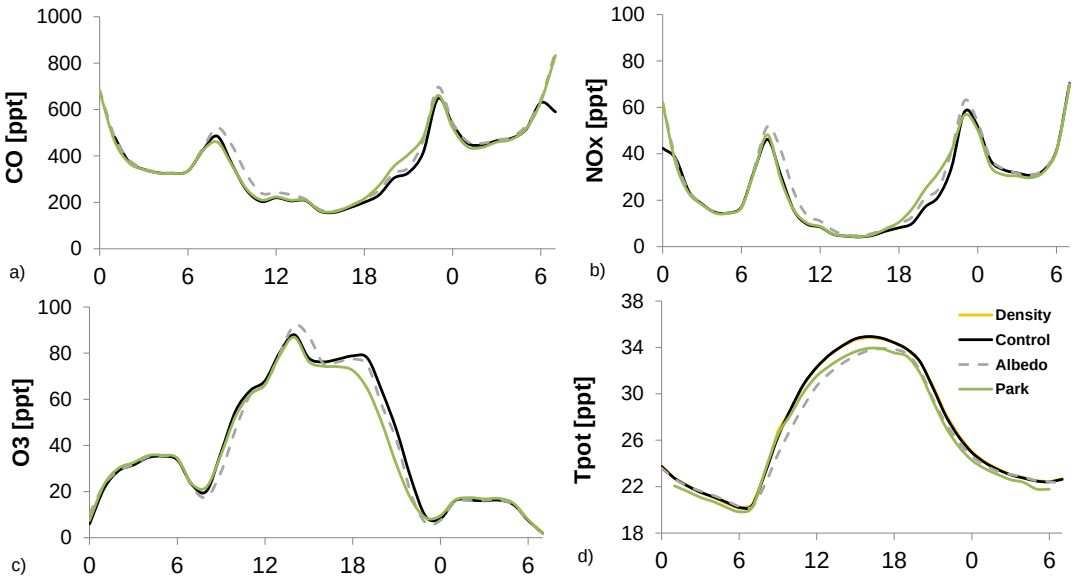

Fig. 50: Daily trend for concentrations of CO (a), NO_x (b) and ozone (c) for August 13 0000 h to August 14 0600 h presenting the three scenarios and the control run.

In general, simulated concentrations of CO and NO_x follow a diurnal trend showing distinct peaks in the morning and evening hours. These peaks are amplified when changing land surface characteristics. As already indicated by Tab. 13, all three scenarios show a concentration increase. This effect is well pronounced in the morning for carbon monoxide

(a) and nitrate oxide (b) shows significant effects in the evening and night-time. Concerning ozone (c), a decrease in daily mean concentration is predicted for each scenario except for 'Albedo'. An increase of the surface reflectivity however promotes an increase of peak O_3 between 1400 h and 1600 h. Although this effect is cancelled out when averaging over the whole modelling period, it accounts for an increase of 6 ppb (almost 7 %) with regard to Fig. 50c. As this effect is not to be observed for the urban greening scenario (Park), the mean concentrations are lower than compared to 'Albedo'. This effect is to be further discussed in Chapter 8.2.

The effect of the temperature reduction on atmospheric chemical composition is mostly pronounced for the near surface layers inside or shortly above the urban canopy. Fig. 51 shows the mean concentrations comparing results from the control run (Control) and the scenarios (Albedo, Park) for the three locations analysed in Chapter 7.2.2 (Fig. 42b) with regard to the lowest two model levels (10 m and 33 m). The wind direction changes in the course of the day, from mostly north-west during the day, to south-east during the night. Urban and rural environments are defined by selecting three model grid cells, one north-west (NW) an urban (Urban) and another one south-east (SE). The difference in concentration of NO_x, CO and O_3 between both rural locations indicates the dominating direction of pollutant transport.

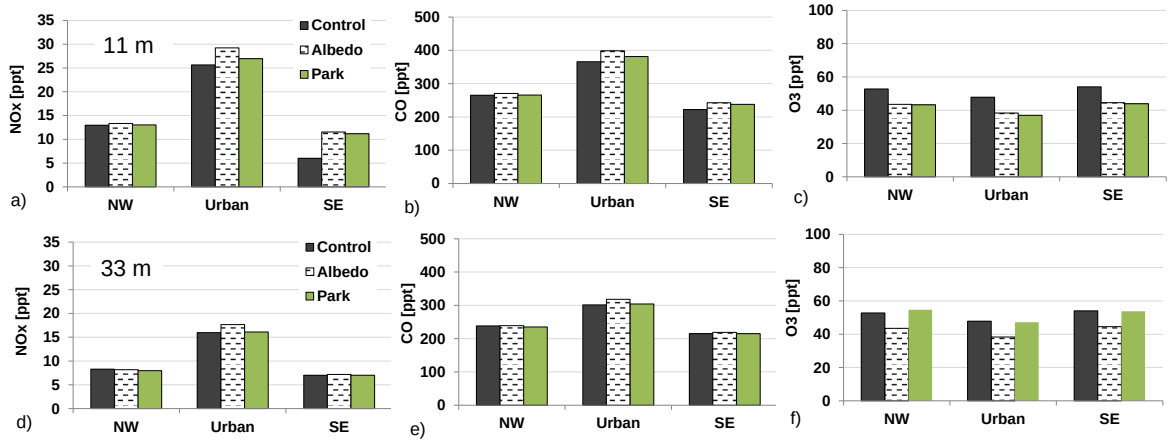

Fig. 51: Concentration of NOx, CO and O_3 averaged over the time period Aug 09-Aug 18 2003 presented for two scenarios (Albedo and Park) and the control run (Control). 2 vertical levels – 5 m (a-d) and 33 m (e-h) are displayed for an urban location (Urban) and two rural locations - one upwind (NW) and the other one downwind (SE), both at a distance of about 20 km to the urban centre.

In general, the concentrations in the urban centre (Urban) increase for both scenarios and so do the concentrations in the rural counterparts in both directions. Values northwest of

the city are proportionally higher than in south eastern direction. Compared with ‘normal’ conditions (Control) however, the differences in mean upwind and downwind concentrations are decreased when changing the albedo or the vegetation content. The following table shows the differences in mean surface concentrations for both rural locations for three selected compounds.

Tab. 15: Difference in mean surface concentration between the north-west (NW) and south-east (SE) rural locations with regard to each scenario and control run

	Control		Albedo		Park	
	Urban	**NW-SE**	**Urban**	**NW-SE**	**Urban**	**NW-SE**
NOx	25.65	6.96	29.21	1.81	26.94	1.85
CO	365.99	43.10	398.34	28.07	381.53	27.68
O3	40.10	-1.22	38.40	-1.01	36.00	-0.66

Followed by reduced temperature according to the specific scenario, the urban-rural circulation, expressed as the difference between both rural locations (NW-SE) is somehow supressed although the net concentrations of primary pollutants in the urban centre (Urban) show an increase. The change in the difference between both rural locations can be attributed basically to an increase of concentrations in the southeast direction, resulting from daytime circulations. By reducing the urban temperature, the urban heat island intensity decreases in conjunction with a decrease of the energetic potential between urban and rural locations. Accordingly, the secondary circulation is disturbed. With regard to ozone, the effect is minor.

8. Discussion

A modification of land surface properties like reflectivity, vegetation content or roughness leads to changes in the nature of the overlying atmosphere. Every scenario applied in the course of that work evokes a reduction of (near surface) air temperatures which can have effects on atmospheric dynamics and can also affect the reactivity of chemical reactions (Seinfeld & Pandis 2012). The response of concentrations to changed boundary conditions can be manifold.

Whereas the impact on ozone is highly driven by temperature and radiation, primary pollutants show a high dependency on atmospheric dynamics responsible for vertical mixing and deposition. Beyond that, primary and secondary pollutants interact via complex chemical reactions, where a change in concentration of one compound can provoke negative feedbacks to other compounds. The reasons for modified chemical composition within an urban canyon due to altered urban characteristics are complex. Recent (Forkel and Knoche 2006) and previous studies (Guenther et al. 1993) have found that an elevated temperature leads to an increased emission of isoprene (C_5H_8), which correspondingly leads to an increase in the concentration. This effect is not fully observed in this work. With regard to Tab. 13, the concentrations of C_5H_8 show an increase with reduced temperature, albeit the net emission is simulated to decrease. By this, it is assumed that processes are involved which generate contrary effects to that usually expected considering the relevant literature.

Based on the model results, changed atmospheric dynamics are assumed to represent the core impact on the concentration of primary pollutants, whereas the temperature itself can be used to sufficiently explain the effect on ozone (Fig. 53a).

8.1 Effects of reduced temperature on atmospheric dynamics

When reducing the temperature of the urban surface and the air within the street canyon respectively, dynamic processes are impeded (e.g. Fig. 49). Consequently, air mixing intensity as represented by the TKE (turbulent kinetic energy) as well as the height of the planetary boundary layer (PBLH) is decreased. Especially for changed surface reflectivity (Albedo) and urban greening (Park), atmospheric dynamics are attenuated significantly (Tab. 16).

Tab. 16: Effects of the specific scenario on mean of turbulent kinetic energy (TKE) and planetary boundary layer height (PBLH)

Scenario	Control	Albedo	Park	Density
TKE [$m^{-2}s^{-2}$]	0.34	0.23	0.22	0.33
PBLH [m]	563.0	519.0	485.0	618.0

On a daily average, reductions of the TKE by about 0.1 m^{-2} s^{-2} and the PBLH by about 50 m and 80 m can be observed for the 'Albedo' and the 'Park' scenario, respectively. The impact on TKE is not obvious when changing the building structures (Density). Moreover, the boundary layer is even increased compared with the control run. Whereas temperature reduction by changed reflectivity and urban greening leads to a decline of the boundary layer, broader street canyons result in an elevation. For this reason, this scenario only shows a minor effect on temperature. This urban planning strategy would get more important when adjusting major roads in the direction to fresh air corridors providing natural ventilation, which would lead to a local cooling and removal of pollutants. Below, the 'Density' scenario is excluded from the discussion.

Whereas the effect of an urban temperature reduction on the urban heat island formation is most obvious during evening and night time periods, the impact of land surface modification on local air quality is mostly pronounced during the day, where turbulent mixing is intense. The absolute concentrations however are higher at night, due to a higher degree of atmospheric stability.

Along with the effect of reduced atmospheric dynamics comes an increase of daily averaged surface concentrations of NO_x and CO within the urban canopy. Vertical mixing is depressed and net surface concentrations increase. Fig. 52 shows the relationship between turbulent kinetic energy (TKE) and simulated hourly concentrations of NO_x and CO respectively with regard to the control run. Aerosols (PM_{10}) are not discussed here as the model does not show a large effect.

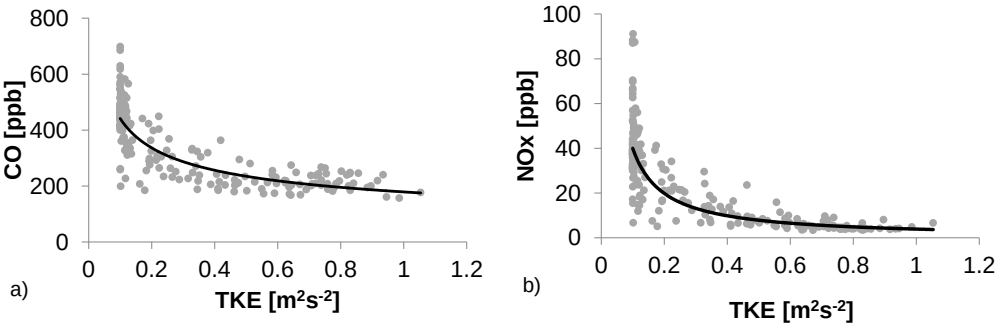

Fig. 52: Dependence of near surface concentration of primary pollutants on atmospheric dynamics explained by the correlation between turbulent kinetic energy (TKE) and surface concentrations of CO (a) and NO_x (b) for hourly model output of the modelling period (Aug 09 - Aug 17 2003).

Although urban greening shows the highest effect on TKE and an equal decrease of the boundary layer height (Tab. 16), the effect on chemical composition drops behind the other scenario (Albedo). The trapping effect of street canyons is still valid when only changing the reflective properties of roofs and wall façades, whereas the 'Park' scenario implies that buildings are completely replaced by natural vegetation (Park). Less primary pollutants imply fewer precursors for ozone formation, which result in a net loss of ozone. This relationship is explained in Chapter 8.2.

Natural vegetation tends to dissipate sensible heat in favour of latent heat. This effect promotes a smaller vertical extend of the PBLH. The crucial term to explain the effect of increasing concentrations coming along with reduced temperatures however is not the extent of the PBLH, but the intensity of turbulent mixing, which seems to have a larger impact for changed building albedos rather than for urban greening. Referring to Chapter 7.3.2, the urban heat island intensity might also have an impact on air quality, being responsible for the formation of secondary circulation systems. According to model results however, no correlation between the urban heat island intensity and concentration of air pollutants can be found.

The temperature reduction itself however shows no direct correlation to the concentration of primary pollutants, which leads to the assumption that the larger part can be attributed to a modification of the dynamic structure of the atmosphere or the presence of another 'third body' acting as a precursor to a concentration change with changed temperature. A change in concentration of one pollutant due to a decrease in atmospheric mixing however can evoke a secondary impact on another compound via chemical reactions. This aspect reveals the complex interrelations in the urban atmosphere and it is fairly hard to quantify

from mesoscale models, which effect is dominating the impacts of certain urban planning measures on the chemical composition.

8.2 Effects of temperature and radiation on chemical reactivity

The loss of ozone with temperature reduction cannot be directly explained by a change of atmospheric dynamics as it is valid for the primary pollutants CO, NO_x and PM_x. A manifold range of processes and compounds are involved in photochemical reaction chains. On the one hand, ozone formation is strongly driven by the physical temperature (4.5). On the other hand, its concentration is connected to the presence of precursor substances. For reasons of simplification, the effect of urban planning scenarios on ambient ozone concentrations is explained in the following by some basic processes.

As ozone is a secondary pollutant, production and destruction is strongly dependent on the existence of precursor substances. The ozone production efficiency (OPE) is an important measure to describe the effect of increasing concentrations of NO_x on ozone formation. In the process of ozone generation, NO_x gets cycled back and forth between NO and NO_2. Therefore, NOx can be seen as catalyst for O_3 formation (Seinfeld & Pandis 2012). Nitric oxide NO, which is emitted through combustion processes is quickly converted to NO_2 via photolysis reactions. As the reaction continues, nitrogen dioxide reacts to form nitrate. As levels of NO are increasing, the levels of ozone drop rapidly (Finlayson-Pitts & Pitts Jr 1999). This effect is dominating the night-time processes where no photolysis occurs and almost all NO_x is converted to NO_2. The amount of ozone which is still available in the atmosphere can react with the present NO_2 to form nitrate (NO_3). At daytime, the situation gets more complex because NO and NO_2 interconvert by the photochemical NO_x cycle. In general, the OPE decreases with an increase of NO_x (Seinfeld & Pandis 2012). According to model results, an increasing amount of NO_x caused by temperature reduction correlates with a decrease of ozone levels (Fig. 53b). Different from primary pollutants like CO or PM_x, the production of ozone directly depends on air temperature as calculated by the box model in Chapter 4.4 (Fig. 12). By this, a decrease in potential near surface temperature according to the specific scenario as presented in Tab. 13 results in a net reduction in ozone concentration (Fig. 53a). By this, the removal and formation of ozone is central to the chemistry of the troposphere (Seinfeld & Pandis 2012)

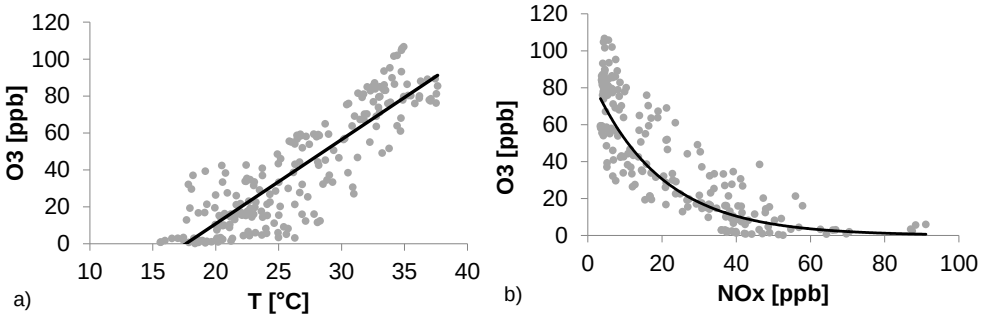

Fig. 53: Dependence of surface ozone concentrations on temperature reduction by correlating potential 2 m temperature and surface concentrations of O_3 (a) and NO_x and O_3 (b) for hourly model output of the modelling period (Aug 09 - Aug 18 2003).

Whereas a positive linear relationship can be found for the correlation of ozone concentrations to air temperature (a), the relation between NO_x and O_3 is of negative exponential nature (b).

Another important factor promoting photochemical reactions in the troposphere is the influence of high energetic shortwave radiation. This aspect explains the increase of peak ozone levels when changing the reflectivity of roof surfaces, although the effective temperature has been decreased (Fig. 50c). This effect can be explained by comparing reflected short wave radiation (SW_UP) for both 'Albedo' and 'Park' scenario and correlating this variable with ozone concentration and photolysis rate respectively (Fig. 54).

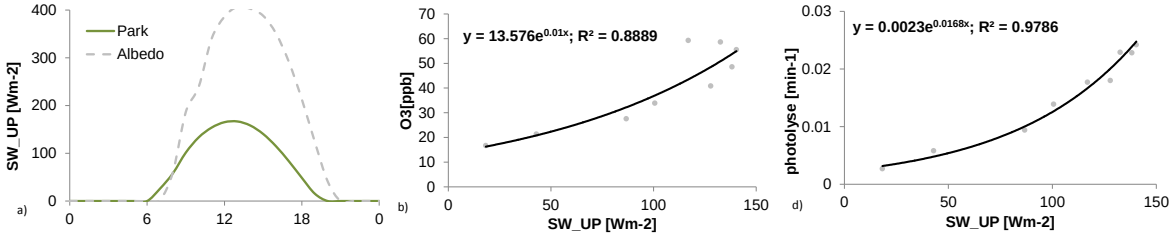

Fig. 54: Reflected short-wave radiation (SW_UP) for the scenarios 'Park' and 'Albedo' (a). Correlation between SW_UP and surface concentrations of O3 (b) and SW_UP and O3 photolysis rate (c) for daily averaged model output.

Fig. 54 indicates that there is a strong dependence between reflected short wave energy and the formation of ozone between 1400 h and 1600 h. The comparison between the urban greening and the white roof scenario illustrates one of the key feedback mechanisms when changing the surface reflectivity of building materials. Besides the cooling effect, the net

radiation at the earth's surface significantly dominates chemical reactions as has been explained on the basis of ozone formation.

The chemistry of the troposphere is further dominated by the amount of free hydroxyl radicals (OH), which can be involved in effective removal mechanisms of tropospheric CO. Although a major part of CO loss can be explained by the change in atmospheric dynamics, it should also be pointed out that its concentration is also dependent on the amount of free hydroxyl-radicals (OH) in the air. In the presence of CO, OH and OH_2 cycle between themselves, leading to a steady state partitioning. By this, CO is also closely linked to the NO_x cycle (Chapter 4.1). For both urban greening and changed roof albedos, a decrease of OH is simulated, as it basically forms from the reaction with ozone. A positive correlation between temperature and OH, calculated from the control run is shown in Fig. 55a, followed by a decrease of CO respectively (Fig. 55b). CO is involved in chemical reactions including NO_x, by this both compounds are linearly correlated (Fig. 55c). OH itself is also an important sink of nitrate when oxidizing NO_2, inferring also a negative correlation of NO_2 and OH (not presented).

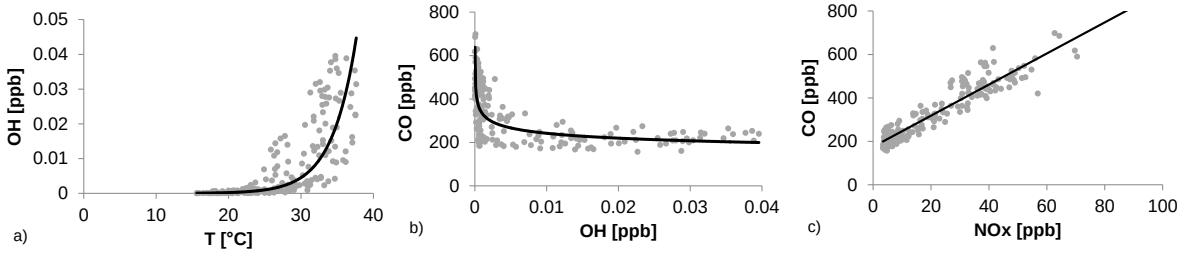

Fig. 55: Explanations of the effect of increasing CO with decreasing temperature based on the correlation between potential 2m temperature and OH (a), OH and CO (b) as well as CO and surface concentrations of NO_x (c) for hourly model output of the modelling period (Aug 09 - Aug 18 2003).

The urban atmosphere is characterized by a large portion of VOCs. The ratio between NO_x and VOCs in turn can alter the efficiency of ozone production. Higher concentration of NO_x can result in less efficient production of ozone. The sensitivity of NO_x and VOC in forming ozone can be analysed by a statistical relationship and presented in a two-dimensional (Fig. 56a) and a three-dimensional way (Fig. 56b) to enable the classification into a NO_x-limited or a VOC limited regime (Finlayson-Pitts & Pitts Jr 1999). Although concentrations of VOCs are rather small in this case, the following graphs can be used to partly explain the reduction of ozone caused by an increase of NO_x. HCHO is used to

illustrate this effect, as it can be counted to one of the most efficient ozone precursors (Seinfeld & Pandis 2012).

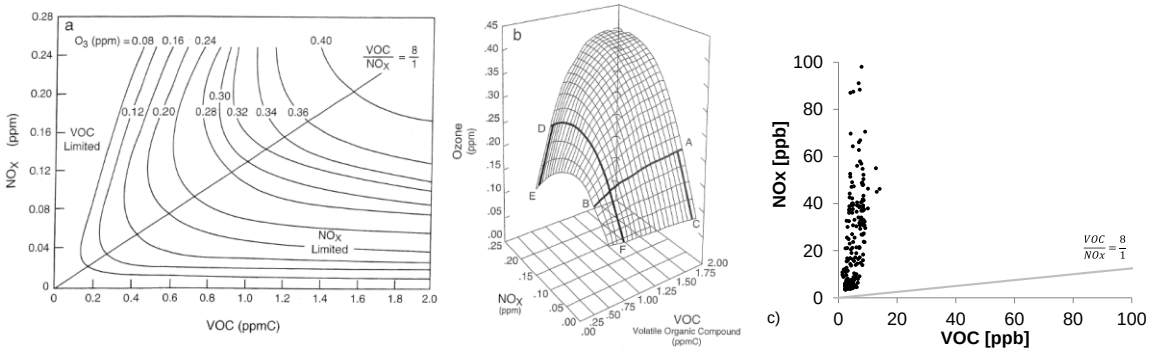

Fig. 56: Typical peak ozone isopleths generated from initial mixtures of VOCs and NO_x in air based modelling experiments explained in Finlayson-Pitts and Pitts (1999). Two dimensional plot relating the VOC/NO_x ratio to ozone concentrations generated by a model (a) and three-dimensional depiction for the same case (b). Figure c shows the relation between VOC to NO_x based on the actual WRF-Chem modelling results, indicating the regime being highly NO_x limited.

With regard to Fig. 56a, the concentrations to the right of the centremost line are characteristic of rural or suburban areas. The areas to the left with lower VOC/NO_x ratios are typical for highly polluted major urban areas (Finlayson-Pitts & Pitts Jr 1999).

According to WRF-Chem results (Fig. 56c), the regime can be classified as highly NO_x limited where an increase of NO_x concentrations at constant VOC concentration actually leads to a decrease in O_3. This effect can be illustrated when following line DF in Fig. 56b. Reducing NO_x here at a constant VOC leads to an increase in ozone till the ridgeline is reached. On the contrary, a reduction of VOC concentrations at constant NO_x along the line DE results in a decrease of the O_3 level. This complex behaviour can be explained by two basic effects.

First, ozone is rapidly titrated when reacting with NO. A second reason for O_3 responding to NO_x at low VOC/NO_x ratios and high concentrations of NO_x respectively is the competition of NO_2 with VOC for the OH radical by forming HNO_3. This reaction sets an end to the chain oxidation of VOCs and removes nitrate dioxide without generating ozone. Since air masses are transported in the course of the day, the simulated ratio is not representative for a single grid cell at one point in time but rather for an area in some distance downwind. By choosing the average value, this effect is assumed to be cancelled out. As the initial concentration of NO_x is decreased when reducing the urban temperature, this effect is helpful to partly explain the loss in net concentration of O_3. Although night

time concentrations are higher for both scenarios, the relative impact on net concentrations is larger during the day except with regard to NO when simulating an urban greening scenario (Park).

8.3 Hourly budgets to quantify the impact on chemical composition

The impact of each urban planning scenario on atmospheric chemical composition is expressed in different ways. The general tendency, except for ozone, is an increase of concentrations with reduced urban temperature. With regard to urban greening for instance, the impact of decreased temperature on atmospheric mixing (TKE) is most pronounced (Tab. 16); even so the increase of mean concentrations of primary pollutants is higher for the 'Albedo' scenario. Both dynamical and chemical effects cause a negative impact on air quality. Nonetheless, it is very difficult to distinguish between primary and secondary effects.

In order to quantify the scenario impact on ambient chemical composition in the simulations, the respective contributions of the various physical phenomena in interaction are evaluated for NO_x, CO and O_3. For this reason, WRF-Chem calculates accumulated tendency terms, which can be derived directly from the model output. On the basis of these terms, it is possible to calculate hourly budgets for each compound in order to quantify the impact of chemical and dynamical tendencies on altered atmospheric composition. The Albedo scenario is used as an example to illustrate the interrelations.

The budget terms for the chemical species, which are provided by WRF-Chem output are: chemical production/loss tendency (CHEM), turbulent vertical mixing tendency (TURB) and advective tendency (ADV). Negative values indicate a loss, positive values a gain according to the respective budget term. The term EMIS describes the emission as given in the emission inventory and the term Gain/Loss can be calculated by adding up the different budget terms, including the hourly emission.

The hourly budgets are computed considering time of the day with maximum concentrations of NO, NO_2 and CO (0008h to 0009h) (Tab. 17) and Ozone (1500h to 1600h) (Tab. 18) for both Control Run and 'Albedo'. Following the methods shown by (Sarrat et al. 2006), hourly averaged budget terms are calculated from model output which

can be used to quantify the contributions of chemical and dynamical mechanisms on net urban concentrations.

Tab. 17: Components of the hourly budget as provided by WRF-Chem output for NO, NO_2 and CO between 0800 and 0900 h (Unit ppbv h^{-1}) with regard to the Control Run (Control) and the Albedo scenario.

	CHEM	TURB	ADV	EMIS	Gain/Loss
NO_Control	-20.11	-9.56	-0.08	73.50	43.75
NO_Albedo	-13.44	-4.80	1.02	73.50	56.28
NO2_Control	16.33	-21.02	-0.48	6.90	1.73
NO2_Albedo	12.35	-10.30	3.19	6.90	12.14
CO_Control	1.02	-353.88	118.79	504.00	269.93
CO_Albedo	0.71	-103.16	53.17	504.00	454.72

The results from Tab. 17 indicate that the biggest change in budget terms comparing control and scenario run (Albedo) can be attributed to vertical mixing (TURB). All turbulent budget terms reflect a negative hourly budget, comparable to a loss of net concentration. With regard to the scenario run (Albedo), this term is decreased for all three compounds. In particular, this effect is most pronounced for carbon monoxide (CO). The decrease in turbulence accounts for 70 %, whereas the decrease of the chemical term only is 30 %. The decrease of the advective term (ADV) accounts for 55 %. When calculating the net gain/loss by adding the net hourly emission, it becomes obvious that the net gain is increased for all compounds when reducing the urban temperature. The negative trends in tendency indicate the highest effects for turbulent and advective terms, which lead to the conclusion that dynamical processes are dominating the effect of temperature decrease on the chemical composition of the urban air.

Since ozone is highly correlated to physical temperature, a net loss is predicted for the Albedo scenario Tab. 18. The explanations above are not directly applicable to ozone. As it is a secondary pollutant, net concentrations additionally depend on several precursor substances, which make a general statement about the trend in tendency budgets rather difficult.

Tab. 18: Components of hourly budget computed for O_3 between 1500 and 1600 h (Unit ppbv h^{-1})

	CHEM	TURB	ADV	EMIS	Gain/Loss
O3_Control	-7.43	28.33	1.35		22.25
O3_Albedo	-5.15	1.90	-23.10		-26.36

9. Conclusions

This work analyzed the effect of different urban heat island mitigation strategies on local and regional air quality using the mesoscale chemical transport model WRF-Chem. An urban parameterization scheme has been included in order to represent urban sub-scale processes.

Different urban schemes which are implemented in WRF (Chen et al. 2011) have been evaluated for the test bed of Stuttgart. Local observations have been exploited in order to calibrate the urban canopy model and evaluate several parameterization schemes with different complexity. The physical and chemical schemes in the model have been adapted for a 33-class land use classification. It turned out that a multi-layer urban canopy model was best suitable to reproduce thermal conditions and turbulent structures in the urban environment.

Different scenario runs were conducted, representing changed reflectivity of buildings (‘Albedo’), two different forms of urban greening (‘Big Park’, ‘Many Parks’) and a modified building density (‘Density’). The modeling time period was August 09 - August 17 2003, representing a period with excessive heat in Central Europe.

All scenarios were able to locally reduce the temperature at the surface and within the urban canopy and thus to reduce the urban heat island intensity. With a maximum surface temperature reduction of 3.5 °C and a projected decrease of the urban heat island intensity by almost 2 °C, effects are most pronounced when incorporating highly reflective materials for buildings (‘Albedo’). In the model, this was achieved by changing the albedo from roofs and walls from 0.2 to 0.7. Due to reflection of a large part of the incoming shortwave radiation, this scenario significantly modified the energy balance at the surface, resulting in a net decrease of temperature. While this strategy only implied changes in the radiative characteristics of building materials, the urban greening scenario (‘Big Park’) requires physical transformation of urban space (building, roads) to natural vegetation. Here, temperature reduction is mainly due to a shift from sensible to latent heat fluxes. The effect on temperature was in the order of 3°C at most, the urban heat island could be reduced by about 1 °C. The grid cell effect of changed building density (‘Density’) was less pronounced. The effect on the UHI was also in the order of 1 °C. A change of surface properties can have significant effects on vertical wind velocities and urban rural

circulation patterns. Again, the strongest effect was projected for the ‘Albedo’ case. The results are in quite good agreement with similar studies applied for other cities (Rizwan et al. 2008).

The major outcome of this work is the simulated effect of these scenarios on urban air quality. The model results support the positive effect of green areas and reduced albedos on ambient ozone concentrations, with a mean reduction by 5-8 %. This positive effect on secondary pollutants was most pronounced for urban greening although the temperature effect was higher for the ‘Albedo’ scenario. In contrast to the positive correlation between temperature and ozone formation it could be documented that peak ozone concentrations can even increase when increasing the reflectivity of impervious surfaces, because the driving force for photochemical reactions is the intensity of shortwave radiation. By reflecting a large portion of incoming solar radiation, white roofs can actually increase peak ozone concentrations during daytime, although temperature has been decreased.

In contrast to secondary pollutants such as ozone, the concentrations of primary pollutants such as NO, CO and PM_{10} were increased by 5-25 % on average, because temperature reduction had a significant effect on the dynamic structure of the atmosphere. A decrease of turbulent kinetic energy (TKE) due to lower temperatures leads to a lower rate of turbulent mixing and a decrease of the mixing layer height, thus slowing down the dilution of pollutants. According to calculated budget terms (Chapter 8.3), it could be proven that dynamical effects are dominating chemical processes when assessing the effect of UHI mitigation strategies on the amount of CO and NO_x.

Urban-rural circulation patterns are responsible for the transport of urban pollutants into the rural surrounding. For the urban area of Stuttgart located in complex terrain, the latter was quite difficult to quantify. It was assumed that the transport of pollutants here was mainly caused by a reversal of the wind direction over the course of the day, leading to an enhanced urban-rural transport process during the night-time.

This study selected one urban area with characteristic topographical and meteorological features and a fixed time period (9 consecutive days during August 2003) with clear skies and calm conditions. The effects of clouds and precipitation were not accounted for. The meteorological patterns did not change significantly, except the diurnal wind-direction. By choosing a different modelling setup, initial conditions can change and might not be in

total accordance with the findings in this work. Further, the effects explained before are not taking into account that a reduction of temperature might also reduce the emission of primary pollutants from air conditioning, which accordingly might lead to a decrease of concentrations.

The present study can serve as decision support for local urban planners, authorities, stakeholders and not least for urban inhabitants. It contributes to questions of sustainable planning of water and energy supply in order to efficiently use available resources or to develop efficient building materials and infrastructure. Further it helps to improve heat wave predictions and health assessment studies in order to assess, preserve and ameliorate the quality of life. Understanding the complexity of chemical and dynamical interrelations is a key process to improve the resilience of urban areas under the pressure of a changing climate and an increasing rate of urbanization. For this reason, existing modelling systems have to be further improved.

One aspect which is the focus of current scientific work in the field of urban air quality is the role of biogenic emissions. The fact that urban greening can negatively affect the air quality by the emission of biogenic compounds is not accounted for in this work, but should be a major challenge in future studies.

Appendix

A.1 Documentation for Using Corine/USGS Landuse Data (33 classes) as WRF Input with help of ArcGIS/ MATLAB

- Download landuse Data from http://www.eea.europa.eu/themes/landuse/interactive/clc-download or order from DLR http://www.corine.dfd.dlr.de/corine_order_de.html
- Take corine 250m
- Insert to ArcGIS → Add Data
- Resample pixel size to 1km: Data Management → Raster Processing → Resample
- Set Coordinate System to WGS 84 → Project Raster

- Find location of region of interest in WRF-geographical data (landuse_30s):
  - 1 Tile = 1200x1200 → 10°
  - Calculate how many 10°-Steps E/N till region of interest
  - Multiply steps with 1200
  - Format: xstart.xend-ystart.yend (21601-22800.15601.16800)
  - 21601-22800.16801-18000
  - 22801-24000.15601-16800
  - 22801-24000.16801-18000

- read tile-data (30s-resolution) in MATLAB and convert to GIS-readable (ASCII): code may look something like:

```
lons = -179.99583:0.00833333:180;
lats  = -89.99583:0.00833333:90;
fid    = fopen('21600-22800.15601-16800')
data = fread(fid);
data = reshape(data', 1200, 1200);
data=rot90(data);
save file.txt data –ASCII
```

- insert header to file.txt → conversion → ascii to raster

```
ncols         1200
nrows         1200
xllcorner     0
yllcorner     40
cellsize      0.00833333
NODATA_value  -9999
```

- Extract corine landcover by mask of file.tif
- Reclassify corine landuse-classes to USGS according LANDUSE.TBL (3 urban classes)

- Export reclassified map as binary format → map.bil

- Open map.bil in matlab + open '21600-22800.15601-16800' (30s) → make them looking the same by rotating and reshaping
- Create new file new.bil → fid=fopen('new.bil','w+') → fwrite(fid,new)

Matlab script:

```
fid = fopen('map.bil');
data = fread(fid);
data = reshape(data,1200,1200);
data = fliplr(data);
data = data(:);
fis = fopen('new.bil','w+');
fwrite (fis,data);
fclose (fis);
```

- Change name of new.bil to '21600-22800.15601-16800'
- Replace original tile by new one
- Insert classes 31,32,33 in VEGPARAM.TBL

REMAP-Table

Grid ID (GIS)	CORINE ID	USGS (WRF)
1	111	32
2	112	31
3	121	33
4	122	33
5	123	33
6	124	33
7	131	19
8	132	33
9	133	33
10	141	32
11	142	32
12	211	2
13	212	3
14	213	3
15	221	4
16	222	4
17	223	4
18	241	4

19	242	4
20	243	4
21	244	15
22	311	11
23	312	14
24	313	15
25	321	7
26	322	17
27	323	17
28	324	18
29	331	25
30	332	19
31	333	19
32	334	19
33	335	24
34	411	17
35	412	17
36	421	17
37	422	17
38	423	17
39	511	16
40	511	16

- Set min/max num_land_cat in index file of 30s-resolution to 2/33
- Index file: isurban = 31
- Registry.EM: num_land_cat = 33
- Set dimensions of domains in namelist.wps
- ./geogrid.exe with new landuse-data
- Load module ncarg
- Ncl check location of domains
- Link Vtable.GFS
- Link in GRIB data → ./link_grib.csh
- ./ungrib.exe
- ./metgrid.exe

- Change Variables in Landuse.TBL and VegPar.TBL for 3 urban categories (31-low,32-high and 33-industrial/commercial) through ArcGIS-Analysis of Landsat5 TM-, MODIS- Images and Literature
- Parameters to be adapted:
  - ALBD: Mean Albedo for summer and winter period
  - SLMO: Soil Moisture

- SFEM: Surface Emission
- SFZO: Roughness
- THERIN: Thermal Inertia
- SHDFAC: Green Vegetation Fraction
- LAIMIN, LAIMAX: min/max Leaf Area Index
- EMISSMIN/EMISSMAX: min/max Emission
- ALBEDOMIN/MAX
- Z0MIN/MAX

Addition to chemical run

- Initialization of new model layer : adapt ‘chemics.init.F’ for 33 land use classes
- Complement dry deposition module ‘module_dep_simple.F’ in order to account for 33 classes
- Complement biogenic emission module ‘module_bioemiss_simple.F’ in order to account for 33 classes

A.2 WRF: ‘LANDUSE.TBL’

```
33,2, 'ALBD   SLMO   SFEM   SFZ0 THERIN   SCFX   SFHC   '

SUMMER
1,     15.,   .10,   .88,   80.,    3.,  1.67, 18.9e5,'Urban and Built-Up Land'
2,     17.,   .30,  .985,   15.,    4.,  2.71, 25.0e5,'Dryland Cropland and Pasture'
3,     18.,   .50,  .985,   10.,    4.,  2.20, 25.0e5,'Irrigated Cropland and Pasture'
4,     18.,   .25,  .985,   15.,    4.,  2.56, 25.0e5,'Mixed Dryland/Irrigated Cropland and Pasture'
5,     18.,   .25,   .98,   14.,    4.,  2.56, 25.0e5,'Cropland/Grassland Mosaic'
6,     16.,   .35,  .985,   20.,    4.,  3.19, 25.0e5,'Cropland/Woodland Mosaic'
7,     19.,   .15,   .96,   12.,    3.,  2.37, 20.8e5,'Grassland'
8,     22.,   .10,   .93,    5.,    3.,  1.56, 20.8e5,'Shrubland'
9,     20.,   .15,   .95,    6.,    3.,  2.14, 20.8e5,'Mixed Shrubland/Grassland'
10,    20.,   .15,   .92,   15.,    3.,  2.00, 25.0e5,'Savanna'
11,    16.,   .30,   .93,   50.,    4.,  2.63, 25.0e5,'Deciduous Broadleaf Forest'
12,    14.,   .30,   .94,   50.,    4.,  2.86, 25.0e5,'Deciduous Needleleaf Forest'
13,    12.,   .50,   .95,   50.,    5.,  1.67, 29.2e5,'Evergreen Broadleaf Forest'
14,    12.,   .30,   .95,   50.,    4.,  3.33, 29.2e5,'Evergreen Needleleaf Forest'
15,    13.,   .30,   .97,   50.,    4.,  2.11, 41.8e5,'Mixed Forest'
16,     8.,  1.0,    .98,  0.01,    6.,   0., 9.0e25,'Water Bodies'
17,    14.,   .60,   .95,   20.,    6.,  1.50, 29.2e5,'Herbaceous Wetland'
18,    14.,   .35,   .95,   40.,    5.,  1.14, 41.8e5,'Wooded Wetland'
19,    25.,   .02,   .90,    1.,    2.,  0.81, 12.0e5,'Barren or Sparsely Vegetated'
20,    15.,   .50,   .92,   10.,    5.,  2.87, 9.0e25,'Herbaceous Tundra'
21,    15.,   .50,   .93,   30.,    5.,  2.67, 9.0e25,'Wooded Tundra'
22,    15.,   .50,   .92,   15.,    5.,  2.67, 9.0e25,'Mixed Tundra'
23,    25.,   .02,   .90,   10.,    2.,  1.60, 12.0e5,'Bare Ground Tundra'
24,    55.,   .95,   .95,   0.1,    5.,   0., 9.0e25,'Snow or Ice'
25,    30.,   .40,   .90,    1.,    5.,   .62, 12.0E5,'Playa'
```

```
26,    18.,  .50,  .95,  15.,   6.,   .62, 12.0E5,'Lava'
27,    70.,  .40,  .90,   1.,   5.,    0., 12.0E5,'White Sand'
28,    15.,  .02,  .88,  80.,   3.,  1.67, 18.9e5,'Unassigned'
29,    15.,  .02,  .88,  80.,   3.,  1.67, 18.9e5,'Unassigned'
30,    15.,  .10,  .88,  80.,   3.,  1.67, 18.9e5,'Unassigned'
31,    30.,  .15,  .93,  60.,   3.,  1.67, 18.9e5,'Low Intensity Residential '
32,    20.,  .12,  .91,  120.,  3.,  1.67, 18.9e5,'High Intensity Residential'
33,    15.,  .10,  .87,  50.,   3.,  1.67, 18.9e5,'Industrial or Commercial'

WINTER
1,     15.,  .10,  .88,  80.,   3.,  1.67, 18.9e5,'Urban and Built-Up Land'
2,     20.,  .60,  .92,  5.,    4.,  2.00, 25.0e5,'Dryland Cropland and Pasture'
3,     20.,  .50,  .93,  2.,    4.,  1.76, 25.0e5,'Irrigated Cropland and Pasture'
4,     20.,  .50,  .92,  5.,    4.,  2.00, 25.0e5,'Mixed Dryland/Irrigated Cropland and Pasture'
5,     20.,  .40,  .92,  5.,    4.,  2.00, 25.0e5,'Cropland/Grassland Mosaic'
6,     20.,  .60,  .93,  20.,   4.,  2.00, 25.0e5,'Cropland/Woodland Mosaic'
7,     23.,  .30,  .92,  10.,   4.,  2.00, 20.8e5,'Grassland'
8,     22.,  .20,  .93,  1.,    4.,  1.30, 20.8e5,'Shrubland'
9,     22.,  .25,  .93,  1.,    4.,  1.24, 20.8e5,'Mixed Shrubland/Grassland'
10,    20.,  .15,  .92,  15.,   3.,  2.00, 25.0e5,'Savanna'
11,    17.,  .60,  .93,  50.,   5.,  2.40, 25.0e5,'Deciduous Broadleaf Forest'
12,    15.,  .60,  .93,  50.,   5.,  2.60, 25.0e5,'Deciduous Needleleaf Forest'
13,    12.,  .50,  .95,  50.,   5.,  1.67, 29.2e5,'Evergreen Broadleaf Forest'
14,    12.,  .60,  .95,  50.,   5.,  3.00, 29.2e5,'Evergreen Needleleaf Forest'
15,    14.,  .60,  .93,  20.,   6.,  1.12, 41.8e5,'Mixed Forest'
16,     8.,  1.0,  .98,  0.01,  6.,    0., 9.0e25,'Water Bodies'
17,    14.,  .75,  .95,  20.,   6.,  1.50, 29.2e5,'Herbaceous Wetland'
18,    14.,  .70,  .95,  40.,   6.,  1.14, 41.8e5,'Wooded Wetland'
19,    23.,  .05,  .90,  1.,    2.,  0.81, 12.0e5,'Barren or Sparsely Vegetated'
20,    15.,  .60,  .92,  10.,   5.,  2.00, 9.0e25,'Herbaceous Tundra'
21,    15.,  .60,  .93,  30.,   5.,  1.75, 9.0e25,'Wooded Tundra'
22,    15.,  .60,  .92,  15.,   5.,  1.75, 9.0e25,'Mixed Tundra'
23,    25.,  .05,  .90,  5.,    5.,  1.80, 12.0e5,'Bare Ground Tundra'
24,    70.,  .95,  .95,  0.1,   5.,    0., 9.0e25,'Snow or Ice'
25,    40.,  .40,  .90,  1.,    5.,   .62, 12.0E5,'Playa'
26,    18.,  .40,  .95,  15.,   5.,   .62, 12.0E5,'Lava'
27,    70.,  .40,  .90,  1.,    5.,    0., 12.0E5,'White Sand'
28,    15.,  .02,  .88,  80.,   3.,  1.67, 18.9e5,'Unassigned'
29,    15.,  .02,  .88,  80.,   3.,  1.67, 18.9e5,'Unassigned'
30,    15.,  .10,  .88,  80.,   3.,  1.67, 18.9e5,'Unassigned'
31,    25.,  .18,  .93,  60.,   3.,  1.67, 18.9e5,'Low Intensity Residential '
32,    15.,  .15,  .91,  120.,  3.,  1.67, 18.9e5,'High Intensity Residential'
33,    12.,  .10,  .85,  50.,   3.,  1.67, 18.9e5,'Industrial or Commercial'
```

A.3 WRF: 'VEGPARM.TBL'

```
Vegetation Parameters
USGS
33,1, 'SHDFAC NROOT  RS    RGL    HS     SNUP  MAXALB  LAIMIN  LAIMAX  EMISSMIN EMISSMAX ALBEDOMIN ALBEDOMAX Z0MIN  Z0MAX  ZTOPV  ZBOTV'
1,   .10, 1,  200.,  999.,  999.0,  0.04,  46.,  1.00,  1.00,  .880,  .15,  .15,  .50,  .50,  0.00,  0.00,  0.00,  'Urban and Built-Up Land'
2,   .80, 3,  40.,   100.,  36.25,  0.04,  66.,  1.56,  5.68,  .920,  .985,  .17,  .23,  .05,  .15,  0.50,  0.01,  'Dryland Cropland and Pasture'
3,   .80, 3,  40.,   100.,  36.25,  0.04,  66.,  1.56,  5.68,  .930,  .985,  .20,  .25,  .02,  .10,  0.50,  0.01,  'Irrigated Cropland and Pasture'
4,   .80, 3,  40.,   100.,  36.25,  0.04,  66.,  1.00,  4.50,  .920,  .985,  .18,  .23,  .05,  .15,  0.50,  0.01,  'Mixed Dryland/Irrigated Cropland and Pasture'
5,   .80, 3,  40.,   100.,  36.25,  0.04,  68.,  2.29,  4.29,  .920,  .980,  .18,  .23,  .05,  .14,  0.50,  0.01,  'Cropland/Grassland Mosaic'
6,   .80, 3,  70.,   65.,   44.14,  0.04,  60.,  2.00,  4.00,  .930,  .985,  .16,  .20,  .20,  .20,  0.50,  0.01,  'Cropland/Woodland Mosaic'
7,   .80, 3,  40.,   100.,  36.35,  0.04,  70.,  0.52,  2.90,  .920,  .960,  .19,  .23,  .10,  .12,  0.50,  0.01,  'Grassland'
8,   .70, 3,  300.,  100.,  42.00,  0.03,  60.,  0.50,  3.66,  .930,  .930,  .25,  .30,  .01,  .05,  0.50,  0.10,  'Shrubland'
9,   .70, 3,  170.,  100.,  39.18,  0.035, 65.,  0.60,  2.60,  .930,  .950,  .22,  .30,  .01,  .06,  0.50,  0.10,  'Mixed Shrubland/Grassland'
10,  .50, 3,  70.,   65.,   54.53,  0.04,  50.,  0.50,  3.66,  .920,  .920,  .20,  .20,  .15,  .15,  5.00,  0.10,  'Savanna'
11,  .80, 4,  100.,  30.,   54.53,  0.08,  58.,  1.85,  3.31,  .930,  .930,  .16,  .17,  .50,  .50,  20.0,  11.5,  'Deciduous Broadleaf Forest'
12,  .70, 4,  150.,  30.,   47.35,  0.08,  54.,  1.00,  5.16,  .930,  .940,  .14,  .15,  .50,  .50,  14.0,  7.0,  'Deciduous Needleleaf Forest'
13,  .95, 4,  150.,  30.,   41.69,  0.08,  35.,  3.08,  6.48,  .950,  .950,  .12,  .12,  .50,  .50,  35.0,  1.0,  'Evergreen Broadleaf Forest'
14,  .70, 4,  125.,  30.,   47.35,  0.08,  52.,  5.00,  6.40,  .950,  .950,  .12,  .12,  .50,  .50,  17.0,  8.5,  'Evergreen Needleleaf Forest'
15,  .80, 4,  125.,  30.,   51.93,  0.08,  53.,  2.80,  5.50,  .930,  .970,  .17,  .25,  .20,  .50,  18.0,  10.0,  'Mixed Forest'
16,  .00, 0,  100.,  30.,   51.75,  0.01,  70.,  0.01,  0.01,  .980,  .980,  .08,  .08,  0.0001,  0.0001,  0.00,  0.00,  'Water Bodies'
17,  .60, 2,  40.,   100.,  60.00,  0.01,  68.,  1.50,  5.65,  .950,  .950,  .14,  .14,  .20,  .20,  0.50,  0.01,  'Herbaceous Wetland'
18,  .60, 2,  100.,  30.,   51.93,  0.02,  50.,  2.00,  5.80,  .950,  .950,  .14,  .14,  .40,  .40,  20.0,  11.5,  'Wooded Wetland'
19,  .01, 1,  999.,  999.,  999.0,  0.02,  75.,  0.10,  0.75,  .900,  .900,  .38,  .38,  .01,  .01,  0.02,  0.01,  'Barren or Sparsely Vegetated'
20,  .60, 3,  150.,  100.,  42.00,  0.025, 68.,  0.41,  3.35,  .920,  .920,  .15,  .20,  .10,  .10,  0.50,  0.01,  'Herbaceous Tundra'
21,  .60, 3,  150.,  100.,  42.00,  0.025, 55.,  0.41,  3.35,  .930,  .930,  .15,  .20,  .30,  .30,  10.0,  0.10,  'Wooded Tundra'
22,  .60, 3,  150.,  100.,  42.00,  0.025, 60.,  0.41,  3.35,  .920,  .920,  .15,  .20,  .15,  .15,  5.00,  0.10,  'Mixed Tundra'
23,  .30, 2,  200.,  100.,  42.00,  0.02,  75.,  0.41,  3.35,  .900,  .900,  .25,  .25,  .05,  .10,  0.02,  0.01,  'Bare Ground Tundra'
24,  .00, 1,  999.,  999.,  999.0,  0.02,  82.,  0.01,  0.01,  .950,  .950,  .55,  .70,  0.001,  0.001,  0.00,  0.00,  'Snow or Ice'
25,  .50, 1,  40.,   100.,  36.25,  0.02,  75.,  0.01,  0.01,  .890,  .890,  .30,  .30,  .01,  .01,  0.00,  0.00,  'Playa'
26,  .00, 0,  999.,  999.,  999.0,  0.02,  75.,  0.01,  0.01,  .880,  .880,  .16,  .16,  .15,  .15,  0.00,  0.00,  'Lava'
27,  .00, 0,  999.,  999.,  999.0,  0.02,  75.,  0.01,  0.01,  .830,  .830,  .60,  .60,  .01,  .01,  0.00,  0.00,  'White Sand'
28,  .00, 0,  999.,  999.,  999.0,  0.02,  75.,  0.01,  0.01,  .830,  .830,  .60,  .60,  .01,  .01,  0.00,  0.00,  'Unassigned'
29,  .00, 0,  999.,  999.,  999.0,  0.02,  75.,  0.01,  0.01,  .830,  .830,  .60,  .60,  .01,  .01,  0.00,  0.00,  'Unassigned'
30,  .00, 0,  999.,  999.,  999.0,  0.02,  75.,  0.01,  0.01,  .830,  .830,  .60,  .60,  .01,  .01,  0.00,  0.00,  'Unassigned'
31,  .30, 1,  200.,  999.,  999.0,  0.04,  45.,  1.00,  2.50,  .880,  .950,  .20,  .45,  .30,  .50,  0.00,  0.00,  'Low Intensity Residential '
32,  .12, 1,  200.,  999.,  999.0,  0.04,  45.,  1.00,  1.50,  .880,  .900,  .20,  .45,  1.10,  1.30,  0.00,  0.00,  'High Intensity Residential'
33,  .07, 1,  200.,  999.,  999.0,  0.04,  45.,  1.00,  1.00,  .850,  .880,  .20,  .45,  .30,  .50,  0.00,  0.00,  'Industrial or Commercial'
TOPT_DATA
298.0
CMCMAX_DATA
0.5E-3
CFACTR_DATA
0.5
RSMAX_DATA
5000.0
BARE
19
NATURAL
```

A.4 WRF: ‘namelist.wps’

```
&share
 wrf_core = 'ARW',
 max_dom = 3,
 start_date = '2003-08-11_00:00:00','2003-08-11_00:00:00','2003-08-11_00:00:00',
 end_date   = '2003-08-18_00:00:00','2003-08-11_00:00:00','2003-08-11_00:00:00',
 interval_seconds = 21600,
 io_form_geogrid = 2,
 debug_level = 1000
/

&geogrid
 parent_id         =   0,1,2,
 parent_grid_ratio =   1,5,3,
 i_parent_start    =   1,18,37,
 j_parent_start    =   1,10,21,
 e_we              =   43,76,61,
 e_sn              =   34,56,49,
 geog_data_res     = '30s','30s','30s',
 dx = 15000,
 dy = 15000,
 map_proj = 'lambert',
 ref_lat   =  49.00,
 ref_lon   =  8.00,
 truelat1  =  30.0,
 truelat2  =  60.0,
 stand_lon =  10.0,
 geog_data_path = '/home/fallmann-j/WRF/DATA/geogwrf3'

/

&ungrib
 out_format = 'WPS',
 prefix = 'FILE',
/

&metgrid
 fg_name = 'FILE'
 io_form_metgrid = 2,
/
```

A.5 WRF-Chem: ‘namelist.wps’

```
&share
 wrf_core = 'ARW',
 max_dom = 1,
 start_date = '2003-08-08_00:00:00',
 end_date = '2003-08-18_00:00:00',
 interval_seconds = 21600,
 io_form_geogrid = 2,
/

&geogrid
 parent_id         =   1,
 parent_grid_ratio =   1,
 i_parent_start    =   1,
 j_parent_start    =   1,
 e_we              =   250,
 e_sn              =   200,
 geog_data_res     =   '30s',
 dx = 3000,
 dy = 3000,
 map_proj  =  'lambert',
 ref_lat   =  48.5,
 ref_lon   =  8.6,
 truelat1  =  30.0,
 truelat2  =  60.0,
 stand_lon =  10.0,
 geog_data_path = '/scratch1/portfolios/BMC/ap-fc/fallmann/Data/GEOG'
/

&ungrib
 out_format = 'WPS',
 prefix = 'FILE',
/

&metgrid
 fg_name = 'FILE'
 io_form_metgrid = 2,
/
```

A.6 WRF/WRF-Chem: 'namelist.input'

```
&time_control
 run_days                  = 9,
 run_hours                 = 0,
 run_minutes               = 0,
 run_seconds               = 0,
 start_year                = 2003,
 start_month               = 08,
 start_day                 = 09,
 start_hour                = 00,
 start_minute              = 00,
 start_second              = 00,
 end_year                  = 2003,
 end_month                 = 08,
 end_day                   = 18,
 end_hour                  = 00,
 end_minute                = 00,
 end_second                = 00,
 interval_seconds          = 21600,
 input_from_file           = .true.,
 history_interval          = 60, !60
 frames_per_outfile        = 300, !1000
 frames_per_auxinput5              = 24,
 restart                   = .false.,
 restart_interval          = 44640,
 io_form_history           = 2,
 io_form_restart           = 2,
 io_form_input             = 2,
 io_form_boundary          = 2,
 debug_level               = 0,
 auxinput4_interval        = 360,
 auxinput5_interval_m      = 60,
 io_form_auxinput5         = 2,
 io_form_auxinput12        = 2,
 auxinput12_inname         = "wrf_chem_input",
 io_form_auxinput6         = 2,
 auxinput6_inname          = "wrfbiochemi_d01",
 /
&dfi_control
/
&logging
/
 &domains
 time_step                 = 10,
 time_step_fract_num       = 0,
 time_step_fract_den       = 1,
 max_dom                   = 1,
 s_we                      = 1,
 e_we                      = 250,
 s_sn                      = 1,
 e_sn                      = 200,
 s_vert                    = 1,
 e_vert                    = 36,
 eta_levels     = 1.0000, 0.9987, 0.9974, 0.9947, 0.9921, 0.9895, 0.9869, 0.9830, 0.9791, 0.9739, 0.9674,
          0.9610,  0.9508,  0.9406,  0.9281,  0.9157,  0.9021,  0.8887,  0.8743,  0.8389,  0.8045,  0.7603,
```

```
          0.6973,  0.6379,  0.5644,  0.4968,  0.4274,  0.3645,  0.3018,  0.2460,  0.1918,  0.1405,  0.0999,
0.0618, 0.0295, 0.000
 p_top_requested                  = 5000,
 num_metgrid_levels               = 38,
 num_metgrid_soil_levels          = 4,
 dx                          = 3000,
 dy                          = 3000,
 grid_id                     = 1,
 parent_id                   = 0,
 i_parent_start              = 1,
 j_parent_start              = 1,
 parent_grid_ratio           = 1,
 parent_time_step_ratio          = 1,
 feedback                    = 0,
 smooth_option               = 0,
 /

 &physics
 mp_physics                  = 2, !changed from 3
 mp_zero_out                 = 2,
 mp_zero_out_thresh              = 1.e-8   ! critical value for moist array threshold, below which
 ra_lw_physics               = 4, !1
 ra_sw_physics               = 4, !2
 radt                        = 30, !changed from 5
 sf_sfclay_physics           = 2,
 sf_surface_physics          = 2,
 bl_pbl_physics              = 2, !2
 bldt                        = 0,
 cu_physics                  = 3, !changed from 5
 cu_diag                     = 1, !changed from 1
 cudt                        = 0,
 cu_rad_feedback             = .true.,
 isfflx                      = 1,
 ifsnow                      = 0,
 icloud                      = 1,
 surface_input_source            = 1,
 num_soil_layers             = 4,
 sf_urban_physics            = 2,
 num_land_cat                        = 33,
/

&chem
ne_area                     = 41, !changed from 55 (number of chemical species)
kemit                       = 10,
chem_opt                    = 2, !2
bioemdt                     = 30, !15
photdt                      = 30, !15
chemdt                      = 0, !1.5
io_style_emissions          = 2,
emiss_inpt_opt              = 1,
emiss_opt                   = 3,
chem_in_opt                 = 0,
phot_opt                    = 2, !changed from 1
gas_drydep_opt              = 1,
aer_drydep_opt              = 1,
bio_emiss_opt               = 3,
gas_bc_opt                  = 1,
gas_ic_opt                  = 1,
```

```
aer_bc_opt                  = 1,
aer_ic_opt                  = 1,
gaschem_onoff                = 1,
aerchem_onoff                = 1,
wetscav_onoff                = 0,
cldchem_onoff                = 0,
vertmix_onoff                = 1,
chem_conv_tr                 = 1,
seas_opt                    = 0,
dust_opt                    = 0,
biomass_burn_opt             = 0,
plumerisefire_frq            = 30,
have_bcs_chem                = .true., !bc from mozart
aer_ra_feedback              = 0,
aer_op_opt                  = 1,
opt_pars_out                = 1,
diagnostic_chem              = 0,
 /
 &fdda
 /
 &dynamics
 rk_ord                              = 3,  ! Ravan
 w_damping                   = 1,  ! changed from 0 (Ravan)
 diff_opt                    = 1,
 km_opt                      = 4,
 diff_6th_opt                = 2,  !changed from 0
 diff_6th_factor             = 0.12,
 base_temp                   = 290.,
 damp_opt                    = 3,  ! changed from 0
 zdamp                       = 5000.,
 dampcoef                    = 0.2,
 gwd_opt                     = 0,  ! gravity wave drag option (1= on), use when grid size > 10 km
 khdif                       = 0,
 kvdif                       = 0,
 smdiv                       = 0.1  ! divergence damping (0.1 is typical)
 emdiv                       = 0.01 ! external-mode filter coef for mass coordinate model
 non_hydrostatic             = .true.,
 moist_adv_opt               = 1,  !changed from 2
 epssm                       = 0.1 ! time off-centering for vertical sound waves
 do_avgflx_em                = 0,  ! Ravan
 mix_full_fields             = .false. ! used with diff_opt = 2; value of ".true." is recommended, except for
highly idealized
 mix_isotropic               = 0,  ! 0=anistropic vertical/horizontal diffusion
 mix_upper_bound             = 0.1,      ! non-dimensional upper limit for diffusion coeffs, for km_opt = 2,
3
 scalar_adv_opt              = 2,
 chem_adv_opt                = 2,
 tke_adv_opt                 = 2,
 time_step_sound             = 4,   ! number of sound steps per time-step (if using a time_step much larger
than 6*dx, increase number of sound steps). = 0
 h_mom_adv_order             = 5,   ! horizontal momentum advection order
 v_mom_adv_order             = 3,
 h_sca_adv_order             = 5,
 v_sca_adv_order             = 3,
!tke_drag_coefficient         = 0.,  ! surface drag coefficient (Cd, dimensionless) for diff_opt=2 only
 tke_heat_flux               = 0.
 top_lid                     = .false.,     ! zero vertical motion at top of domain (idealized)
 /
```

```
&bdy_control
spec_bdy_width                  = 5,
spec_zone                       = 1,
relax_zone                      = 4,
specified                       = .true.,
nested                          = .false.,
/
&grib2
/
&namelist_quilt
nio_tasks_per_group = 0,
nio_groups = 1,
/
```

Bibliography

Ackermann, I.J., Hass, H., Memmesheimer, M., Ebel, A., Binkowski, F.S., & Shankar, U. 1998. Modal aerosol dynamics model for Europe: development and first applications. Atmospheric Environment, 32, (17) 2981-2999

Ahmad, S. & Hashim, N.M. 2007. Effects of soil moisture on urban heat island occurrences: case of Selangor, Malaysia. *Humanity & Social Sciences Journal*, 2, (2) 132-138

Akbari, H., Pomerantz, M., & Taha, H. 2001. Cool surfaces and shade trees to reduce energy use and improve air quality in urban areas. *Solar Energy*, 70, (3) 295-310

Akbari, H., Bretz, S., Kurn, D.M., & Hanford, J. 1997. Peak power and cooling energy savings of high-albedo roofs. *Energy and Buildings*, 25, (2) 117-126

Akbari, H., Menon, S., & Rosenfeld, A. 2009. Global cooling: increasing world-wide urban albedos to offset CO2. *Climatic Change*, 94, (3-4) 275-286

Amt für Umweltschutz Stuttgart, S. Klimakalender Stuttgart. 2013. accessed at: http://www.stadtklima-stuttgart.de/index.php?klima_kalender_vorwort; 07/22/2014.

Arnfield, A.J. 2003. Two decades of urban climate research: a review of turbulence, exchanges of energy and water, and the urban heat island. *International Journal of Climatology*, 23, (1) 1-26

Arnfield, A.J. & Grimmond, C.S.B. 1998. An urban canyon energy budget model and its application to urban storage heat flux modeling. *Energy and Buildings*, 27, (1) 61-68

Birol, F. 2013, *World energy outlook*, Paris, France: International Energy Agency, 2013: 13.
http://www.worldenergyoutlook.org/media/weowebsite/2013/WEO2013Ch01ScopeAndMethodology.pdf; 07/25/2014.

Bowler, D.E., Buyung-Ali, L., Knight, T.M., & Pullin, A.S. 2010. Urban greening to cool towns and cities: A systematic review of the empirical evidence. *Landscape and Urban Planning*, 97, (3) 147-155

Britter, R.E. & Hanna, S.R. 2003. Flow and dispersion in urban areas. *Annual Review of Fluid Mechanics*, 35, (1) 469-496

Chameides, W.L., Lindsay, R.W., Richardson, J., & Kiang, C.S. 1988. The role of biogenic hydrocarbons in urban photochemical smog: Atlanta as a case study. *Science*, 241, (4872) 1473-1475

Chapman, L. & Thornes, J.E. 2004. Real-Time Sky-View Factor Calculation and Approximation. *Journal of Atmospheric & Oceanic Technology*, 21, (5) 730-741

Chen, F., Kusaka, H., Bornstein, R., Ching, J., Grimmond, C.S.B., Grossman-Clarke, S., Loridan, T., Manning, K.W., Martilli, A., Miao, S., Sailor, D., Salamanca, F.P., Taha, H.,

Tewari, M., Wang, X., Wyszogrodzki, A.A., & Zhang, C. 2011a. The integrated WRF/urban modelling system: development, evaluation, and applications to urban environmental problems. *International Journal of Climatology*, 31, (2) 273-288

Chen, F., Kusaka, H., Bornstein, R., Ching, J., Grimmond, C.S.B., Grossman-Clarke, S., Loridan, T., Manning, K.W., Martilli, A., Miao, S., Sailor, D., Salamanca, F.P., Taha, H., Tewari, M., Wang, X., Wyszogrodzki, A.A., & Zhang, C. 2011b. The integrated WRF/urban modelling system: development, evaluation, and applications to urban environmental problems. *International Journal of Climatology*, 31, (2) 273-288

Chen, Y., Jiang, W.M., Zhang, N., He, X.F., & Zhou, R.W. 2009. Numerical simulation of the anthropogenic heat effect on urban boundary layer structure. Theor Appl Climatol, 97, (1-2) 123-134

Clarke, J.A. 2001. *Energy simulation in building design*. Routledge.

Crutzen, P.J. 1974. Photochemical reactions initiated by and influencing ozone in unpolluted tropospheric air. Tellus, 26, (1-2) 47-57

Dee, D.P., Uppala, S.M., Simmons, A.J., Berrisford, P., Poli, P., Kobayashi, S., Andrae, U., Balmaseda, M.A., Balsamo, G., Bauer, P., Bechtold, P., Beljaars, A.C.M., van de Berg, L., Bidlot, J., Bormann, N., Delsol, C., Dragani, R., Fuentes, M., Geer, A.J., Haimberger, L., Healy, S.B., Hersbach, H., Holm, E.V., Isaksen, L., Källberg, P., Köhler, M., Matricardi, M., McNally, A.P., Monge-Sanz, B.M., Morcrette, J.J., Park, B.K., Peubey, C., de Rosnay, P., Tavolato, C., Thipaut, J.N., & Vitart, F. 2011. The ERA-Interim reanalysis: configuration and performance of the data assimilation system. *Quarterly Journal of the Royal Meteorological Society*, 137, (656) 553-597

Denier van der Gon, H., Visschedijk, A., Van der Brugh, H., & Dröge, R. 2010. A high resolution European emission data base for the year 2005, A contribution to UBA-Projekt PAREST: Particle Reduction Strategies. Accessed at: http://www.umweltbundesamt.de/sites/default/files/medien/461/publikationen/texte_41_2013_appelhans_e03_komplett_0.pdf; 07/15/14.

DWD. Wetterlexikon. 2014. URL: http://www.deutscherwetterdienst.de/lexikon/index.htm?ID=W&DAT=Waermebelastung. 08/07/2014

Emeis, S. 2010. *Surface-based remote sensing of the atmospheric boundary layer*. Series: Atmospheric and Oceanographic Sciences Library, Vol. 40. Springer Heidelberg, X 174pp.

EPA 2012, *Our Nation's Air - Status and Trends through 2010*, US Environmental Protection Agency, Office of Air Quality Planning and Standards: Research Triangle Park, North Carolina.

EPA 2013. Measuring Heat Islands.
Accessed at: http://www.epa.gov/heatisland/about/measuring.htm, 07/22/2014

Erisman, J.W., Van Pul, A., & Wyers, P. 1994. Parametrization of surface resistance for the quantification of atmospheric deposition of acidifying pollutants and ozone. *Atmospheric Environment*, 28, (16) 2595-2607

European Environment Agency (EEA) 2000. CORINE land cover technical guide; Technical report No 40. Accessed at: http://www.eea.europa.eu/publications/tech40add; 07/26/2014.

Fallmann, J., Emeis, S., & Suppan, P. 2014. Mitigation of urban heat stress - a modelling case study for the area of Stuttgart. DIE ERDE - Journal of the Geographical Society of Berlin, 144, (3-4) 202-216

Fan, H. & Sailor, D.J. 2005. Modeling the impacts of anthropogenic heating on the urban climate of Philadelphia: a comparison of implementations in two PBL schemes. *Atmospheric Environment*, 39, (1) 73-84

Fenger, J. 1999. Urban air quality. *Atmospheric Environment*, 33, (29) 4877-4900

Fenger, J. 2009. Air pollution in the last 50 years – From local to global. *Atmospheric Environment*, 43, (1) 13-22

Finlayson-Pitts, B.J. & Pitts Jr, J.N. 1999. *Chemistry of the upper and lower atmosphere: theory, experiments, and applications* Academic press.

Forkel, R. & Knoche, R. 2006. Regional climate change and its impact on photooxidant concentrations in southern Germany: Simulations with a coupled regional climate-chemistry model. *Journal of Geophysical Research: Atmospheres*, 111, (D12) D12302

Grell, G.A., Peckham, S.E., Schmitz, R., McKeen, S.A., Frost, G., Skamarock, W.C., & Eder, B. 2005. Fully coupled "online" chemistry within the WRF model. *Atmospheric Environment*, 39, (37) 6957-6975

Grimm, N.B., Faeth, S.H., Golubiewski, N.E., Redman, C.L., Wu, J., Bai, X., & Briggs, J.M. 2008. Global Change and the Ecology of Cities. Science, 319, (5864) 756-760

Grimmond, C.S.B. 1992. The suburban energy balance: Methodological considerations and results for a mid-latitude west coast city under winter and spring conditions. International Journal of Climatology, 12, (5) 481-497

Grimmond, C.S.B., Potter, S.K., Zutter, H.N., & Souch, C. 2001. Rapid methods to estimate sky-view factors applied to urban areas. *International Journal of Climatology*, 21, (7) 903-913

Grote, R. ., Monson, R., & Niinemets, . l. 2013, "Leaf-Level Models of Constitutive and Stress-Driven Volatile Organic Compound Emissions," *In Biology, Controls and Models of Tree Volatile Organic Compound Emissions*, 5 ed. +. l. Niinemets & R. K. Monson, eds., Springer Netherlands, pp. 315-355.

Guenther, A., Karl, T., Harley, P., Wiedinmyer, C., Palmer, P.I., & Geron, C. 2006. Estimates of global terrestrial isoprene emissions using MEGAN (Model of Emissions of Gases and Aerosols from Nature). *Atmospheric Chemistry & Physics*, 6,

Guenther, A.B., Jiang, X., Heald, C.L., Sakulyanontvittaya, T., Duhl, T., Emmons, L.K., & Wang, X. 2012. The Model of Emissions of Gases and Aerosols from Nature version 2.1 (MEGAN2.1): an extended and updated framework for modeling biogenic emissions. *Geosci.Model Dev.*, 5, (6) 1471-1492

Guenther, A.B., Zimmerman, P.R., Harley, P.C., Monson, R.K., & Fall, R. 1993. Isoprene and monoterpene emission rate variability: Model evaluations and sensitivity analyses. *Journal of Geophysical Research: Atmospheres*, 98, (D7) 12609-12617

Guerreiro, C., de Leeuw, F., & Foltescu, V. 2013, *Air quality in Europe-2013 report*, European Environment Agency, Copenhagen (Denmark). Accessed at: http://www.eea.europa.eu/publications/air-quality-in-europe-2013; 08/13/2014.

Harley, P., Guenther, A., & Zimmerman, P. 1996. Effects of light, temperature and canopy position on net photosynthesis and isoprene emission from sweetgum (Liquidambar styraciflua) leaves. Tree Physiology, 16, (1-2) 25-32

Höppe, P. & Hurk, B. 1999. The physiological equivalent temperature ΓÇô a universal index for the biometeorological assessment of the thermal environment. *Int J Biometeorol*, 43, (2) 71-75

Horowitz, L.W., Walters, S., Mauzerall, D.L., Emmons, L.K., Rasch, P.J., Granier, C., Tie, X., Lamarque, J.F., Schultz, M.G., Tyndall, G.S., Orlando, J.J., & Brasseur, G.P. 2003. A global simulation of tropospheric ozone and related tracers: Description and evaluation of MOZART, version 2. *Journal of Geophysical Research: Atmospheres*, 108, (D24) 4784

Hu, X.M., Nielsen-Gammon, J.W., & Zhang, F. 2010. Evaluation of three planetary boundary layer schemes in the WRF model. *Journal of Applied Meteorology and Climatology*, 49, (9) 1831-1844

Ichinose, T., Shimodozono, K., & Hanaki, K. 1999. Impact of anthropogenic heat on urban climate in Tokyo. Atmospheric Environment, 33, (24GÇô25) 3897-3909

IIASA. Model of Greenhouse Gas - Air pollution Interaction and Synergies (GAINS). 2009. http://gains.iiasa.ac.at/models/, 07/22/2013

Jacobson, M.Z. & Ten Hoeve, J.E. 2011. Effects of Urban Surfaces and White Roofs on Global and Regional Climate. Journal of Climate, 25, (3) 1028-1044

Kalnay, E. & Cai, M. 2003. Impact of urbanization and land-use change on climate. *Nature*, 423, (6939) 528-531

Kesselmeier, J. & Staudt, M. 1999. Biogenic Volatile Organic Compounds (VOC): An Overview on Emission, Physiology and Ecology. Journal of Atmospheric Chemistry, 33.

Kuenen, J., van der Gon, H.D., Visschedijk, A., van der Brugh, H., & van Gijlswijk, R. 2011. MACC European emission inventory for the years 2003–2007. *TNO-report TNO-060-UT-2011-00588, Utrecht.* Accessed at: https://gmes-atmosphere.eu/documents/deliverables/d-emis/TNO%20report_UT-00588_MACC_emission2003_2007.pdf; 09/10/2014.

Kusaka, H., Kondo, H., Kikegawa, Y., & Kimura, F. 2001. A Simple Single-Layer Urban Canopy Model For Atmospheric Models: Comparison With Multi-Layer And Slab Models. *Boundary-Layer Meteorology*, 101, (3) 329-358

Kuttler Wilhelm 2012. Climate Change on the Urban Scale – Effects and Counter-Measures in Central Europe, Human and Social Dimensions of Climate Change, Prof. Netra Chhetri (Ed.), ISBN: 978-953-51-0847-4, InTech, DOI: 10.5772/50867. Accessed at: http://www.intechopen.com/books/human-and-social-dimensions-of-climate-change/climate-change-on-the-urban-scale-effects-and-counter-measures-in-central-europe

Lai, L.W. & Cheng, W.L. 2009. Air quality influenced by urban heat island coupled with synoptic weather patterns. *Science of The Total Environment*, 407, (8) 2724-2733

Liu, Y., Chen, F., Warner, T., & Basara, J. 2006. Verification of a Mesoscale Data-Assimilation and Forecasting System for the Oklahoma City Area during the Joint Urban 2003 Field Project. *Journal of Applied Meteorology and Climatology*, 45, (7) 912-929

Loridan, T. & Grimmond, C.S.B. 2012. Characterization of Energy Flux Partitioning in Urban Environments: Links with Surface Seasonal Properties. *Journal of Applied Meteorology & Climatology*, 51, (2) 219-241

Louis, J.F. 1979. A parametric model of vertical eddy fluxes in the atmosphere. *Boundary-Layer Meteorol*, 17, (2) 187-202

LUBW 2014. Daten- und Kartendienst der LUBW. Accessed at: http://udo.lubw.baden-wuerttemberg.de/public/index.xhtml?pid=.Natur%20und%20Landschaft. 09/10/2014.

Martilli, A., Grossman-Clarke, S., Tewari, M., & Manning, K. W. Description of the modifications made in WRF.3.1 and short user's manual of BEP. 2009. 24-5-2014.

Martilli, A. 2007. Current research and future challenges in urban mesoscale modelling. *International Journal of Climatology*, 27, (14) 1909-1918

Martilli, A., Clappier, A., & Rotach, M. 2002. An Urban Surface Exchange Parameterisation for Mesoscale Models. *Boundary-Layer Meteorology*, 104, (2) 261-304

Mellon, M.T., Jakosky, B.M., Kieffer, H.H., & Christensen, P.R. 2000. High-Resolution Thermal Inertia Mapping from the Mars Global Surveyor Thermal Emission Spectrometer. *Icarus*, 148, (2) 437-455

Mills, G. 2008. Luke Howard and The Climate of London. *Weather*, 63, (6) 153-157

Mitchell, K. N. & C. 2005. The community Noah land surface model LSM - User's Guide Public Release Version 2.7.1. Accessed at: http://www.ral.ucar.edu/research/land/technology/lsm/noah/Noah_LSM_USERGUIDE_2.7.1.pdf, 07/22/2014

Molina, M.J. & Molina, L.T. 2004. Megacities and Atmospheric Pollution. *Journal of the Air & Waste Management Association*, 54, (6) 644-680

Monson, R.K., Jaeger, C.H., Adams, W.W., Driggers, E.M., Silver, G.M., & Fall, R. 1992. Relationships among Isoprene Emission Rate, Photosynthesis, and Isoprene Synthase Activity as Influenced by Temperature. *Plant Physiology*, 98, (3) 1175-1180

Moss, R.H., Edmonds, J.A., Hibbard, K.A., Manning, M.R., Rose, S.K., Van Vuuren, D.P., Carter, T.R., Emori, S., Kainuma, M., Kram, T., Meehl, G.A., Mitchell, J.F.B., Nakicenovic, N., Riahi, K., Smith, S.J., Stouffer, R.J., Thomson, A.M., Weyant, J.P., & Wilbanks, T.J. 2010. The next generation of scenarios for climate change research and assessment. *Nature*, 463, (7282) 747-756

OECD 2011. Meeting the Needs of 9 Billion People, OECD-International Transport forum. Accessed at: http://www.internationaltransportforum.org/pub/pdf/11Outlook.pdf, 07/22/2014

OECD 2012. OECD Environmental Outlook to 2050. *OECDiLibrary*. Accessed at: /content/book/9789264122246-en

Oke, T.R. 1973. City size and the urban heat island. *Atmospheric Environment (1967)*, 7, (8) 769-779

Oke, T.R. 1981a. Canyon geometry and the nocturnal urban heat island: Comparison of scale model and field observations. *Journal of Climatology*, 1, (3) 237-254

Oke, T.R. 1981b. Canyon geometry and the nocturnal urban heat island: Comparison of scale model and field observations. *Journal of Climatology*, 1, (3) 237-254

Oke, T.R. 1982a. The energetic basis of the urban heat island. *Quarterly Journal of the Royal Meteorological Society*, 108, (455) 1-24

Oke, T.R. 1982b. The energetic basis of the urban heat island. *Quarterly Journal of the Royal Meteorological Society*, 108, (455) 1-24

Oke, T.R. 1997. Urban climates and global environmental change. Applied Climatology: Principles & Practices.New York, NY: Routledge 273-287

Oke, T.R. 1987. *Boundary layer climates*, 5 ed. Psychology Press.

Oleson, K.W., Bonan, G.B., & Feddema, J. 2010. Effects of white roofs on urban temperature in a global climate model. *Geophysical Research Letters*, 37, (3) L03701

Onishi, A., Cao, X., Ito, T., Shi, F., & Imura, H. 2010. Evaluating the potential for urban heat-island mitigation by greening parking lots. *Urban Forestry & Urban Greening*, 9, (4) 323-332

Owen, S.M., MacKenzie, A.R., Stewart, H., Donovan, R., & Hewitt, C.N. 2003a. BIOGENIC VOLATILE ORGANIC COMPOUND (VOC) EMISSION ESTIMATES FROM AN URBAN TREE CANOPY. *Ecological Applications*, 13, (4) 927-938

Owen, S.M., MacKenzie, A.R., Stewart, H., Donovan, R., & Hewitt, C.N. 2003b. BIOGENIC VOLATILE ORGANIC COMPOUND (VOC) EMISSION ESTIMATES FROM AN URBAN TREE CANOPY. *Ecological Applications*, 13, (4) 927-938

Quah, A.K.L. & Roth, M. 2012. Diurnal and weekly variation of anthropogenic heat emissions in a tropical city, Singapore. *Atmospheric Environment*, 46, (0) 92-103

Raupach, M.R., Antonia, R.A., & Rajagopalan, S. 1991. Rough-Wall Turbulent Boundary Layers. *Applied Mechanics Reviews*, 44, (1) 1-25

RIZWAN, A.M., DENNIS, L.Y.C., & LIU, C. 2008. A review on the generation, determination and mitigation of Urban Heat Island. *Journal of Environmental Sciences*, 20, (1) 120-128

Roedel, W. & Wagner, T. 1992. Physik unserer Umwelt: Die Atmosphäre, 1 ed. Springer.

Rosenfeld, A.H., Akbari, H., Romm, J.J., & Pomerantz, M. 1998. Cool communities: strategies for heat island mitigation and smog reduction. *Energy and Buildings*, 28, (1) 51-62

Salamanca, F. & Martilli, A. 2012. A numerical study of the Urban Heat Island over Madrid during the DESIREX (2008) campaign with WRF and an evaluation of simple mitigation strategies. *International Journal of Climatology*, 32, (15) 2372-2386

Sander, S.P., Golden, D.M., Kurylo, M.J., Moortgat, G.K., Wine, P.H., Ravishankara, A.R., Kolb, C.E., Molina, M.J., Finlayson-Pitts, B.J., and Huie, R.E. 2006. Chemical kinetics and photochemical data for use in atmospheric studies evaluation number 15.

Sarrat, C., Lemonsu, A., Masson, V., & Guedalia, D. 2006. Impact of urban heat island on regional atmospheric pollution. *Atmospheric Environment*, 40, (10) 1743-1758

Schell, B., Ackermann, I.J., Hass, H., Binkowski, F.S., & Ebel, A. 2001. Modeling the formation of secondary organic aerosol within a comprehensive air quality model system. *Journal of Geophysical Research*, 106, 28

Seinfeld, J.H. & Pandis, S.N. 2012. *Atmospheric chemistry and physics: from air pollution to climate change* John Wiley & Sons.

Sharkey, T.D. & Yeh, S. 2001. Isoprene emission from plants. Annual Review of Plant Physiology and Plant Molecular Biology, 52, (1) 407-436

Skamarock, W. C., Klemp, J. B., Dudhia, J., Gill, D. O., Barker, D. M., Wang, W., & Powers, J. G. 2005. A Description of the Advanced Research WRF Version 2. National Center for Atmospheric Research Boulder CO Moseoscale and microscale meteorolgy division. 1-6-2005.

Solecki, W.D., Rosenzweig, C., Parshall, L., Pope, G., Clark, M., Cox, J., & Wiencke, M. 2005. Mitigation of the heat island effect in urban New Jersey. *Global Environmental Change Part B: Environmental Hazards*, 6, (1) 39-49

Solomon, S. e. al. 2007. Contribution of Working Group I to the Fourth Assessment Report of the Intergovernmental Panel on Climate Change, 2007. Cambridge University Press, Cambridge, United Kingdom and New York, NY, USA. 23-5-2013.
Ref Type: Online Source

Stocker, T.F., Dahe, Q., & Plattner, G.K. 2013. Climate Change 2013: The Physical Science Basis. *Working Group I Contribution to the Fifth Assessment Report of the Intergovernmental Panel on Climate Change.Summary for Policymakers (IPCC, 2013)*

Stockwell, W.R., Kirchner, F., Kuhn, M., & Seefeld, S. 1997. A new mechanism for regional atmospheric chemistry modeling. Journal of Geophysical Research: Atmospheres, 102, (D22) 25847-25879

Stockwell, W.R., Middleton, P., Chang, J.S., & Tang, X. 1990. The second generation regional acid deposition model chemical mechanism for regional air quality modeling. Journal of Geophysical Research: Atmospheres, 95, (D10) 16343-16367

Stone Jr, B. 2012. *The city and the coming climate: Climate change in the places we live* Cambridge University Press.

Stull, R.B. 1988. An introduction to boundary layer meteorology, 13 ed. Springer.

Svensson, M.K. 2004. Sky view factor analysis – implications for urban air temperature differences. *Meteorological Applications*, 11, (3) 201-211

Taha, H. 1996. Modeling impacts of increased urban vegetation on ozone air quality in the South Coast Air Basin. *Atmospheric Environment*, 30, (20) 3423-3430

Taha, H. 1997a. Modeling the impacts of large-scale albedo changes on ozone air quality in the South Coast Air Basin. *Atmospheric Environment*, 31, (11) 1667-1676

Taha, H. 1997b. Urban climates and heat islands: albedo, evapotranspiration, and anthropogenic heat. *Energy and Buildings*, 25, (2) 99-103

Taha, H. 1999. Modifying a Mesoscale Meteorological Model to Better Incorporate Urban Heat Storage: A Bulk-Parameterization Approach. *Journal of Applied Meteorology*, 38, (4) 466-473

Tang, G., Li, X., Wang, Y., Xin, J., & Ren, X. 2009. Surface ozone trend details and interpretations in Beijing, 2001-2006. Atmos.Chem.Phys., 9, (22) 8813-8823 available from: http://www.atmos-chem-phys.net/9/8813/2009/

Tewari, M., Chen, F., Kusaka, H., & Miao, S. Coupled WRF/Unified Noah/Urban-Canopy Modeling System. 2007. https://www.rap.ucar.edu/research/land/technology/urban/WRF-LSM-Urban.pdf, 07/22/2014.

Tong, H., Walton, A., Sang, J., & Chan, J.C.L. 2005. Numerical simulation of the urban boundary layer over the complex terrain of Hong Kong. *Atmospheric Environment*, 39, (19) 3549-3563

UCAR, NCAR, CISL, & VETS. The NCAR Command Language (Version 6.1.2) [Software]. 2013. Boulder, CO.

United Nations 2012, World Urbanization Prospects The 2011 Revision. URL: http://esa.un.org/unup/pdf/FINAL-FINAL_REPORT%20WUP2011_Annextables_01Aug2012_Final.pdf 08/07/2014

USGS 2006. The National Land Cover Database. Accessed at: http://landcover.usgs.gov/usgslandcover.php; 05/25/2014.

Visser, W. 2009. The top 50 sustainability books. O. D. van Heel (Ed.). Greenleaf Pub.

Voogt, J.A. & Oke, T.R. 2003. Thermal remote sensing of urban climates. *Remote Sensing of Environment*, 86, (3) 370-384

Watson, I.D. & Johnson, G.T. 1987. Graphical estimation of sky view-factors in urban environments. *Journal of Climatology*, 7, (2) 193-197

Wesely, M.L. 1989. Parameterization of surface resistances to gaseous dry deposition in regional-scale numerical models. *Atmospheric Environment (1967)*, 23, (6) 1293-1304

Wesely, M.L. & Lesht, B.M. 1989. Comparison of RADM dry deposition algorithms with a site-specific method for inferring dry deposition. *Water Air Soil Pollut*, 44, (3-4) 273-293

WHO 2006. *WHO Air quality guidelines for particulate matter, ozone, nitrogen dioxide and sulfur dioxide: global update 2005: summary of risk assessment*, Geneva: World Health Organization. Accessed at: http://whqlibdoc.who.int/hq/2006/WHO_SDE_PHE_OEH_06.02_eng.pdf; 09/10/2014.

Zehnder, J. A. & Grossman-Clarke, S. 2009, "Urban Meteorological Modeling," *In Visualizing Sustainable Planning*, H. Hagen, S. Guhathakurta, & G. Steinebach, eds., Springer Berlin Heidelberg, pp. 93-108.

Zhou, Y. & Shepherd, J.M. 2010. Atlantas urban heat island under extreme heat conditions and potential mitigation strategies. *Nat Hazards*, 52, (3) 639-668

Erklärung

Ich versichere, dass ich die von mir vorgelegte Dissertation selbstständig angefertigt, die benutzten Quellen und Hilfsmittel vollständig angegeben und die Stellen der Arbeit - einschließlich Tabellen, Karten und Abbildungen - , die anderen Werken im Wortlaut oder dem Sinn nach entnommen sind, in jedem Einzelfall als Entlehnung kenntlich gemacht habe; dass diese Dissertation noch keiner anderen Fakultät oder Universität zur Prüfung vorgelegen hat; dass sie abgesehen von unten angegebenen Teilpublikationen noch nicht veröffentlicht worden ist, sowie, dass ich eine solche Veröffentlichung vor Abschluss des Promotionsverfahrens nicht vornehmen werde. Die Bestimmungen der Promotionsordnung sind mir bekannt. Die von mir vorgelegte Dissertation ist von Prof. Dr. Stefan Emeis betreut worden.

Garmisch-Partenkirchen,

_____